Development of a Turbine-Based Ocean Thermal Energy Harvesting Mechanism Applied to the Underwater Glider

By

Hongbo Hou

Student Registration Number: 201954073

A THESIS

Submitted in fulfillment of the requirements for the degree of

Doctor of Philosophy

Naval Architecture with Ocean Engineering

UNIVERSITY OF STRATHCLYDE

Declaration

This thesis is the result of the author's original research. It has been composed by the author and has not been previously submitted for examination which has led to the award of a degree.

This thesis has been approved as a partial fulfillment of the requirements for Degree of Doctor of Engineering in Naval Architecture with Ocean Engineering from Department of Naval Architecture, Ocean and Marine Engineering.

Thesis Advisor: *Weichao Shi, Laibing Jia, Mehmet Atlar*

Student Name: Hongbo Hou

Signature: Hongbo Hou **Date: 13/04/2023**

Table of Contents

List of Figures

List of Tables

Acknowledgements

The 4-year PhD journey has passed in the blink of an eye. Although the pandemic brought challenges, I experienced the most joyful and precious four years of my life. Without the help and support of everyone in my life, I would not have been so fortunate in my journey. Therefore, please allow me to express my gratitude to them at the beginning of this thesis.

Firstly, I wish to extend my profound appreciation and gratitude to my primary supervisor, Dr. Weichao Shi. His guidance provided me with the opportunity to pursue my doctorate and has profoundly impacted my academic and personal growth. Through his aid, I was able to not only complete my research but also evolve into a better version of myself. Similarly, I also extend my gratitude to another one of my supervisors, Dr. Laibing Jia. Our paths were intertwined in a magical way, and I am thankful for his selfless assistance in my doctoral journey. I must also express my sincere appreciation to my co-supervisor, Prof. Mehmet Atlar. His unwavering support and shared wisdom significantly contributed to my academic journey and the successful completion of my research.

Secondly, I would like to extend my gratitude to my colleagues and friends at the Applied Biomimetics Marine Hydrodynamics Research Group: Yunxin, Yang, Abel, Callum, Moritz, Kaan, Zeynep. I appreciate their friendship and help throughout my journey.

Thirdly, I would like to express my gratitude to my friends in life, Xiaodong, Marvin, Yihan, Yujia, Alex, Guangwei, Ming, Yi… Thank you for making my life more colorful, and I wish you all a bright future.

Finally, I would like to thank my family members, my mom, dad, aunt, uncle, brother and cousins. When I face any challenges in life, their support and love are my most important pillars. Without their help, I would not have come this far.

Abstract

Underwater gliders (UGs) are gaining popularity in ocean exploration. Extending the range and duration of UGs is becoming a current research focus; however, one of the primary obstacles to achieving this is the limited energy supply. This study developed a turbine-based energy harvesting mechanism (EHM) by researching the operational mechanism and design method of its turbine. The turbine-based EHM originated from the energy harvesting mechanism proposed by NASA. In NASA's original idea, when the turbine-based EHM is in operational mode, a thermal buoyancy engine exploits the ocean's temperature differences to change the glider's buoyancy by phase change material (PCM), driving it to move in the water; these maneuvers power a turbine mounted behind the glider to harvest energy.

Firstly, before delving into the turbine study, the conceptual design of NASA's turbine-based EHM is refined. To enhance the feasibility of NASA's turbine-based EHM, its original energy harvesting mode is modified according to the consideration of engineering constraints. In the new mode of the turbine-based EHM, the moving trajectory of UGs has been changed; the thermal buoyancy engine generates ballast force to propel UGs vertically through the ocean and simultaneously drives the turbine of the hull to rotate, thereby extracting energy from the fluid. Moreover, the original method of converting thermal energy into hydraulic energy of EHM is modified. This new energy harvesting mode of the turbine-based EHM will be adopted in subsequent research related to turbines.

Secondly, focusing on the turbine, to efficiently optimize it for harvesting the kinetic energy provided by the thermal buoyancy engines, a mathematical model based on blade element momentum theory (BEMT) is established to conduct extensive analysis. An enhanced BEMT model is integrated. Through numerous analyses using the mathematical model, a comprehensive understanding of the turbine's design philosophy is derived, including the optimal combination of C_p and C_t, the choice of the design tip speed ratio (TSR), the selection of the radius, and more. The model reveals a significant deviation from the traditional turbine design philosophies.

Furthermore, the mathematical model optimizes the turbine mounted behind UG hull and provides a preliminary estimate of the turbine-based EHM's capabilities.

Thirdly, as the understanding of the turbine's operating mechanisms in this study deepens, the Actuator Disk Theory is expanded. The current BEMT-based turbine design method assumes achieving the Betz limit when the axial induction factor (a) reaches 1/3. However, this only applies to turbines driven by a constant velocity, i.e., the velocity-driven turbine. The turbine in EHM, driven by ballast force, is essentially a force-to-velocity turbine, meaning it operates under a constant force and is powered by the velocity generated by this force. Consequently, this study extends the actuator disk theory for force-to-velocity turbines and identifies the relationship between the axial induction factor, power, and energy yield of the force-to-velocity turbine. Based on this relationship, a new BEMT-based design method is proposed for the preliminary design of force-to-velocity turbines, adapting to the unique working principles of the turbine in this study. A case study demonstrates and verifies the developed method, showing that the new method can quickly and effectively identify the optimal design for force-to-velocity turbines. Additionally, during the expansion of the actuator disc theory, some design philosophies of the turbine in this study, related to the optimal combination of C_p and C_t, are mathematically elucidated. The effectiveness and limitations of these philosophies, previously summarized, are discussed in light of these equations.

Lastly, to validate the energy harvesting capability of the turbine-based EHM, high-fidelity computational fluid dynamics (CFD) simulations were conducted using an optimally designed turbine based on previous findings. Using a typical UG hull and a turbine designed based on the prior design philosophy and the enhanced BEMT method with the expanded actuator theory, DFBI simulation of EHM was carried out with CFD software. CFD results suggest that a theoretically self-sustainable UG with unlimited endurance might be achievable, ignoring the lifespan of the components in the system. They also indicate that the turbine-based EHM might have the potential to compete with other OTEC-PCM systems in the future.

List of symbols and abbreviations

Abbreviation	Definition
A_D	cross-section of the stream-tube at the actuator disc
A_W	cross-section of the stream-tube at far downstream
A_∞	cross-section of the stream-tube at far upstream
a	axial induction factor
a'	tangential induced factor
a_{design}	design axial induction factor
a'_{design}	design tangential induction factor
a_{design_E}	design axial induction factor for the highest energy yield
a_{design_P}	design axial induction factor for the highest power
B	ballast force
B_D	component of the ballast force in the UG's forward direction
B_L	component of the ballast force in the UG's vertical direction
C	chord length
C_D	drag coefficients of the foil
C_d	resistance coefficient of the carrying platform
C_L	lift coefficients of the foil
C_n	normal coefficient
C_P	power coefficient from actuator disc theory
C_p	power coefficient from BEMT analysis and experiment
C_T	thrust coefficient from actuator disc theory
C_t	thrust coefficient from BEMT analysis and experiment
C_{T_h}	drag coefficient of the hull
$C_{T_h}^{\ b}$	drag coefficient of the bare hull
$C_{T_h}^{\ i}$	drag coefficient of the hull subjected to hydrodynamic interaction
D	diameter of UG hull
d_w	UG's operational depth
E_d	energy deficit
E_y	energy yield of the EHM
e_a	approximate relative error
L	working length
L_h	hull length
M_b	the buoyancy magnification

N	blade number
$N^{'}$	grid number
P	power
P_{DFBI}	power of EHM in DFBI simulation
P_{inner}	air pressure in the hull
$P_{\max}$	maximum gas pressure in the accumulator
P_P	pre-charge pressure in the accumulator
P_{PCM}	pressure of PCM
$P_{working}$	working pressure of UG
P_D^+	pressure in front of the actuator disc
P_D^-	pressure behind the actuator disc
P_∞	pressure far away from the actuator disc
p	apparent order
Q	torque imposed on turbine
Q_h	torque imposed on the hull
R	radius of the turbine
$R^{'}$	ratio of solution scalars
Re	Reynolds number
R_h	hull resistance
r	radius of the carrying platform
r^e	local radius of the blade element
r_i	radius of the ith ring
r_{21}^p	grid refinement factor
S	wet surface of UG hull
T	thrust of the turbine
T_b	thrust for each blade element
T_h	water temperature at the ocean surface
T_l	water temperature at the operational depth
T_{PCM}	temperature of PCM
T_t	turbine thrust
t	operation cycle time
U_D	velocity in front of the disc
U_W	flow velocity far downstream
U_∞	flow velocity far upstream
V	cruising velocity of UG
V_{DFBI}	velocity of UG from DFBI simulation

V_{PCM}	volume of PCM
V_{PCM_L}	volume of PCM in liquid phases
V_{PCM_S}	volume of PCM in solid phases
V_{real}	real velocity of UG in the iteration
V_{wake}	wake velocity
W	relative velocity
W_k	work input by the carrying platform
W_f	wake factor
W_{f_i}	the wake factor of the ith ring
α	angle of attack
α_{design}	design angle of attack
β	twist angle
ε	difference between the solution scalars
η_h	hydrodynamic energy conversion efficiency
η_m	efficiency for the turbine in momentum level
λ	tip speed ratio
λ_{design}	design tip speed ratio
$\lambda_{equivalent}$	equivalent tip speed ratio
$\lambda_{operating}$	operating tip speed ratio
μ	ratio of the local radius
ρ	water density
σ_r	chord solidity
φ_1	result of fine mesh grids
φ_2	result of medium mesh grids
φ_3	result of coarse mesh grids
ϕ	inflow angle
ϕ_{design}	design inflow angle
ϕ_g	gliding angle
Ω_e	effective rotation speed
Ω_t	turbine's rotational velocity
Ω_h	hull's rotational velocity around its own axis
Δr	width between each ring
$\%GCI^{21}_{FINE}$	GCI index
Abbreviation	**Definition**
AIC	Axial Induction Control

AoA	Angle of Attack
AUV	Autonomous Underwater Vehicles
BEMT	Blade Element Momentum Theory
BET	Blade Element Theory
CFD	Computational Fluid Dynamics
DFBI	Dynamic Fluid Body Interaction
DFIG	Doubly Fed Induction Generator
EHM	Energy Harvesting Mechanism
ESM	Energy Storage Materials
GCI	Grid Convergence Index
HAT	Horizontal Axis Turbine
LSB	Laminar Separation Bubble
N2	Nitrogen
NASA	National Aeronautics and Space Administration
OTEC	Ocean Thermal Energy Conversion
OTEC-PCM	Ocean Thermal Energy Conversion with PCM
PCM	Phase Change Material
RAT	Ram Air Turbine
RBM	Rigid Body Motion
UG	Underwater Glider
URANS	Unsteady Reynolds Averaged Navier Stokes
VAT	Vertical Axis Turbine
TEG	Thermoelectric Generator
PVT	Pressure-Volume-Temperature relationship
TSR	Tip Speed Ratio

1 Introduction

The primary objective of this chapter is to introduce the Ph.D. project, focusing on the development of an energy harvesting turbine in a turbine-based energy harvesting mechanism (EHM) for underwater gliders (UGs). Section 1.1 presents the motivation for this research. This is followed by the main aim and objectives in Section 1.2. Section 1.3 outlines the structure of this chapter, and Section 1.4 provides a summary.

1.1 Motivation

It is widely recognized that oceans will assume a greater significance in the global economy in the coming years. As a result, ocean monitoring is essential to deepen our understanding of the oceans and to harness their potential wealth (Falcão et al., 2018). For centuries, oceanographers have depended on ships for data collection and observations. This ship-based research has enriched our understanding of various oceanic phenomena, including ocean circulation, plate tectonics, global ocean productivity, and climate-ocean interactions (Schofield et al., 2007). However, the use of ships comes with its own set of limitations. They cannot provide the fine spatial and temporal resolution often required for detailed studies, and their operational costs can be prohibitive. Given these constraints, UGs have recently emerged as pivotal tools in ocean exploration, thanks to their extended endurance and cost-effectiveness. UGs operate using a buoyancy engine, which alters buoyancy to enable the glider to rise and sink in the water. This is achieved by pumping hydraulic oil in and out of UG hull. Additionally, horizontal movement is facilitated by hydrofoils, allowing UGs to travel in a sawtooth pattern. Several companies and organizations have pioneered the development of commercial UGs equipped with electrical buoyancy engines. Notable examples include Slocum, Seaglider (Eriksen et al., 2001), Spray (Sherman et al., 2001), and Petrel (Xue et al., 2018).

Enhancing the range and endurance of UGs has emerged as a focal point in research, primarily because increasing both can lead to substantial cost savings in ocean observation. Additionally, this extension facilitates scientists in acquiring high-fidelity data (Javaid et al., 2014, Wang et al., 2020).

One of the principal challenges for achieving extended range is their limited energy source. Due to their compact interior space, they cannot house high-capacity batteries needed to power diverse electronic devices. A promising solution lies in harnessing ocean thermal energy to drive a thermal buoyancy engine within the glider. Gliders equipped with this engine are referred to as Thermal UGs (Wang et al., 2020, Webb et al., 2001, Yang et al., 2016, Ma et al., 2016). In contrast to conventional electrical buoyancy engines, which can deplete over half of UGs' battery power, thermal buoyancy engines convert oceanic thermal energy into mechanical energy. This mechanical energy then propels UGs. On average, a thermal buoyancy engine can extend UGs' operational range by 3 to 4 times (Davis et al., 2002, Webb et al., 2001).

While thermal buoyancy engines considerably reduce energy consumption related to propulsion, Thermal UGs must still power their onboard payloads and attitude control systems. As a result, the energy remains a limiting factor in the evolution of Thermal UGs. Both electric and thermal gliders, moreover, exhibit relatively modest speeds, capping at about 1 knot. In scenarios demanding higher-speed cruising, the incorporation of extra thrusters becomes essential, posing further demands on battery capacity. One potential avenue to mitigate this energy deficit involves the development of Ocean Thermal Energy Conversion (OTEC) systems. These systems transform oceanic thermal energy into electrical energy, making it accessible for UGs. Contemporary advancements have gravitated towards hydraulic-based systems. These systems incorporate a mini turbine and generator within the high-pressure oil circuit, capitalizing on energy during the ballasting phase when the thermal engine expels hydraulic oil (Chao, 2016, Jones et al., 2014, Wang et al., 2019). Notwithstanding these strides, traditional hydraulic-based OTEC systems are not without their setbacks, notably their diminished reliability and energy harvesting efficacy.

In 2006, NASA introduced a novel EHM designed specifically for Thermal UGs, presenting a unique technological pathway for OTEC. This system leverages a thermal buoyancy engine to propel UGs through water. Simultaneously, a turbine positioned behind the hull spins, transforming kinetic energy into electrical power (Chao, 2006). This EHM stands apart from conventional OTEC

systems. A standout feature is its ability to adjust both pitch and rotation speed, enabling the glider to utilize propeller-based propulsion. This adaptation not only broadens the operational scope of UGs (Jones et al., 2014) but also facilitates greater movement speeds, enhancing resilience against powerful currents (Claus et al., 2012). Moreover, unlike traditional OTEC configurations that incorporate mini turbines within their oil circuits, this EHM design avoids placing moving components inside the high-pressure oil circuit. The result is a system marked by simplicity and reduced susceptibility to failures (Falcão et al., 2018), culminating in heightened reliability.

The turbine within this kind of turbine-based EHM plays a pivotal role as a key functional unit. It dictates the proportion of harvestable kinetic energy, provided by the thermal buoyancy engines, that can be transformed into electricity. While the turbine possesses a unique operating mechanism and set of conditions, it remains under-researched. Crucially, the overarching philosophy guiding its design remains ambiguous in the present context. This gap in understanding and research is a significant factor in the energy harvesting system's non-implementation. To date, there has been no substantial exploration into the viability of this kind of system.

These technical insights and observed developments prompted the author to investigate the potential of this kind of turbine-based energy harvesting system. The focal point of this exploration is the study and enhancement of the turbine within this kind of turbine-based EHM, aiming to fully realize its capabilities.

1.2 Aim and objectives

Given the motivation and literature review presented in Chapter 2, this Ph.D. project aims to enhance UGs' voyage and duration by developing the energy harvesting turbine within the turbine-based EHM.

To achieve this aim, the following objectives have been set:

- Objective 1: Conduct an extensive literature review on the contemporary design and optimization of turbines within EHMs. This will facilitate a better understanding of current research topics, highlight knowledge gaps in the field, and propose an apt research methodology tailored to the project's goals.
- Objective 2: Identify a more viable energy harvesting mode for the mechanism, taking into account practical engineering constraints. This step also involves preliminary groundwork to pave the way for subsequent turbine research.
- Objective 3: Design and optimize the turbine using blade element momentum theory (BEMT). This will be achieved by constructing a mathematical model for the turbine-based EHM and conducting exhaustive analyses of various turbine designs to deepen understanding of the turbine's design philosophy and operating principles.
- Objective 4: Delve deeper into the observations made during Objective 3 by exploring them mathematically. This will enhance comprehension of the turbine's operation within the energy harvesting framework. The aim here is to refine and expand upon the actuator disk theory, a foundational aspect of BEMT. With this enriched understanding, a novel BEMT-based design methodology tailored to the turbine's distinctive operational principle will be developed.
- Objective 5: Validate the energy harvesting capability of the mechanism fitted with the newly-designed turbine based on the findings in Objectives 3 and 4 through CFD simulation.

1.3 Thesis layout

The research aims and objectives have been achieved through the work documented in this thesis, which is organized across several chapters. A detailed outline of these chapters is provided below:

Chapter 1 provides an introduction to the research encapsulated in the thesis. It offers readers insight into the motivation behind the research, its aims and objectives, and the structure of the thesis. This chapter serves as a concise primer on the research undertaken.

Chapter 2 conducts an exhaustive literature review on the cutting-edge ocean thermal EHM for UGs, with particular emphasis on turbines used in such mechanisms, addressing "Objective 1". The

chapter aims to broaden the understanding of pertinent research topics and refines the research objectives by pinpointing knowledge gaps.

Chapter 3 proposes a new energy harvesting mode for EHM that is grounded in practical engineering considerations, directed towards "Objective 2". The primary intent is to bolster the viability of EHM. The chapter also delineates design parameters of EHM, excluding the turbine, paving the way for a detailed turbine study.

Chapter 4 attends to "Objective 3" by designing and optimizing the turbine in EHM through BEMT and a mathematical model. It harnesses the computational efficiency of BEMT to design and scrutinize a plethora of turbines. Further, the chapter delves into the working principles and design nuances of the turbine by analyzing a comprehensive dataset.

Chapter 5 concentrates on "Objective 4", elucidating the phenomena detailed in Chapter 4 at a mathematical juncture. This chapter further expands upon the actuator disk theory for turbines within EHM, establishing correlations between the axial induction factor, power, and energy yield. Building upon the revised actuator disk theory, a novel BEMT-based turbine design method is introduced.

Chapter 6 achieves "Objective 5" by employing computational fluid dynamics (CFD) for verification purposes. It conducts a dynamic fluid body interaction (DFBI) simulation of the entire system to affirm the energy harvesting capabilities and viability of the turbine-based EHM fitted with an optimal turbine, as deduced from findings in Chapters 4 and 5.

Chapter 7 provides a comprehensive summary of the study, including the research aims and objectives, as well as articulating key conclusions. It also proffers suggestions for potential future investigations in this domain.

The thesis structure is represented in Figure 1-1

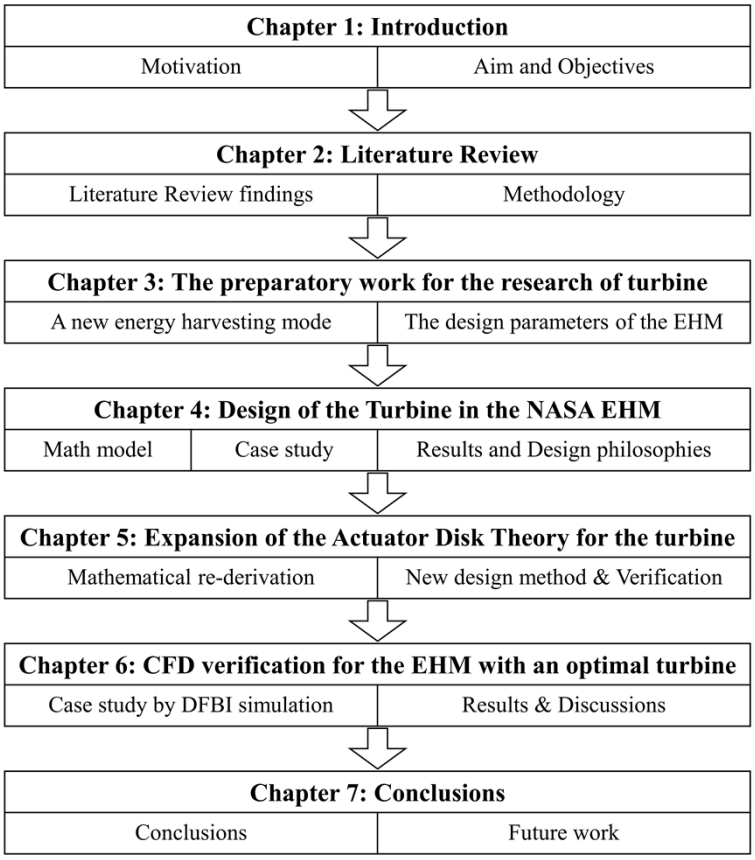

Figure 1-1. The framework of the thesis layout

1.4 Summary

Chapter 1 introduces the research outlined in this thesis. It highlights the motivation behind the study and delineates the primary aim and objectives of the research. Additionally, it provides an overview of the thesis structure, guiding readers on what to expect in subsequent chapters.

2 Literature review

The main objective of this chapter is to confirm the aim and objectives of this research through a comprehensive literature review. This involved pinpointing the existing gaps in the state-of-the-art literature concerning EHM used in UGs.

Firstly, various types of UGs were examined to understand their developmental trajectories, challenges faced during their evolution, and the strategies employed to overcome these challenges (Section 2.1). Subsequently, the chapter delved into recent advances in the research field of OTEC with PCM (OTEC-PCM) as applied to UGs. This analysis sought to comprehend the progression of OTEC-PCM and introduce the specialized OTEC-PCM under study, namely turbine-based EHM (Section 2.2). This was followed by a review of the principles governing the thermal engine in EHM (Section 2.3). Next, the horizontal axis turbine (HAT) and its prevailing design methodologies were explored, with a special emphasis on the challenges associated with using current design techniques to tailor the turbine in EHM (Section 2.4). The subsequent section offered an exhaustive review of cutting-edge methodologies that can be employed to probe the intricate workings of the thermal buoyancy engines and the tidal turbine (Section 2.5). In conclusion, synthesizing the discoveries and addressing the identified knowledge gaps has reconfirmed the aim and objectives of the thesis (Section 2.6).

2.1 UGs and their energy shortage challenges

2.1.1 Background of UGs

The unanimous understanding is that the oceans are poised to assume an even greater significance in the global economy in the imminent future. Consequently, monitoring these vast water bodies becomes pivotal to our endeavors in deciphering the mysteries of the oceans and tapping into their latent resources (Falcão et al., 2018). Historically, oceanographers have largely depended on ships as their primary tool for data collection and observations during research expeditions. As illustrated in Figure 2-1, this mode of operation has yielded a trove of insights into realms such as ocean

circulation, plate tectonics, marine productivity, and the interplay between climate and oceans (Schofield et al., 2007). Nonetheless, ships come with their own set of constraints. Not only do they offer limited spatial and temporal resolution, but they also demand hefty operational expenses (Eriksen et al., 2001).

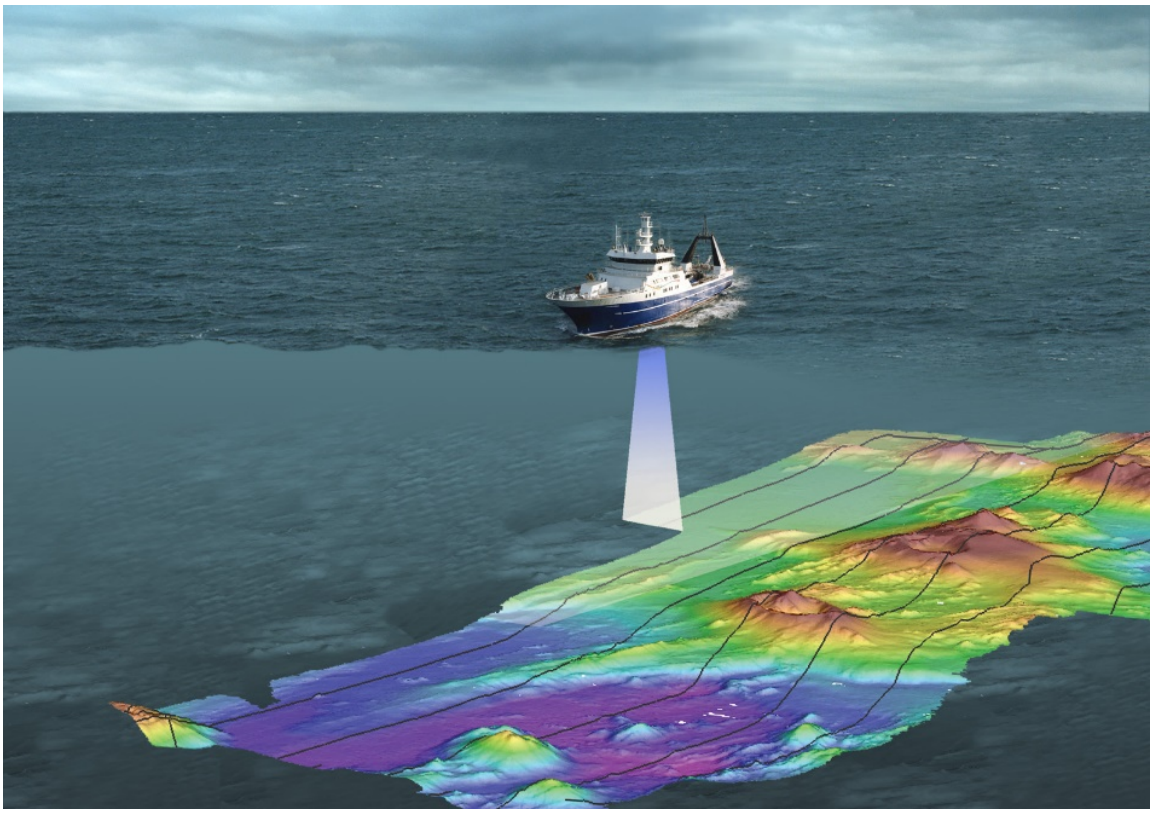

Figure 2-1. RV Tangaroa (NIWA, 2022)

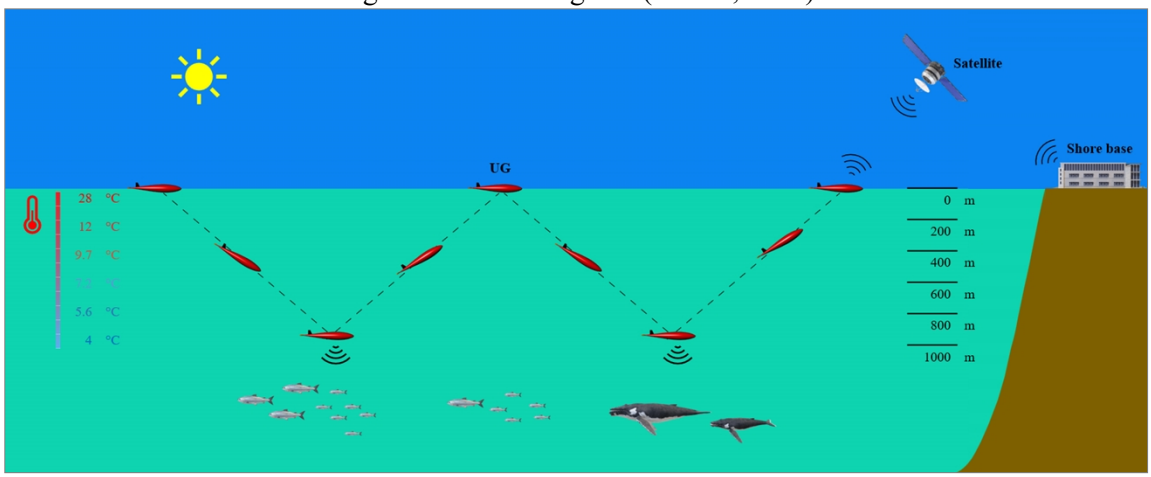

Figure 2-2. Sawtooth trajectory of an UGs

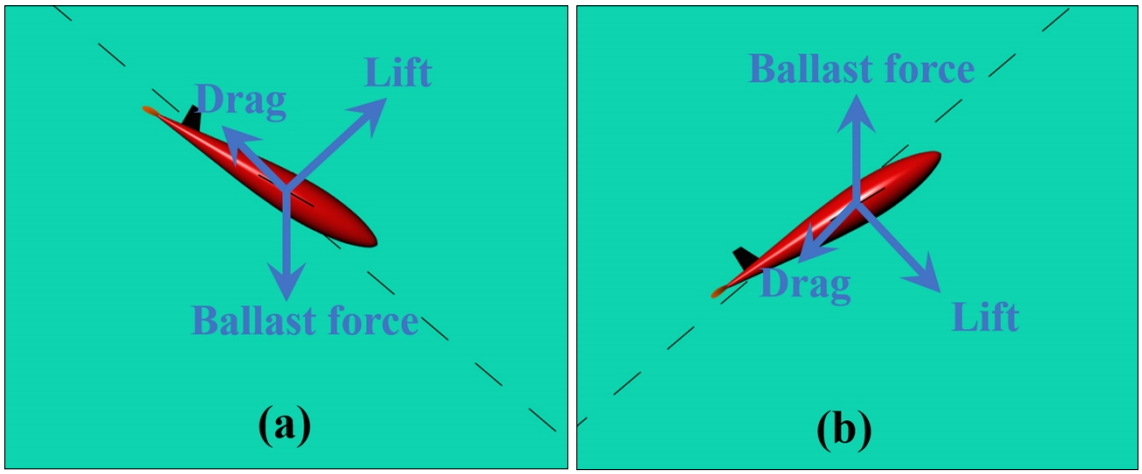

Figure 2-3. Forces acting on the glider during a steady glide motion: (a) Descending glide; (b) Ascending glide

In light of these challenges with traditional oceanic data collection methods, UGs have emerged as a predominant tool for ocean exploration in recent times. Its rise in popularity can be attributed to its remarkable endurance, expansive range, and cost-effective operations. The glider in this study harnesses the power of a buoyancy engine. This engine facilitates changes in buoyancy, enabling the glider to oscillate between ascending and descending in the water. Through hydrofoils, horizontal forces are produced, making it possible for UGs to move in a sawtooth trajectory, as depicted in Figure 2-2. The interplay of forces exerted on the glider during its ascent and descent is illustrated in Figure 2-3. Here, the ballast force is a manifestation of the differential between buoyancy and gravity. Today, UGs are in active service with over 50 enterprises and research institutions globally. They play a crucial role in gauging various oceanic parameters such as seawater temperature, salinity levels, surface and average currents, depth, both apparent and inherent optical properties, fluorescence, and more. This is made possible by equipping UGs with a diverse array of sensors (Schofield et al., 2007). An example of UGs' capability is displayed in Figure 2-4, showcasing a detailed salinity map of the ocean produced using the data collected by UGs.

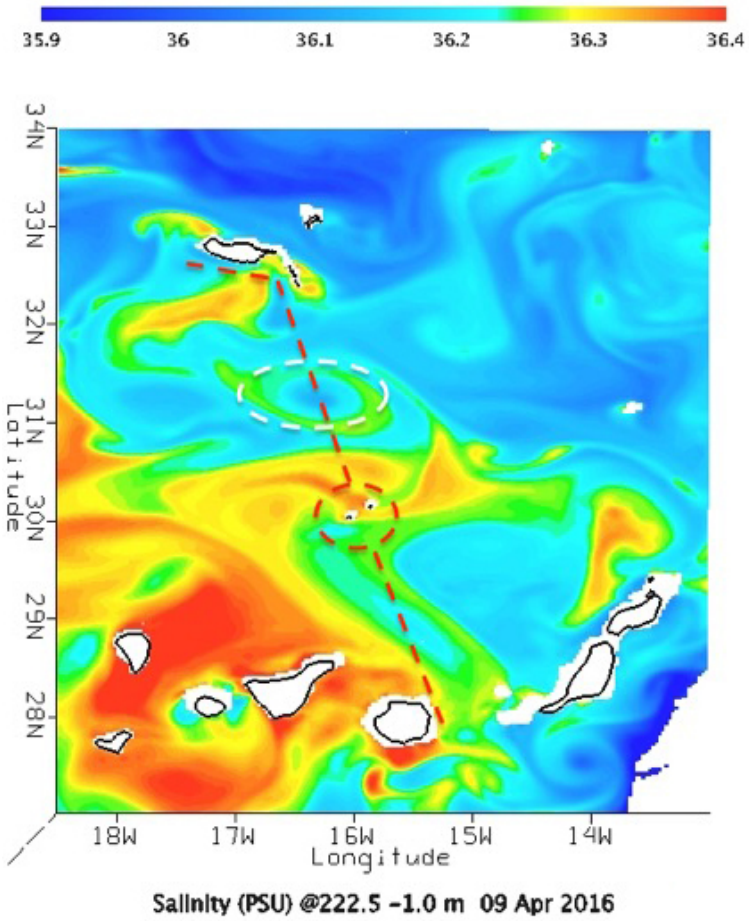

Figure 2-4. Salinity of the ocean explored by UGs (PLOCAN, 2016)

2.1.2 Varieties of UGs and their energy supply solutions

Electric UGs

Several commercial Electric UGs, powered by electrical buoyancy engines, have been developed by various companies and institutions. Some notable examples include:

- Slocum, developed by Teledyne Marine (Jones, 2012).
- Seaglider, a creation of University of Washington (Eriksen et al., 2001).
- Spray, devised by Woods Hole Oceanographic Institution (Sherman et al., 2001).
- Petrel, a product of Tianjin University (Xue et al., 2018).

These Electric UGs are depicted in Figure 2-5.

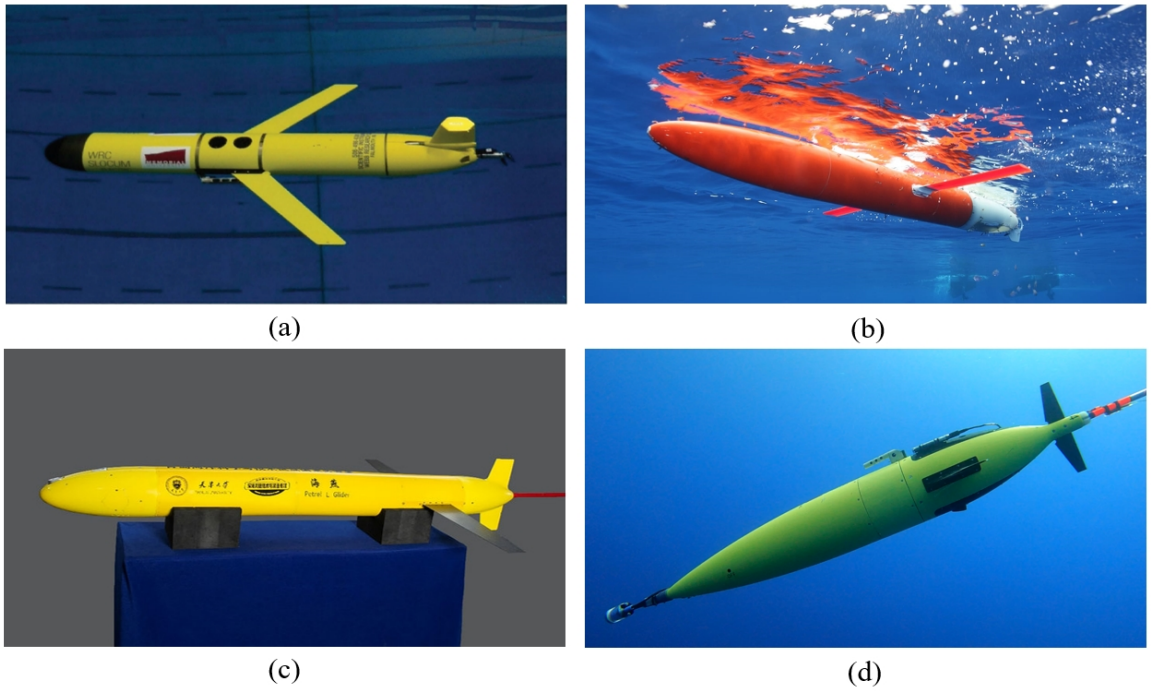

Figure 2-5. UGs from Various Developers: (a) Slocum; (b) Spray Glider; (c) Petrel; and (d) Seaglider (Jones, 2012, WHOI, 2022, Yang et al., 2022, Cyprusubsea, 2022)

The electric buoyancy engine-driven UGs can execute missions spanning several thousand kilometres and lasting for many months (Eriksen et al., 2001). For instance, Slocum set a remarkable undersea world record by traversing 7,570 km over an uninterrupted 330-day journey (IMOS, 2017).

A primary challenge in the advancement of Electric UGs stems from their restricted energy and mission capabilities (Jones et al., 2014). The constrained internal space of UGs limits the size of the battery they can house, consequently curtailing both the voyage range and the onboard electronic payloads they can carry. This limited energy storage hinders UGs' mission duration. Moreover, UGs' set sawtooth trajectory restricts its ability to study a specific depth consistently. This limitation has led to the introduction of auxiliary propeller-based propulsion modules to expand mission capabilities (Jones et al., 2014). However, integrating such a system escalates energy consumption, further intensifying the energy demands.

Currently, the most feasible solution for Electric UGs to mitigate this energy shortfall is to augment the battery package's capacity. However, this approach is nearing its threshold due to the physical constraints of UGs and the bounds of existing battery technology.

Hybrid UGs

As previously mentioned, the addition of an auxiliary propeller-based propulsion module to Electric UGs presents a viable solution to their restricted mission capabilities. With this in mind, Hybrid UGs have emerged and gained traction. A typical example is SLOCUM G2, as shown in Figure 2-6.

Figure 2-6. Illustration of SLOCUM G2 Hybrid UG (GEO-matching, 2022)

SLOCUM G2 features a foldable propeller positioned at the end of its hull, as illustrated in Figure 2-7. In the buoyancy-driven mode, the foldable blades transition into a streamlined form to minimize drag, allowing UGs to move at a speed of 0.35 m/s. In the propeller-driven mode, the propeller extends, enabling UGs to travel at a faster speed of 0.8 m/s and achieve a more flexible operational trajectory (Jones et al., 2014). Several other Hybrid UGs are in the pipeline for commercialization, including the Urashima developed by Nagasaki University (Yamamoto, 2015), Fòlaga jointly developed by Italy and Spain (Caffaz et al., 2010), and Petrel from Tianjin University (Niu et al., 2017).

Figure 2-7. Folding propeller design (Jones et al., 2014)

Hybrid UGs, however, have the limitation of a comparatively shorter range and duration than traditional Electric UGs. This arises from the fact that the energy consumption of the propeller is considerably higher than that of the buoyancy engine. Given the limited battery capacity of UGs, they cannot support extended-range missions. Consequently, the propeller-based propulsion system serves merely as an auxiliary module for UGs.

Like their electric counterparts, a potential solution for Hybrid UGs to tackle the energy supply challenge is to augment the capacity of the battery package.

Thermal UGs

The ability to extend the duration and range of UGs can substantially decrease the costs associated with ocean observations. As a result, enhancing the range and duration of UGs has emerged as a prominent area of research (Javaid et al., 2014). Against this backdrop, harnessing ocean thermal energy to power the buoyancy engine of a glider has been suggested as a viable approach to prolong operational range and duration in the ocean (Wang et al., 2020, Webb et al., 2001, Yang et al., 2016, Ma et al., 2016). Gliders that utilize a thermal buoyancy engine are termed Thermal UGs. This engine can transform the thermal energy present in seawater into mechanical energy. This mechanical energy is then employed to generate ballast force, propelling UGs to rise and fall in a sawtooth trajectory within the ocean. A detailed review of the thermal engines can be found in

Section 2.3.1. The operating principle and standard working mode of Thermal UGs are depicted in Figure 2-8.

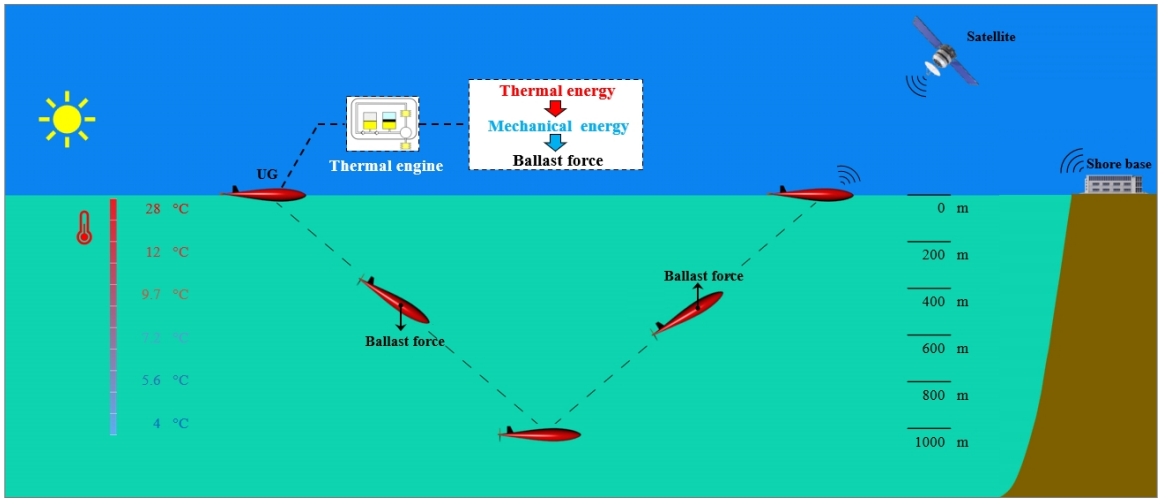

Figure 2-8. Working principle and operating mode of Thermal UGs

In contrast to the electrical buoyancy engine, which consumes 60-85% of Electric UGs' battery power, the thermal buoyancy engines can harness the ocean's thermal energy, potentially increasing the glider's voyage by 3-4 times (Davis et al., 2002).

Figure 2-9. Slocum Thermal design (Niewiadomska, 2004)

In 1998, the world's first Thermal UG, Slocum Thermal, was initially tested at Lake Seineca in New York, as depicted in Figure 2-9. Following this, Slocum Thermal underwent an eight-month sea trial to demonstrate the feasibility of a thermal glider; its designers assert that Slocum Thermal's

range could extend up to 40,000 km (Webb et al., 2001, Wang et al., 2020). By 2005, the second-generation Slocum Thermal glider was successfully developed, offering enhanced technical maturity, reliability, and stability. In 2008, the third-generation Slocum Thermal glider was introduced. Although it was eventually lost in the ocean, it demonstrated its potential commercial value (Wang et al., 2020, Jones et al., 2009). Tianjin University has pioneered two versions of Thermal UGs known as Petrel Thermal glider. In 2005, experiments with the Petrel Thermal glider took place at Qiandao Lake, China. By 2013, the second generation, named Petrel II, was developed. Sea trial outcomes indicated that Petrel Thermal gliders could sustain a consistent cycle in long-term tests, underscoring their reliability (Yang et al., 2016, Zhang et al., 2009a, Wang et al., 2020). Petrel Thermal UG is showcased in Figure 2-10.

Figure 2-10. Petrel Thermal UG design (Zhang et al., 2009b)

The developmental trend for Thermal UGs focuses on extending both range and duration, aiming for a theoretically unlimited voyage. This unlimited range and duration can lower operational costs and allow scientists to gather high-density data. Such comprehensive data collection is crucial for understanding the ocean's hydrological characteristics (Wang et al., 2020). Although thermal buoyancy engines can significantly reduce energy consumption related to propulsion, Thermal UGs still require energy for their onboard payloads and attitude control systems. Thus, similar to Electric UGs, the advancement of Thermal UGs also centers on energy considerations.

UGs with OTEC-PCM

To achieve a theoretically unlimited range and duration for UGs, several researchers have explored OTEC technologies, which harness the ocean's thermal energy to provide electrical power for the routine operations of UGs. Given that OTECs often leverage phase change material (PCM) for energy conversion, this process is also referred to as OTEC-PCM. OTEC-PCM uses PCM to transform thermal energy into mechanical energy. This mechanical energy then drives a mini turbine within the oil circuit, generating electrical energy to power system components (Wang et al., 2020). More details about OTEC-PCM can be found in Section 2.2.

By integrating OTEC-PCM, the range of Electric UGs can be considerably extended. For instance, Tianjin University designed Electric UGs equipped with an OTEC-PCM module (dubbed Smart Float) and conducted a sea trial (Zhang et al., 2022), as illustrated in Figure 2-11. Furthermore, in 2009, SOLO-TREC, sponsored by JPL Research & Technology Development program and the Office of Naval Research, was developed and underwent testing (JPL, 2009).

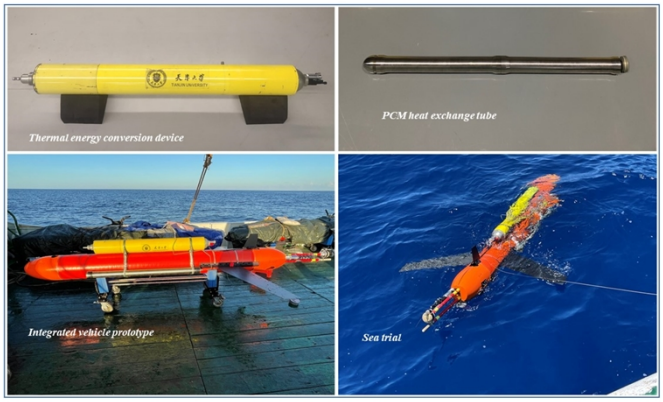

Figure 2-11. OTEC-PCM module applied to UGs (Zhang et al., 2022)

While OTEC-PCM modules incorporated in Smart Float and SOLO-TREC are adept at converting thermal energy to electrical energy using PCM, they cannot employ PCM directly for UGs propulsion like Thermal UGs do. Given that propulsion consumes up to 85% of UGs' energy, Teledyne Marine introduced Slocum Thermal E-Twin UG, which not only comes equipped with an OTEC-PCM but can also utilize it as a thermal buoyancy engine, as depicted in Figure 2-12.

Since the electrical energy harnessed by OTEC-PCM primarily powers the onboard payloads and attitude control systems—which are relatively low-energy consumers—Slocum Thermal E-Twin has the potential to operate as a global class glider with an endurance spanning several years (Jones et al., 2014).

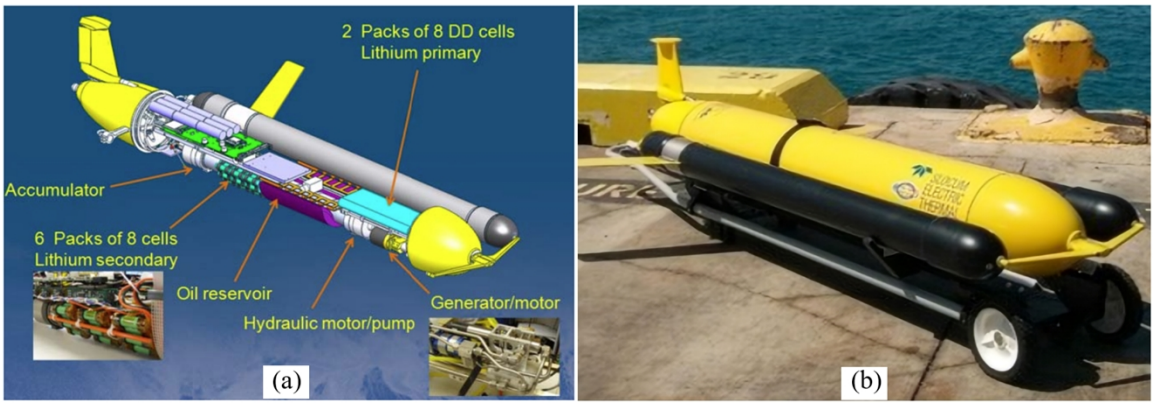

Figure 2-12. Slocum Thermal E-Twin gliders with OTEC-PCM: (a) Internal schematic diagram; and (b) External structural diagram (Jones et al., 2014)

The primary challenge confronting this type of UG is their reliability. Current OTEC-PCM technology in UGs produces electricity by deploying a mini hydraulic turbine in the oil circuit. The presence of moving parts within this high-pressure oil circuit can create a system prone to complications and failures (Falcão et al., 2018). Furthermore, the operating environment for hydraulic turbines in such OTEC-PCM configurations is often marked by high pressure and low volume. For instance, the hydraulic turbine in Slocum Thermal E-Twin operates under exceedingly high pressures, going up to 3000 psi (approximately 21 MPa). Even with the inclusion of two heat transfer devices, the hydraulic oil volume driving the turbine is a mere 1000 cc. This combination of high-pressure and low-volume results in suboptimal efficiency of the hydraulic turbine (Wang et al., 2019).

Another limitation is that the prevailing OTEC-PCM technology can only capture a restricted energy yield. For instance, the energy output of Slocum-TREC glider, equipped with 10 kg of PCM, stands at approximately 6.5 kJ per cycle when operating at a depth of 1200 m (Haldeman et al.,

2015). In the case of Electric UGs, this energy yield typically falls short of the consumption needs. While Thermal UGs might strike a balance between energy yield and consumption, the capacity for onboard payloads remains restricted.

Given that energy remains the primary obstacle in the evolution of UGs, Thermal UGs integrated with OTEC-PCM, despite their current challenges, stand as a pivotal pathway for UGs advancement. Consequently, this research emphasizes Thermal UGs with OTEC-PCM.

2.1.3 Summary

In Section 2.1, the history and progression of UGs were detailed. Commercially available UGs were examined and categorized into four groups: Electric UGs, Thermal UGs, UGs with OTEC-PCM, and Thermal UGs with OTEC-PCM. The strengths and challenges of each category were explored. Literature insights indicate that one of the central challenges in advancing UGs is the ongoing constraint of battery capacity, which results in energy limitations. Tapping into ocean thermal energy for conversion to electrical energy, or directly propelling UGs, emerges as a promising answer to this issue.

From the evidence gathered from prior research, it is apparent that Thermal UGs can harness thermal energy, convert it into mechanical energy, and then use this mechanical force for propulsion. This extends UGs' range and duration by approximately 3 to 4 times. UGs equipped with OTEC-PCM can harness thermal energy, transform it into mechanical energy, and then convert this mechanical force into electrical energy, catering to UGs' daily operational needs and further enhancing its operational duration. Thermal UGs with OTEC-PCM, being a hybrid of Thermal UGs and UGs with OTEC-PCM, amalgamates the benefits of both and has the potential to be indefinitely self-sustaining in the ocean, provided the system components' lifespans are not considered. This study pivots on advancing this UGs category, viewing it as a pivotal direction for future progression.

2.2 Application of OTEC in UGs

Underwater vehicles have the capacity to harness diverse energy sources from the ocean, including ocean thermal energy (Wang et al., 2020), solar energy (Crimmins et al., 2006), wave energy (Li et al., 2022), and salinity-gradient energy (Jung et al., 2022). Among these, thermal energy stands out as especially apt for underwater vehicles due to its consistent availability in the ocean. This consistent presence is attributed to temperature differentials between the sea surface and the deep ocean (Wang et al., 2019). Consequently, various forms of OTEC have been innovated to empower UGs to tap into this energy, converting it into usable electricity.

2.2.1 Overview of OTEC

OTEC primarily consists of two categories: OTEC based on the thermoelectric generator (OTEC-TEG) and OTEC based on OTEC-PCM.

OTEC-TEG

OTEC-TEG system is designed to directly convert thermal energy into electrical energy, leveraging either the Seebeck or the Peltier effect (Lee et al., 2018). Falcao incorporated this technology into UGs, devising a setup consisting of a TEG, energy storage material (ESM), and heat transfer fins (Falcão et al., 2018), illustrated in Figure 2-13. Relying on thermodynamic principles, the mechanism harnesses the temperature gradient between the heat transfer fins and ESM to generate electrical energy directly (Wang et al., 2019).

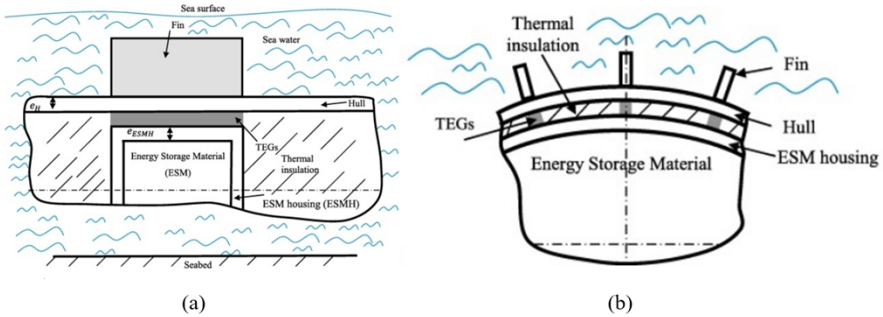

Figure 2-13. OTEC-TEG: (a) Side view; (b) Front view (Falcão et al., 2018)

The primary advantage of OTEC-TEG is its operational reliability since its power generation components are not exposed to extremely high pressures. However, there are downsides. Firstly, the efficiency of TEG-based OTEC is quite low. To generate 6000 J of electric energy in a single dive-ascend cycle, the system requires a significant amount of PCM, weighing up to 29 kg. Additionally, the elevated cost of TEGs undermines the economic feasibility of this approach. A single unit might set one back by several tens of euros, and the entire system necessitates around 5000 such units (Falcão et al., 2018).

OTEC based on OTEC-PCM

PCM is a substance that undergoes significant heat absorption or release during its phase transition, as illustrated in Figure 2-14 (Schmidt, 2007). In its melting phase, PCM can experience a substantial volume expansion, thereby generating high pressure. For example, certain PCM can swell by up to 9% in volume when subjected to an external force of 60 MPa (Kong et al., 2010). This expansion process produces a significant amount of mechanical energy, which OTEC-PCM systems can then convert into electrical energy. Presently, OTEC-PCM technology is evolving towards maturity, with various practical applications being implemented in UGs.

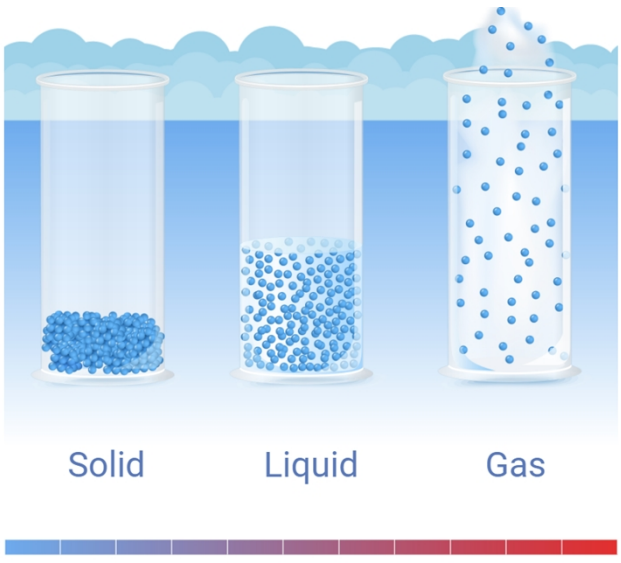

Figure 2-14. PCM application (Seatrec, 2022)

OTEC-PCM technology can be categorized into two types based on the method of mechanical transmission. The first type uses a Rack-Pinion Gear system to transform mechanical energy into electrical energy, as depicted in Figure 2-15. In this setup, when UGs are at the warm sea surface, PCM (wax) melts and expands. This expansion forces the oil within PCM chamber to be pushed into an accumulator containing high-pressure gas (Bellows). Once PCM has fully melted, a magnetic valve opens, allowing the high-pressure N_2 from the accumulator to propel both the piston and Rack-Pinion Gear system forward. This forward movement results in the rotation of the gear and generator, subsequently generating electricity that charges a battery pack (NASA, 2009).

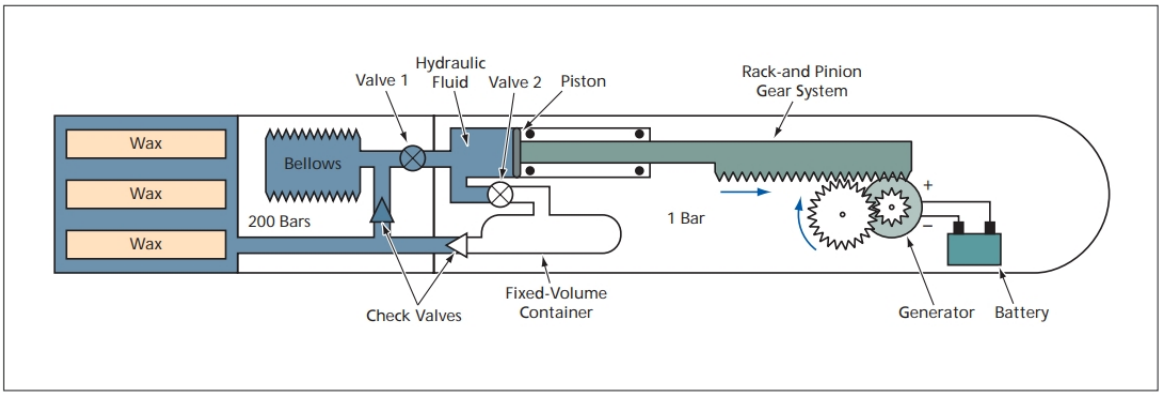

Figure 2-15. OTEC-PCM based on Rack-Pinion Gear system (NASA, 2009)

This design, however, confronts several challenges. Firstly, the Rack-Pinion Gear system exhibits low drive efficiency, averaging only about 50%. Secondly, its intricate structure demands costly customization. Thirdly, the substantial density of the rack-pinion gear system culminates in a significantly heavy system. As a result, this hydraulic-based OTEC-PCM design has not seen widespread adoption (Wang et al., 2020).

Another form of OTEC-PCM has gained more practical traction. This configuration incorporates a mini hydraulic turbine within the high-pressure oil pipeline. This mini hydrodynamic turbine activates a generator to recuperate energy as the accumulator expels hydraulic oil. Figure 2-16 provides a schematic of this OTEC-PCM variation. In 2009, SOLO-TREC was pioneered by the Jet Propulsion Laboratory (JPL) and the California Institute of Technology using this OTEC-PCM

model. It boasts ten heat exchangers filled with PCM and is capable of storing 1.7 Wh of energy during each operational cycle (Chao, 2016). Tianjin University crafted its OTEC-PCM prototype grounded in this concept; sea trials indicate that the prototype, weighing 6 KG, can garner 1.86 Wh in each power cycle (Wang et al., 2019). A separate energy harvesting module, following this technical trajectory and created by Tianjin University, has been integrated into Smart Float autonomous underwater vehicles (AUVs). Sea trials have demonstrated that the module, containing 4.5 L of N-hexadecane, can harness 1.487 Wh of energy per cycle on the Smart Float AUVs (Zhang et al., 2022).

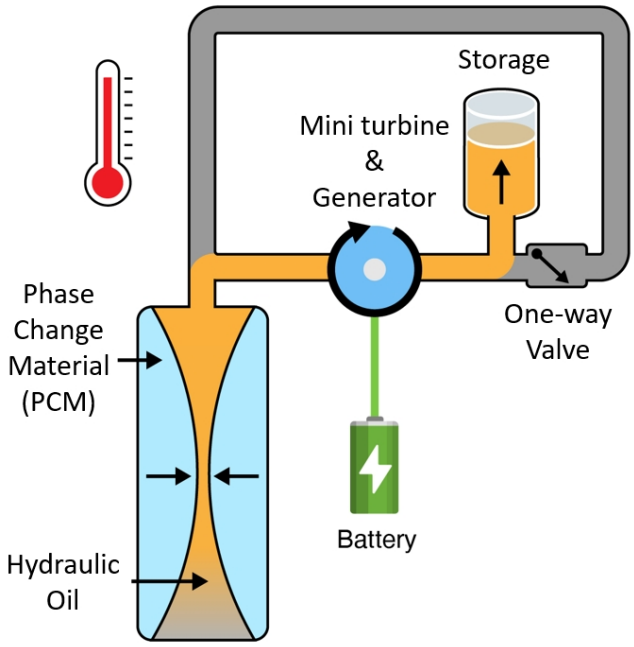

Figure 2-16. OTEC-PCM based on a mini hydrodynamic turbine (Seatrec, 2022)

This type of OTEC-PCM boasts the benefits of simplicity and compactness. Moreover, its hydraulic-to-kinetic conversion efficiency is remarkably high, ensuring the effective transformation of hydraulic energy output from the accumulator into the hydrodynamic output of the turbine within the pipe (Wang et al., 2019).

However, this OTEC-PCM variant has its drawbacks. Reliability stands out as the primary concern; the mini hydrodynamic turbine operates under pressures that can exceed 20 MPa (Wang et al., 2019, Chao, 2016). A hydraulic system functioning at such elevated pressures, especially when

incorporating moving parts for energy retrieval, can become intricate and susceptible to failures (Falcão et al., 2018).

Another limitation is that this OTEC-PCM version exclusively serves as an EHM, without utilizing PCM to propel UGs directly. As delineated in Section 2.1.2, the mechanical energy harnessed by PCM could be directed to drive UGs, achieving potential energy conservations of up to 85% for UGs. Where PCM in OTEC-PCM deployed for propulsion, the resultant energy savings could be channeled to outfit UGs with high-powered marine environment detectors or to further amplify UGs' operational span and reach.

Recognizing these potential benefits, Teledyne Marine pioneered a dual-purpose OTEC-PCM, which doubles as a thermal buoyancy engine. This innovative OTEC-PCM design has been integrated into Slocum Thermal E-Twin, as illustrated in Figure 2-17.

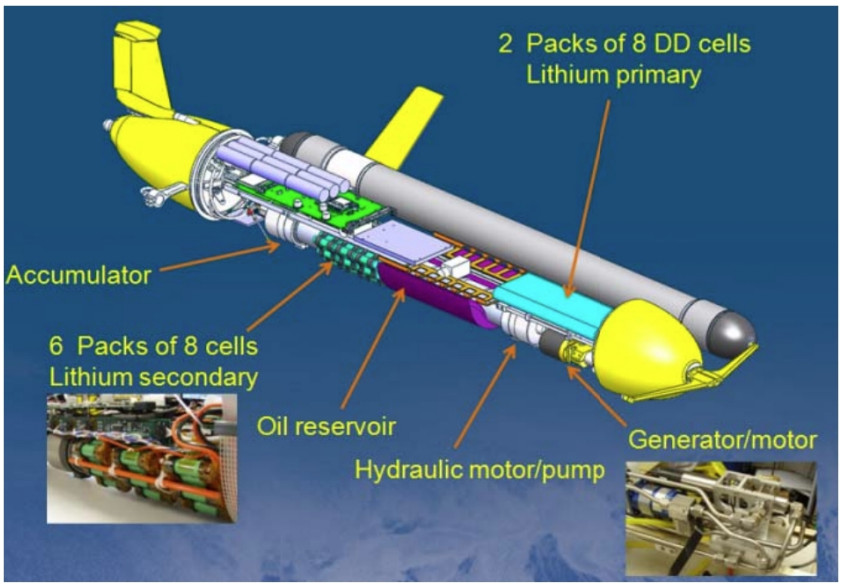

Figure 2-17. Dual-purpose OTEC-PCM integration in Slocum Thermal E-Twin (Jones et al., 2014)

The underlying mechanism of the dual-purpose OTEC-PCM revolves around integrating a mini generator into the high-pressure oil pipeline of the thermal buoyancy engines, which is elaborated upon in Section 2.3.1. Equipped with two major heat exchangers, the dual-purpose OTEC-PCM

can accumulate an average of 1.8 Wh of energy per dive/ascent cycle (Haldeman et al., 2015). Given that a portion of the mechanical energy from OTEC-PCM is harnessed for UGs propulsion, considerably conserving energy, Slocum Thermal E-Twin has the potential to operate as a truly global-class glider with extended endurance spanning multiple years (Jones et al., 2014).

The dual-purpose OTEC-PCM grapples with two key issues. Firstly, there is the necessity for a considerable quantity of PCM, underscored by the presence of the two sizeable heat exchangers. The drag created by these heat exchangers cannot be overlooked during UGs' operations. However, the predominant challenge is the system's reliability. As previously highlighted, the mini turbine's function within an oil circuit can culminate in an intricate system prone to malfunctions (Falcão et al., 2018). A malfunction or damage to the mini hydrodynamic turbine, potentially leading to an obstruction in the oil circuit, would pose a significant risk to UGs. Under such circumstances, UGs might be pulled into the ocean depths by gravity, exposing it to the deleterious impacts of extreme underwater pressure. In light of these challenges, NASA has put forward a turbine-based EHM proposition aiming to bolster UGs' reliability and multifunctionality.

2.2.2 NASA's turbine-based EHM

Drawing from the preceding section, the established OTEC-PCM employed in Thermal UGs produce electricity by incorporating a mini hydrodynamic turbine within the oil circuit of the thermal engine. This design inevitably leads to a system that is intricate and susceptible to breakdowns. An effective remedy for this complication is the external placement of the turbine, beyond UG hull.

In 2006, NASA unveiled a patent detailing an innovative OTEC-PCM approach for Thermal UGs endowed with certain propulsive capabilities (Chao, 2006). To distinguish this variant from other OTEC-PCM, this study dubs it turbine-based EHM. As touched upon earlier, thermal buoyancy engines can transmute thermal energy in seawater into mechanical energy. This mechanical energy then generates ballast forces, which facilitate UGs gliding movement within the ocean. The essence of EHM is the integration of a turbine at Thermal UGs' rear. This turbine harnesses energy from

UGs gliding trajectory, converting it to electric power which then energizes UGs when in energy harvesting mode, as depicted in Figure 2-18.

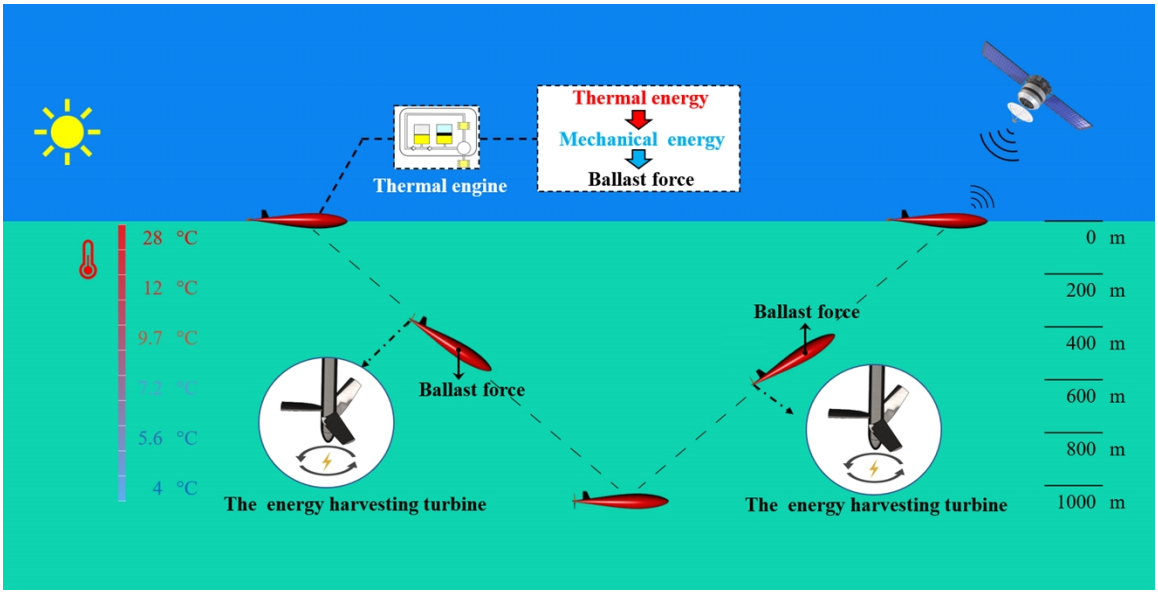

Figure 2-18. NASA's turbine-based EHM in energy harvesting mode

Compared to the dual-purpose OTEC-PCM of Slocum Thermal E-Twin, The turbine-based EHM offers superior reliability and survivability. The primary reason for this is that the turbine in the turbine-based EHM is positioned outside the intricacies of the high-pressure hydraulic circuit. Thus, even if the turbine encounters a mechanical failure, the entire system does not face an elevated risk.

Another merit of the turbine-based EHM is its potential for easy adaptation as an auxiliary propeller-based propulsion module (Chao, 2006). Fundamentally, it already incorporates the two primary elements intrinsic to a propeller-based propulsion system: a motor and a propeller.

On one side, EHM inherently features a motor. This is rooted in the understanding that a generator can function as a motor due to Faraday's law of electromagnetic induction. This law posits that a machine capable of transforming mechanical energy into electrical energy can also work inversely, converting electrical energy back into mechanical energy. When a generator takes on the role of a motor, this mode is termed as 'motor operation' or 'motoring'. By directing electrical power to the

generator's stator windings, an electromagnetic field forms, inducing torque in the rotor which prompts its rotation. Such rotation can be harnessed to drive mechanical components or systems. This principle is solidly grounded in physics, having undergone extensive study and validation (J Chapman, 2004, Sen, 2021). Indeed, the principle has found wide application in wind/tidal turbines. Many wind turbine designs employ the generator as a motor to kickstart the turbine in conditions of low wind speeds. Such dual-functional generators are typically dubbed doubly-fed induction generators (DFIG) (Abad et al., 2011, Muller et al., 2002, Torkaman et al., 2018). Initially, an external power supply propels the generator (acting as a motor) to rotate the turbine blades and foster airflow. Once the turbine gains momentum and wind speeds rise, the generator shifts gears, acting to transform the kinetic energy of the wind into electrical energy (Chowdhury et al., 2006, Gupta et al., 2013, Torkaman et al., 2018).

Conversely, by integrating a pitch-altering mechanism into the turbine blade, the turbine can be readily converted into a propeller. This pitch-altering mechanism is already advanced, cost-effective, and does not necessitate added research and design expenses. A quintessential pitch-changing mechanism is delineated in Figure 2-19. In truth, this dual-role propeller/turbine is not groundbreaking. It has found applications in various marine settings, like sailing boats and yachts, to cite a few examples (Liu et al., 2018).

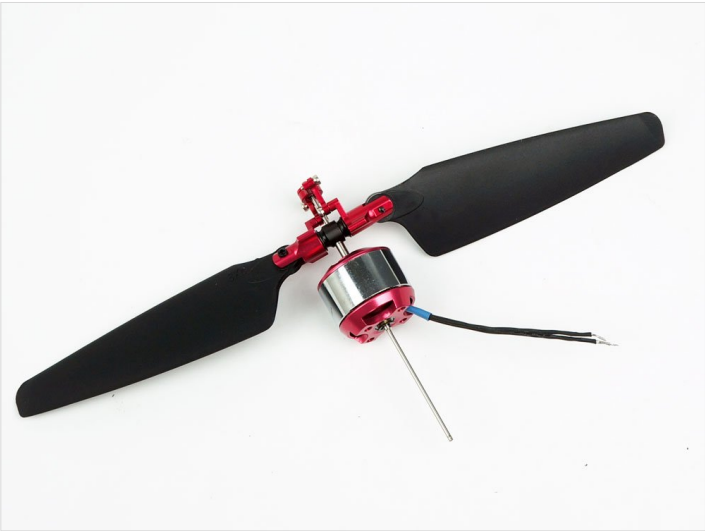

Figure 2-19. Typical pitch-changing mechanism (Amazon, 2023)

Equipped with propeller-based propulsion, UGs can maintain a specific depth, significantly enhancing their mission capability (Jones et al., 2014), as shown in Figure 2-20.

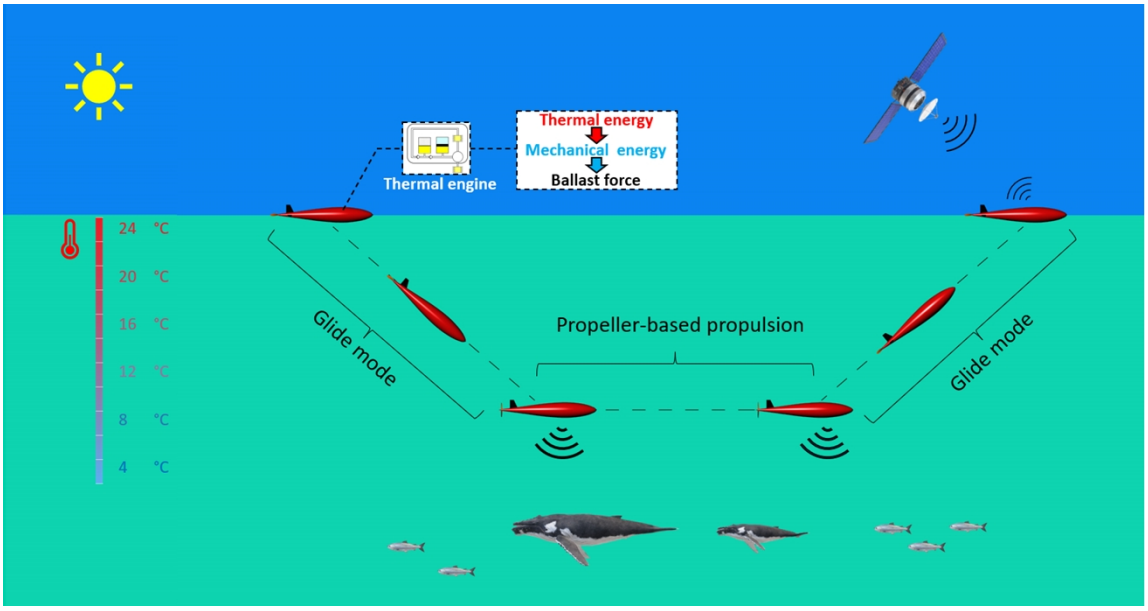

Figure 2-20. UGs with expanded mission capability

UGs outfitted with the turbine-based EHM essentially amalgamates characteristics of Thermal UGs, Hybrid UGs, and UGs with OTEC-PCM, as detailed in Section 2.1.2. By integrating the benefits of these three types of UGs, UGs' range can be elevated to a Global Class, and their mission capability can be substantially broadened. Therefore, the turbine-based EHM represents a compelling trajectory for the advancement of UGs.

Considering the various advantages of the turbine-based EHM mentioned above, the Ph.D. project will engage in an in-depth optimization and exploration of this concept. However, two primary challenges tied to the turbine-based EHM currently constrain its applicability.

The initial challenge is rooted in UGs' modest gliding velocity, which hovers between 0.25 m/s to 0.5 m/s. When factoring in the resistance introduced by the turbine during its energy harvesting mode, this speed drops even further. At these diminished speeds, the turbine blades' leisurely motion through water results in an exceedingly low Reynolds number (Re). Consequently, the

emergence of a laminar separation bubble (LSB) on the foil becomes an inevitable occurrence (Munson et al., 1995, Burton et al., 2011, Schlichting et al., 1961). The presence of an LSB can profoundly modify the flow dynamics over the turbine blades, precipitating an array of performance complications (Lissaman, 1983, Marxen et al., 2003). UGs' limited gliding speed is primarily attributable to the constraints imposed by its internal thermal buoyancy engines. Although this engine produces the ballast force propelling UGs and dictates its pace, the finite ballast force it can muster results in a slower UGs movement in the water, limiting the kinetic energy available for the turbine to harvest.

The subsequent challenge relates directly to EHM's turbine. As the turbine translates kinetic energy from the fluid movement into hydrodynamic output—which generators then convert into electricity—it determines the fraction of kinetic energy from the thermal buoyancy engines that can be harnessed. Evidently, the research demands an efficient turbine. However, the design rationale for a turbine operating under this specific scenario remains elusive and requires elucidation. Both challenges will receive comprehensive coverage in Sections 2.3 and 2.4.

Moreover, during UGs' gliding phase, having a spinning turbine at its rear could jeopardize its stability, amplifying the risk of wing stalls. Should the wings stall, UGs might find it challenging, if not impossible, to regain stability, causing it to plummet into the ocean depths where extreme pressures could wreak havoc on its structure.

2.2.3 Summary

Section 2.2 examined the various categories of existing OTECs utilized in UGs, encompassing their fundamental principles, benefits, and constraints. A comparative analysis of these OTECs is presented in Table 2-1. Subsequently, NASA's turbine-based EHM, which is the focal point of this research, is detailed. UGs equipped with the turbine-based EHM fundamentally merge aspects of Thermal UGs, Hybrid UGs, and UGs with OTEC-PCM. The turbine-based EHM equips UGs with the theoretical capability to be self-sustaining, allowing them to persist indefinitely in the ocean, barring the lifespan limitations of its components. This also enhances UGs' mission

potential. However, this system's practicality hinges on the development of a thermal buoyancy engine capable of generating a greater ballast force, which would result in an increased gliding velocity. Additionally, the design rationale of the turbine within this EHM necessitates deeper exploration.

Table 2-1: Comparison of different OTECs

Comparisons	Advantage	Disadvantage	kJ/kg PCM
OTEC based on the thermoelectric generator (TEG)	High reliability	Expensive Low efficiency	0.2
OTEC based on the expansion of PCM (OTEC-PCM)	Mature	Low reliability Low mission capability	1.12 (highest)
NASA's turbine-based EHM	Theoretically high reliability High mission capability No extra modification	Not mature	NA

2.3 Thermal buoyancy engines in the turbine-based EHM

2.3.1 Principle of the thermal buoyancy engines

The ocean's thermocline is a distinct layer that divides the sea into a warmer surface region and a colder deep region. As one descends through this layer, there is a swift decrease in temperature. As depicted in Figure 2-21, a typical distribution of seawater temperature shows the temperature plummeting rapidly from 20℃ to 30℃ at the surface to approximately 4℃ in the deeper regions due to the influence of the ocean thermocline (Kong et al., 2010). This temperature gradient between the surface and the deeper layers results in the formation of the ocean's thermal energy (Ma et al., 2016). The thermal buoyancy engines capitalize on this ocean thermal energy through the use of PCM. This mechanism harnesses the thermal energy to alter its buoyancy, thereby enabling UGs to ascend and descend in the water column (Yang et al., 2016).

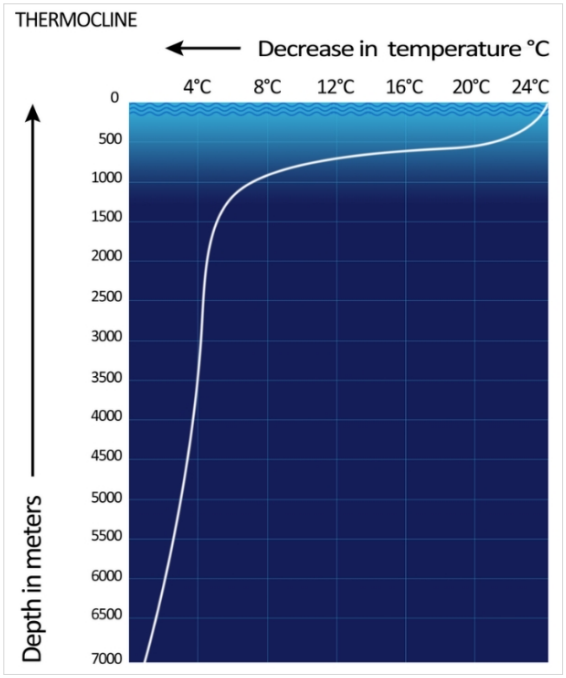

Figure 2-21. Thermocline temperature distribution of seawater (Wikipedia, 2014)

Almost all existing thermal engines are configured based on the principles of the thermal engine system found in SLOCUM (Webb et al., 2001), as depicted in Figure 2-22. In this thesis, such engines are termed 'traditional thermal buoyancy engines'. The traditional thermal engine primarily composes of a heat transfer, an accumulator, inner, and outer bladders, two check valves, and a 3-way valve.

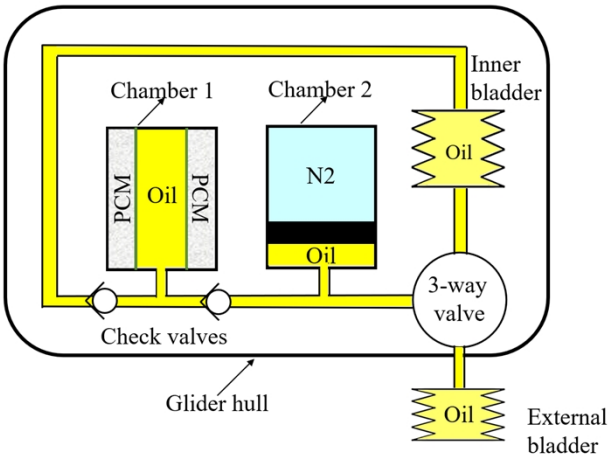

Figure 2-22. Schematic of traditional thermal engine system (Webb et al., 2001)

Heat transfer has various forms, the most prevalent configuration is depicted in Figure 2-22 and includes a metal pressure shell, a flexible tube, and hydraulic oil. PCM is placed between the pressure shell and the flexible tube, while the flexible tube is filled with hydraulic oil. As UGs move between the sea surface and deeper waters, PCM phase and volume change in accordance with the temperature variations. When UGs are near the sea surface, PCM melts and expands, pushing the oil within the flexible tube into the accumulator.

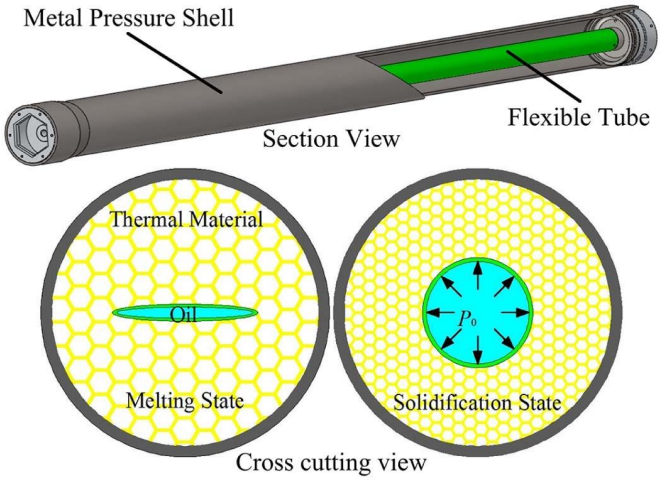

Figure 2-23. Most common structure of heat transfer (Yang et al., 2016)

The accumulator serves as a mechanical energy storage device. As illustrated in Figure 2-24, it typically consists of a pressure shell, a gas bladder filled with high-pressure N_2, and hydraulic oil situated between the shell and the bladder. When the heat transfer forces the hydraulic oil into the accumulator, N_2 within the gas bladder gets compressed, leading to an increase in pressure. After all the oil has entered the accumulator, the magnetic valve closes to maintain the stored pressure and mechanical energy. Once UGs descend to the designated depth, the magnetic valve opens, releasing the stored mechanical energy, which then drives the oil out, generating buoyancy.

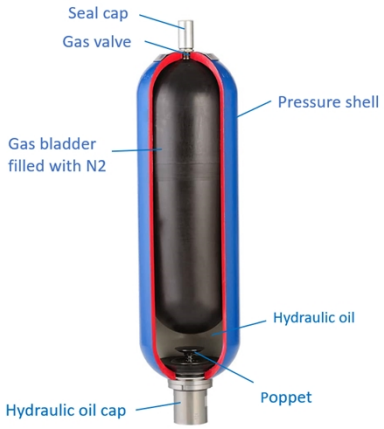

Figure 2-24. Mechanical energy storage accumulator (Parker, 2023)

Both the inner and outer bladders are constructed from rubber, as shown in Figure 2-25.

Figure 2-25. Rubber oil bladder (Aliexpress, 2022)

As depicted in Figure 2-26, the check valve is a component that can be attached to the oil tube. It acts as a one-way valve, allowing the flow to exit but preventing its return. When pressure is applied, the valve opens. It plays a vital role in traditional thermal buoyancy engines by ensuring the directionality of the oil flow.

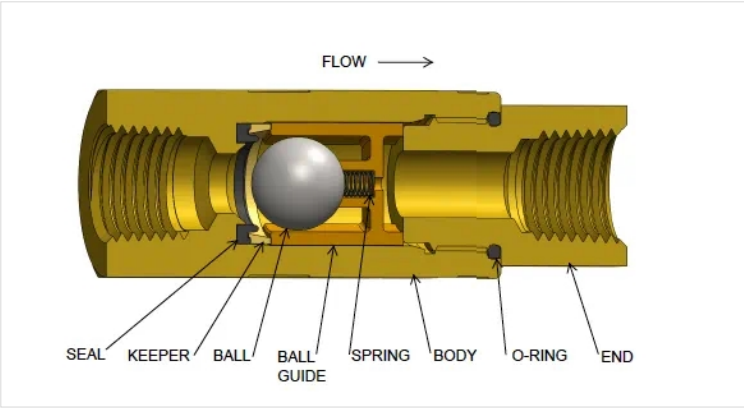

Figure 2-26. Check valve structure (Globalspec, 2022)

As illustrated in Figure 2-27, the 3-way valve is a type of magnetic valve equipped with three ports, each connected to a separate pipe. Through programming, the 3-way valve can regulate the flow direction.

Figure 2-27. 3-way valve (RS, 2022)According to the working principle of the thermal engine, the entire working cycle can be divided into four steps, as shown in Figure 2-28.

In Step 1, when UGs are at the sea surface, PCM within the heat transfer starts to melt and expand. As this expansion occurs, it squeezes the oil from the heat transfer unit and into the accumulator. The check valve prevents the backflow of the oil.

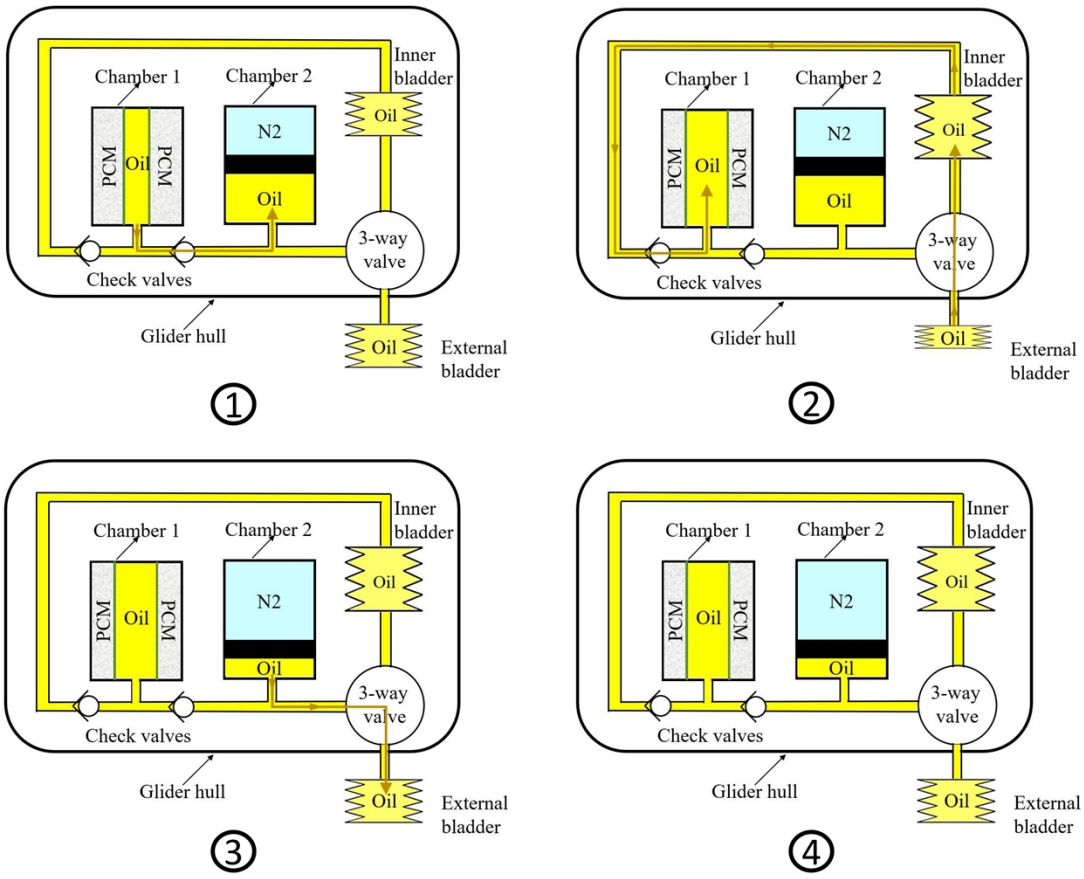

Figure 2-28. Thermal buoyancy engines working cycle

In Step 2, with the opening of the 3-way valve, atmospheric pressure pushes the oil from the external bladder into the internal bladder. As a result, the buoyancy reduces, causing UGs to descend. As the descent deepens, the surrounding water temperature drops, causing the liquid PCM in the heat transfer unit to solidify and shrink. This contraction prompts the oil in the internal bladder to flow back into the heat transfer unit.

In step 3, upon reaching its designated depth, the 3-way valve opens, enabling the oil in the accumulator to be driven into the external bladder. Subsequently, the buoyancy increases, initiating UGs' ascent.

Lastly, Step 4 witnesses UGs reaching the sea surface, thereby paving the way for the commencement of the subsequent cycle (Webb et al., 2001).

2.3.2 Challenge of applying traditional thermal buoyancy engines to the EHM

The traditional thermal buoyancy engines are primarily favored for their straightforward design and reliability. However, they have a major limitation: the low ballast force they can produce. For example, Slocum thermal E-twin, fitted with two heat transfer units, can only produce around 1000 cc of pressurized working oil, which translates to a mere 10 N of buoyancy force (Jones et al., 2014). Such low ballast force is typically adequate for conventional Thermal UGs, given their modest requirements for ballast force and operational velocities. However, when considering the turbine-based EHM, this constraint is a significant hindrance. As previously discussed, a low ballast force curtails the kinetic energy that the turbine can harness. Moreover, the reduced velocity, a consequence of the inadequate ballast force, forces the turbine foils to function at a low Re. This condition, in turn, results in compromised hydrodynamic performance (Deters et al., 2014, Li, 2013).

The limited ballast force can be attributed to two primary factors. First, there is a spatial limitation on the volume of PCM that UGs can accommodate due to the inherent compactness of the system. Secondly, the traditional thermal buoyancy engines do not capitalize fully on PCM's capability to transform thermal energy into mechanical energy. Consequently, PCM's inefficiency cascades down to the overall system inefficiency. The subsequent section delves into the root causes of this PCM inefficiency.

Two primary factors account for the inefficient use of PCM in traditional thermal buoyancy engines. Firstly, there is the issue of non-optimal working pressure at which PCM translates thermal energy into mechanical energy. Typically, UGs operate at depths of around 1000 m, subjecting them to water pressures close to 10 MPa. To push out oil from UG hull, N_2 pressure within the accumulator has to exceed this water pressure, typically rising to approximately 12 MPa (Ma et al., 2016). In conventional thermal buoyancy engines, PCM's operational pressure during its melting and expansion phases closely matches this N_2 pressure, averaging around 12 MPa. However, PCM

is capable of generating considerably higher pressures during their melting phase. To illustrate, paraffin wax can achieve a volumetric expansion rate of 9% under a pressure of 60 MPa (Klintberg et al., 2002). Pressure-Volume-Temperature (PVT) relationship, as shown in Figure 2-29, highlights that n-Tetratetracotane can sustain significant volume expansion even at external pressures up to 100 MPa. Further studies have shown that n-Pentadecane, when used in a thermal buoyancy engine, achieves its peak cycle efficiency at an operational pressure of 90 MPa. This pressure is nearly nine times higher than the top working pressure of PCM in a standard thermal buoyancy engine (Falcão et al., 2016). As a result of this discrepancy, the pressure generated by expanding PCM remains underleveraged, causing suboptimal PCM utilization.

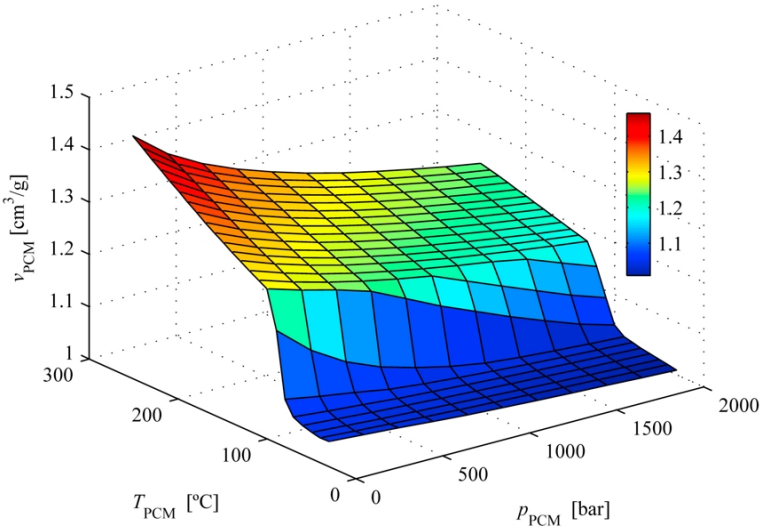

Figure 2-29. Global PVT surface for n-Tetratetracotane (Falcão et al.)

A second factor contributing to inefficiency stems from the porous structure of PCM when subjected to low pressure. This porosity is primarily determined by the internal air pressure within the hull. As depicted in Figure 2-28, during the second step of the thermal buoyancy engines' operational cycle, PCM undergoes solidification and contraction. The prevailing air pressure inside the glider hull then prompts the transfer of oil from the inner bladder into the heat exchanger. This internal air pressure gives rise to varying levels of PCM porosity, which in turn impacts the circulation of the hydraulic oil by limiting the available volume within the heat exchanger (Yang

et al., 2016). Elevated internal air pressures could mitigate porosity, thereby enhancing the efficacy of PCM. However, in traditional thermal buoyancy engines, there exists a constraint on the attainable internal air pressure. As noted earlier, during the first phase of the working cycle, the oil is driven into UG hull by the ambient atmospheric pressure at sea level. This necessitates that the atmospheric pressure always exceeds the internal air pressure within UG hull. As a result, the maximum feasible air pressure inside UG hull caps at roughly 1 atm. This restriction induces unavoidable porosity and suboptimal PCM performance. A conceivable remedy involves integrating a supercharger within UG hull to facilitate the transfer of oil from the inner bladder back into the heat exchanger (Yang et al., 2016). Nevertheless, the incorporation of such a supercharger would elevate the system's energy demands and could undermine its overall reliability.

To render the turbine-based EHM practical, an objective is enhancing the ballast force of the thermal buoyancy engines without increasing PCM load. To achieve this, the focus of this research is to increase the low cycle efficiency of PCM. As discussed earlier, the suboptimal working pressure of PCM is a factor that hinders its cycle efficiency, thereby diminishing the comprehensive efficiency of the system. To mitigate this limitation, Falcão proposes elevating the working pressure of PCM and introducing a high-to-low pressure transition mechanism at the junction of PCM and hydraulic circuit as a potential remedy (Falcão et al., 2016). However, a functional design has to be materialized, indicating the necessity for a comprehensive redesign of the thermal buoyancy engines. Furthermore, to address the secondary efficiency bottleneck—porosity in PCM due to the low internal air pressure within the hull—a solution for optimizing the internal air pressure is required.

2.3.3 Summary

Section 2.3 delves into the foundational principles of the thermal buoyancy engines, leveraging PCM's ability to transmute thermal energy into mechanical energy to drive UGs. However, traditional designs of these engines yield restricted ballast force, primarily owing to suboptimal

PCM performance. While such limitations might be tolerable for standard Thermal UGs, they pose challenges for the turbine-based EHM as delineated in this research. The restricted ballast force results in a dearth of kinetic energy available for turbine extraction and compels the turbine to operate at a disadvantageous low Re. For the realization of a functional turbine-based EHM, it is imperative to innovate a thermal buoyancy engine that can produce augmented ballast force without necessitating an increase in PCM content. Attaining this entails optimizing the cycle efficiency of PCM within the engine's architecture.

2.4 Turbine in the turbine-based EHM

As depicted in Figure 2-18, the turbine used in this EHM is essentially a HAT. This section is to provide an overview of the prevailing advancements in HATs and discuss the challenges related to their application into the turbine-based EHM proposed in this study.

2.4.1 HAT

Wind/tidal turbines are mechanisms that transform the kinetic energy of moving air or water into rotational mechanical energy. This rotational energy is subsequently transduced into electrical power via a generator. The inaugural wind turbine with the capability to produce electric power was pioneered by Scottish scholar James Blyth in 1887. Since this groundbreaking innovation, the realms of wind and tidal energy have become increasingly pivotal in modern life. Presently, there are two predominant types of turbines: HAT and vertical axis turbine (VAT). Among them, HAT enjoys wider application due to its higher power coefficients, straightforward architecture, consistent rotation, and inherent self-starting capability (Das et al., 2022). Representative examples of wind and tidal HATs can be seen in Figure 2-30.

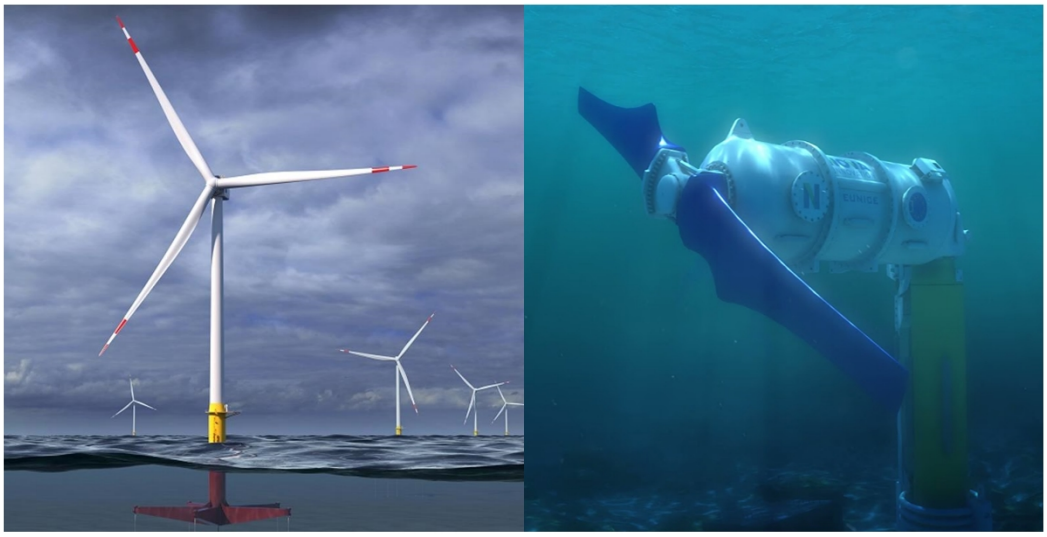

(a) (b)

Figure 2-30. HAT in: (a) Wind energy; and (b) Tidal energy (reproduced from (Nova, 2021) and (GE, 2021))

2.4.2 BEMT-based turbine design method

Most of the contemporary HATs are designed using BEMT. BEMT melds two components: Blade element theory (BET) and the actuator (or momentum) theory (Wang et al., 2022), as introduced in the following section.

BET

BET traces its origins to the work of Polish scientist Stefan Drzewiecki (Drzewiecki, 1920), and its development was later augmented by William Froude (Froude, 1878). Initially conceptualized for propellers, BET has since been adapted for turbines. Central to this theory is the decomposition of blades into discrete portions termed blade elements, as depicted in Figure 2-31. Each segment is treated as an autonomous two-dimensional (2D) foil, facilitating the calculation of hydrodynamic forces based on localized flow conditions at each blade element. Upon determining the hydrodynamic properties for each segment, they are collated to ascertain the holistic hydrodynamic performance of HAT (Gudmundsson, 2014).

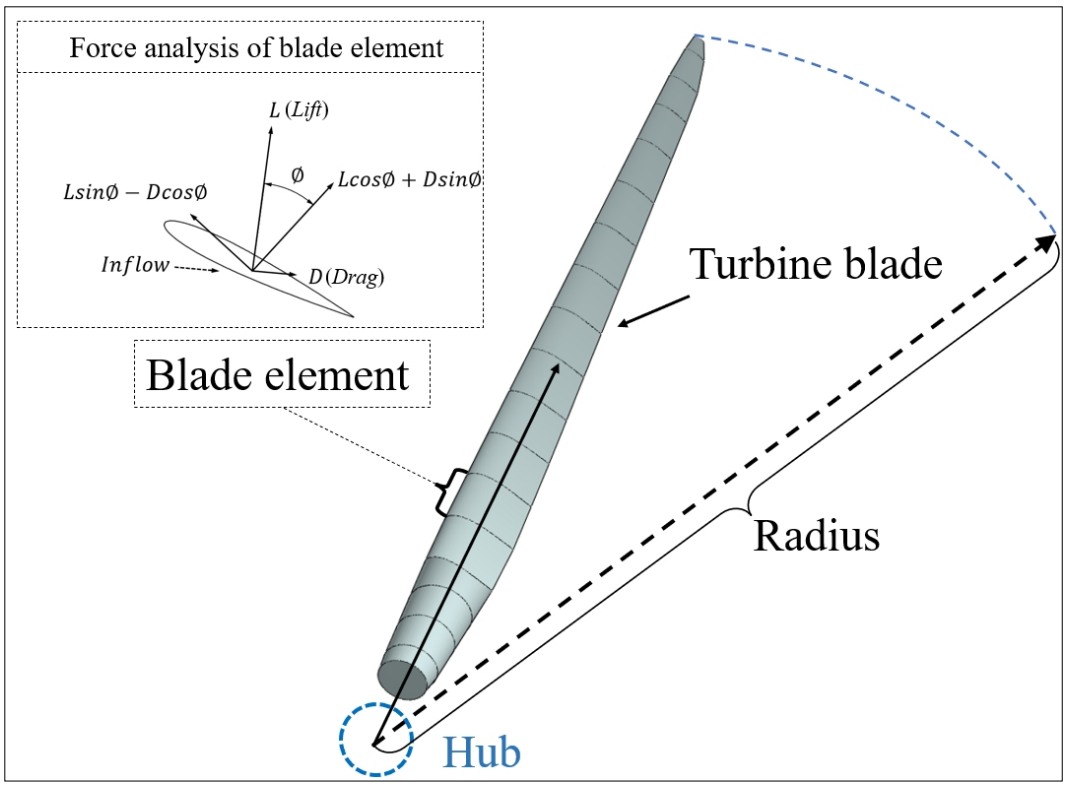

Figure 2-31. BET (Produced from the software Qblade)

BET presents several advantages in the realm of turbine design. Notably, it can account for diverse foil geometries, twist angles, angles of attack (AoA), and hydrodynamic attributes. It is especially adept at computing the torque and thrust of a turbine. Moreover, BET is conducive to modeling pivotal nonlinearities, such as those in lift and drag curves.

However, BET is not without its limitations. Specifically, it operates under the presumption that forces exerted on each blade element are 2D, consequently sidelining spanwise flow and the intricate interplay of forces between the elements. An additional oversight of BET is its inability to account for the induced flow within the stream-tube. Such an omission might culminate in an exaggerated estimation of hydrodynamic forces when juxtaposed with experimental outcomes under identical conditions.

Momentum theory (Actuator disk theory)

The momentum theory, often referred to as the actuator disk theory, was first conceptualized by (Rankine, 1865) for propellers, and subsequently modified for turbines, as illustrated in Figure 2-32. Betz further refined this approach by introducing a streamlined actuator disc model (Betz, 1920). Within this paradigm, the turbine is abstracted as a one-dimensional actuator disc that interrupts fluid pressure continuity as it navigates through the turbine, thereby siphoning energy from the flow (Zhao et al., 2019, Dixon et al., 2010). This model zeroes in on the momentum exchange occurring between the flow and the disc along the axial trajectory (De Lellis et al., 2018). By amalgamating the load in the orthogonal direction, the resultant thrust can be ascertained (Hansen, 2017).

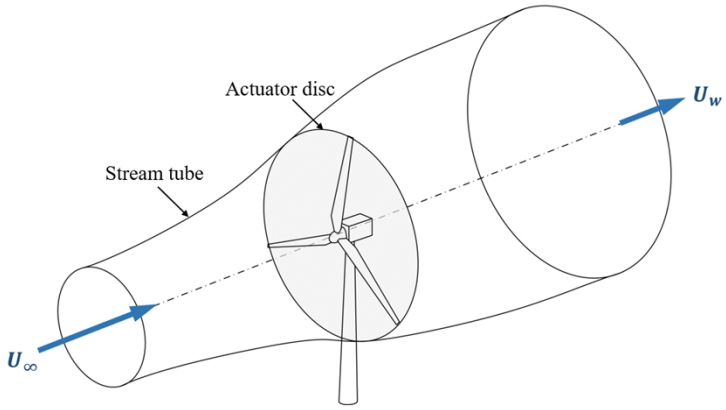

Figure 2-32. Simplified actuator disc and stream-tube model (Branlard, 2008)

The actuator theory is based on the following assumptions (Dixon et al., 2010, Gudmundsson, 2014):

- The flow through the actuator disc is uniform and subjected to a consistent load, resulting in a uniform acceleration of the air.
- The flow is assumed to be incompressible and inviscid, implying there is no drag or momentum diffusion.
- Both upstream and downstream of the actuator disc, the flow is contained within the boundary of the stream-tube.
- The flow external to the stream-tube maintains a constant stagnation pressure.

- The rotation induced in the flow by the turbine is ignored.
- A distinct control volume surrounds the stream-tube, effectively separating the flow inside from the surrounding air.

Despite its conceptual simplicity, the actuator disc model yields beneficial approximations. Betz's contributions to this model in 1920 were particularly noteworthy: he posited a theoretical maximum for the turbine's power coefficient (C_p) at 59.3%—now commonly referred to as the Betz limit. To attain this limit, the actuator disc should diminish the velocity of the incoming flow by 1/3 in its proximity (Betz, 1920). This proportional reduction in axial flow velocity, when compared between the upstream and the turbine rotor, is termed the axial induction factor a . As such, the assertion that $a = 1/3$ has become foundational in contemporary turbine design. When embarking on turbine design via BEMT, designers typically start with the presumption that the turbine can reduce the axial flow velocity by 1/3.

BEMT

BEMT combines BET and the actuator disc theory. This fusion was originally developed by (Glauert, 1935).

While BET assumes that blade elements are 2D and that the effective inflow velocity is a vector sum of the rotational velocity and incoming velocity, BEMT takes it a step further. It considers the induced velocities resulting from the aerodynamic blade loads (Hansen, 2017). Using BEMT analysis, one can construct the velocity triangle for a blade element, as demonstrated in Figure 2-33. Where W is the relative velocity; U_∞ is the incoming velocity of the flow; r is the local radius of the blade element; R is the radius of the turbine; λ is TSR; and ϕ , α , and β are the inflow angle, angle of attack, and the twist angle, respectively. The axial induced velocity is denoted as aU_∞ ; the tangential induced factor is denoted as a' ; and the tangential induced velocity is denoted as $a'U_\infty \lambda \frac{r}{R}$.

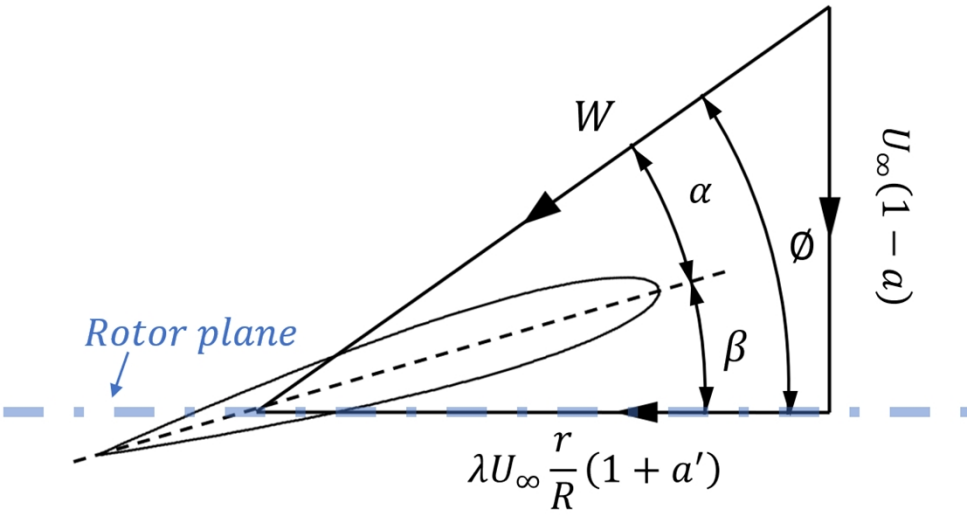

Figure 2-33. Velocity triangle of a blade element

Given the lift and drag coefficients for 2D foil in relation to the angle of attack, the magnitude and direction of the inflow velocity can be determined from the velocity triangle once the induced velocity is ascertained. This, in turn, enables calculation of the load on the foil. The primary challenge is to estimate these induced velocities. To tackle this, BEMT utilizes BET to segment the turbine blade into multiple discrete elements. It assumes that forces exerted on these blade segments are exclusively based on the lift and drag coefficients of the foil. Further, BEMT deploys momentum theory to equate changes in the flow's linear and angular momentum to the blade element thrust and torque previously computed. This process facilitates the calculation of induced velocities on the blades (Liu et al., 2012).

BEMT is instrumental in designing turbines, such as the one featured in EHM. As alluded to in the actuator theory, Betz stipulated that to reach the Betz limit, the axial induction factor a should be 1/3 (Betz, 1920). When crafting a turbine using BEMT, designers typically commence by assuming a 1/3 reduction in axial flow velocity. With this foundational assumption, one can quantify the momentum shift in the stream-tube. Subsequently, the optimal twist angle and chord length for the turbine can be deduced based on the selected foil profile. Comprehensive details on this design approach are provided in the upcoming methodology section (Section 2.5.1.1).

The design methodology described is predominantly employed for preliminary design in contemporary settings, given that the actuator disk theory does not perfectly represent the flow dynamics around the turbine, and it sidesteps several pragmatic engineering challenges. In real-world scenarios, a myriad of considerations come into play when crafting a turbine. For example, the turbine's structural integrity is paramount. Many turbines are intentionally designed with an axial induction factor a of 0.28, slightly deviating from the optimal value of 1/3. This design choice significantly reduces the load while only marginally compromising the energy output (Corten et al., 2008). Furthermore, considerations extend to the interactions between turbines situated within a wind farm. An emerging strategy to amplify the cumulative energy output of a wind farm involves curbing the energy production of upwind turbines by modulating their axial induction factor. This tactic allows turbines positioned downstream to harness a greater proportion of the energy. This approach is termed axial induction control (AIC) (Boersma et al., 2017, Hoek et al., 2019, Houck et al., 2022). Another vital aspect in turbine design is tip loss. There are established methodologies that integrate tip loss models into the turbine design regimen, enabling the selection of the most efficient turbine configuration (Khchine et al., 2017). Although these sophisticated design strategies, rooted in Betz's actuator disk theory, can be more fitting for particular operational conditions and are both pragmatic and precise, the foundational tenets of turbine design have largely remained unchanged throughout the years.

2.4.3 Challenge of applying BEMT to the turbine design in this research

Different from the traditional turbine, the turbine investigated in this study has distinct features that complicate the use of BEMT for its design. These challenges can be classified into two categories: those arising from the turbine's working conditions and those resulting from its working principle.

2.4.3.1 General challenges stemming from the special working conditions of the turbine

Using the conventional BEMT for turbine design in this study brings forward several key challenges, rooted in the turbine's distinct operational conditions. Firstly, standard BEMT inherently presumes a consistent incoming flow velocity, a premise highlighted in the assumptions

of the actuator theory (Section 2.4.2). In contrast, the actual inflow for the turbine under investigation in this research is characterized by the non-uniform wake trailing UG hull, as graphically portrayed in Figure 2-34. This divergence between BEMT's foundational assumptions and the genuine operating conditions of the turbine might instigate design discrepancies. For instance, there is a potential risk of over-assuming the momentum harnessed by the blade element, leading to an undesirably elongated chord length.

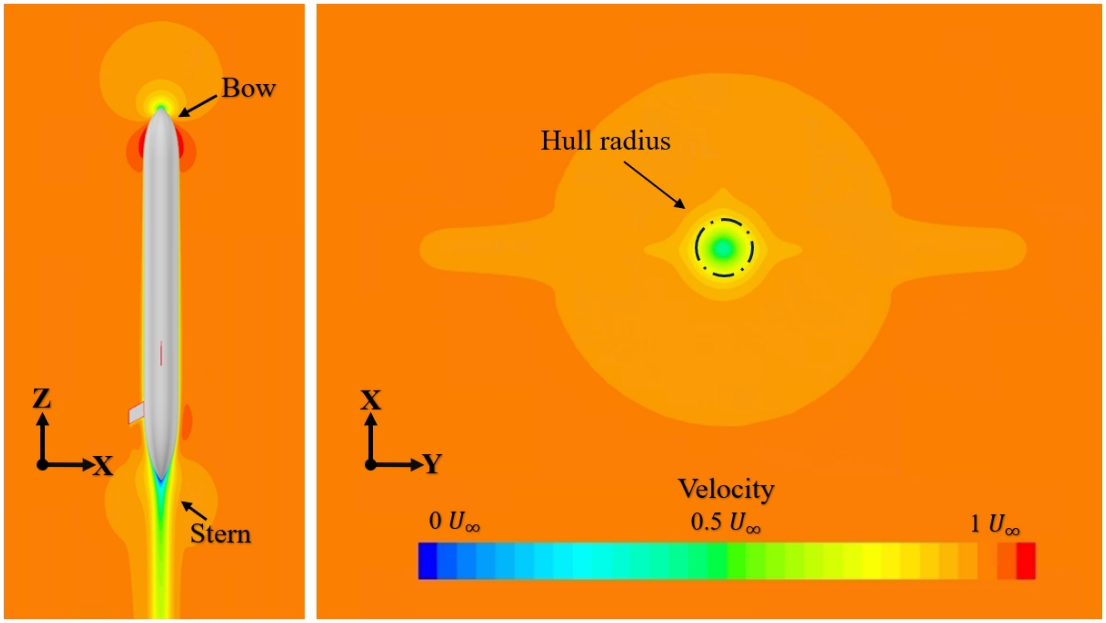

Figure 2-34. Typical wake distribution behind UG: (a) Side view; and (b) Rear view (Produced from STAR CCM+)

The second challenge stems from the low *Re* under which the turbine operates. Given the system's sluggish motion and the influence of the wake, the turbine blades often operate under low *Re* conditions ($Re < 50{,}000$). Under such conditions, the hydrodynamic performance of the blades becomes compromised and is highly sensitive to *Re* (Deters et al., 2014, Li, 2013). This dynamic complicates the turbine design process. The ambiguity surrounding *Re* number, which is paramount in the design process, can pose challenges. If the chosen design *Re* for the foil is significantly different from the actual operational *Re* of the foil, the turbine's performance could

be adversely affected. This is because the momentum captured by the turbine in such scenarios would diverge from the optimal momentum projected by BEMT.

To navigate these inherent challenges and adapt BEMT design methodology to the specificities of the turbine under consideration, certain refinements to BEMT design method might be requisite. It is imperative to highlight that these refinements are solely intended for the design methodology grounded in BEMT. The foundational principles of this refined method continue to align with the traditional BEMT, as delineated in Figure 2-35. Given that both the wake and *Re* intricacies are intrinsically connected to velocity, these two modifications are collectively termed as velocity corrections.

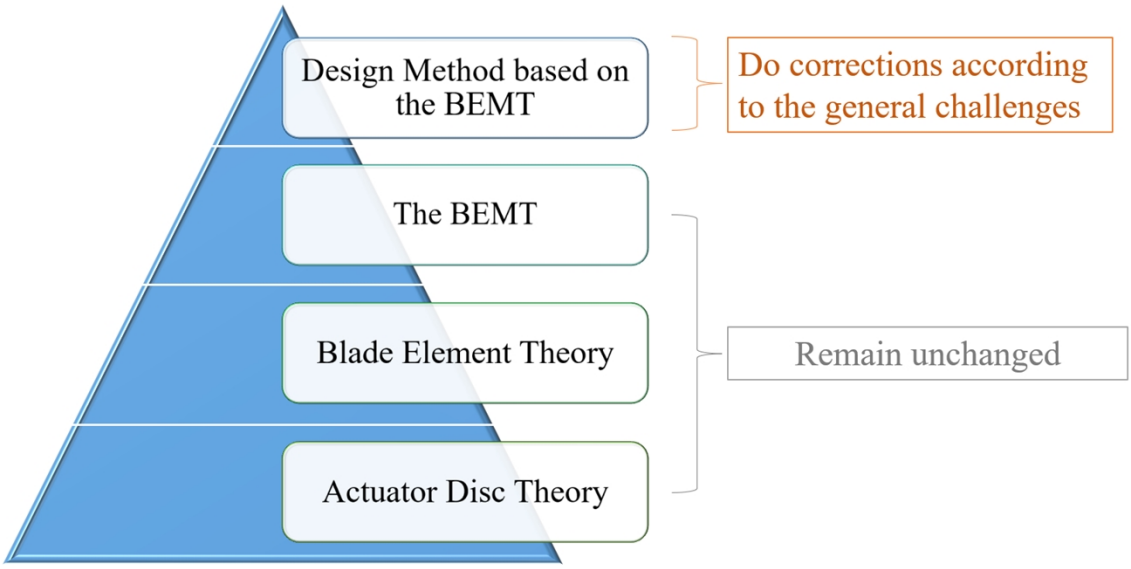

Figure 2-35. Velocity corrections for challenging working conditions

The third challenge pertains to the undefined design philosophy of the turbine. Given that the operational conditions of the turbine in this research deviate from those of traditional turbines, the design approach for the turbine in the turbine-based EHM remains ambiguous. This is particularly true for the selection of the turbine radius and TSR – both of which are pivotal design parameters. To proficiently design turbines using BEMT-centric design approach, an exhaustive examination of the effects of turbine radius and TSR on power and energy yield is essential.

2.4.3.2 Challenges caused by the special working principle of the turbine

The operational principles of the turbine in this study diverge from the foundational concepts that anchor BEMT design method. This divergence introduces difficulties when employing the conventional BEMT-based design approach to delineate the optimal turbine geometry for EHM.

The traditional BEMT-based design method, an offshoot of Betz's actuator disk theory, envisages the turbine as an actuator disk. The actuator disk, as conceived in Betz's theory, possesses two distinguishing attributes: it remains stationary and is propelled by a predefined incoming velocity, as depicted in Figure 2-32. Consequently, the classical BEMT design method is calibrated for stationary turbines spurred by a designated incoming velocity. Such turbines, termed as velocity-driven turbines in this research, are predominant globally.

In this research, the turbine integral to EHM can still be abstracted as an actuator disk. However, in contrast to Betz's concept of the actuator disk, this particular actuator disk is mobile, propelled by force (specifically, the ballast force conferred by the thermal buoyancy engines). As illustrated in Figure 2-18, the turbine is galvanized into motion by the ballast force, which instigates the rotational motion of the turbines. For the purposes of this study, the turbine and its associated actuator disk are designated as the force-to-velocity turbine and force-to-velocity actuator disk, respectively.

While the force-to-velocity turbine might be a less familiar concept, it boasts a storied lineage. The prototype of force-to-velocity turbines was conceptualized as a form of ram air turbine (RAT). A RAT, integrated into aircraft designs, harnesses ram pressure to engender power, serving as an auxiliary power source (Saad et al., 2017, Jian, 2016). During the tumultuous years of World War II, Germany pioneered the creation of the first-ever rocket-propelled fighter, christened as the Messerschmitt Me 163 Komet, depicted in Figure 2-36. To navigate the power supply challenge, a RAT was strategically positioned at its nose. Given that the Messerschmitt Me 163 Komet was impelled by a potent rocket engine, the incident flow induced the rotation of RAT, thereby

energizing the system. This brand of RAT also found application in another rocket-driven fighter, the Mikoyan-Gurevich I-270, developed under the aegis of Soviet Air Forces (Gunston, 2000).

Figure 2-36. Messerschmitt Me 163 Komet and its force-to-velocity turbine (Buuk, 2003)

Figure 2-37. RAT on modern aircraft (9GAG, 2019)

However, as the efficiency and output of turbojet engines advanced, rocket-powered fighter became unnecessary. In contemporary times, RAT is commonly used as an emergency power source on modern aircraft, activated when both primary and auxiliary power systems fail (Saad et al., 2021), as shown in Figure 2-37.

Another application of the force-to-velocity turbine is found in certain mortar shells that are equipped with a small power-generating turbine at their head. These are typically deployed from unmanned helicopter at high altitudes, as depicted in Figure 2-38. As gravity pulls the system downward, the turbine encounters airflow, driving it to generate power for a proximity fuze.

Figure 2-38. Mortar shell with energy harvesting turbine (Andersen, 2017, CCTV, 2019)

It is evident that the working principles of the force-to-velocity actuator disk, which represents the force-to-velocity turbine, deviate from those of Betz's stationary actuator disk, which relies on a designated incoming velocity. Consequently, certain assumptions rooted in Betz's original actuator disk theory, such as the necessity for the axial induction factor a to be 1/3 (Betz, 1920) for maximizing energy yield, might not hold true for our force-to-velocity turbine. Building on this premise, it could be further postulated that the conventional BEMT-based design method, which is grounded in Betz's actuator disc theory, may not be fully suitable for designing the force-to-velocity turbine.

To tailor BEMT for our turbine's specific needs, this research might have to reinterpret and expand upon Betz's actuator disc theory. Using this modified theory as a foundation, the thesis aims to establish a new BEMT-based turbine design methodology specifically for the force-to-velocity turbine. This approach will diverge from the conventional BEMT design process, as depicted in Figure 2-39.

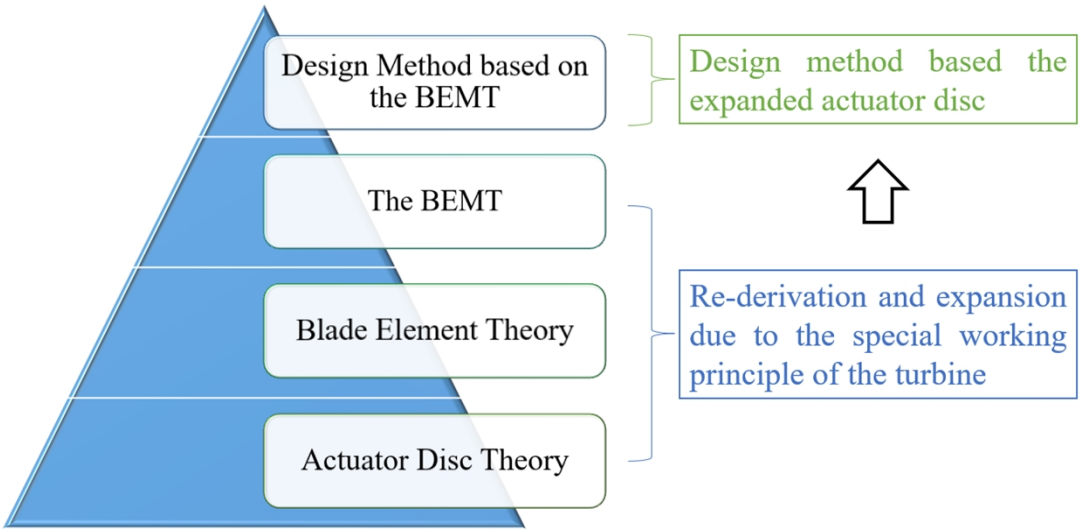

Figure 2-39. New turbine design method based on the expanded actuator disc theory

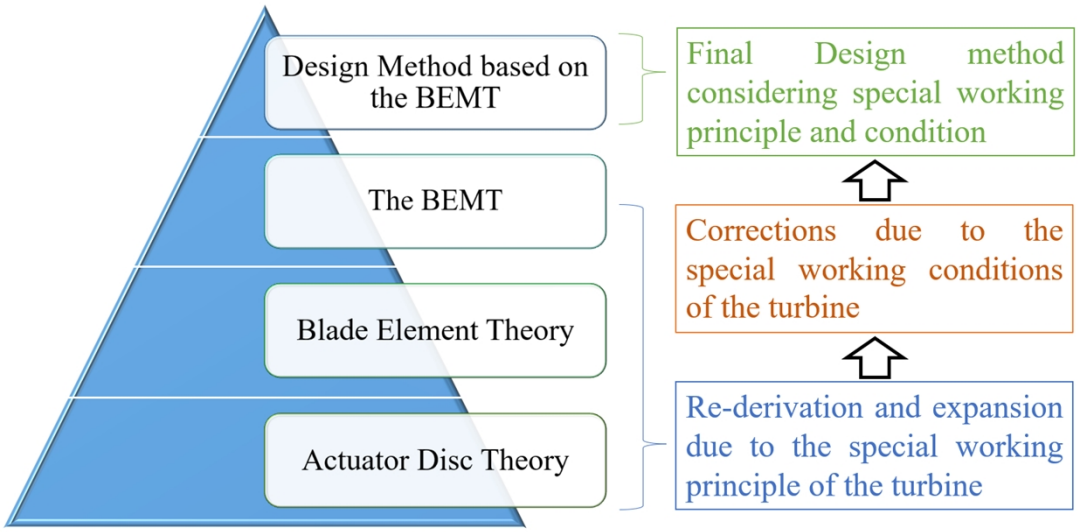

Figure 2-40. Final design method considering both special working principle and special working conditions

Finally, the velocity corrections discussed in Section 2.4.3.1, which were necessitated by the unique operating conditions, will be incorporated into this new turbine design method for the force-to-velocity turbine, as depicted in Figure 2-39. This integration will help formulate a comprehensive design approach tailored for the turbine in EHM for this study, as outlined in Figure 2-40.

2.4.4 Summary

In Section 2.4, various turbine types are explored, emphasizing HAT used within EHM for this research. The intricacies of BEMT and the corresponding turbine design method are elaborated upon. Through a thorough review of preceding studies, several challenges emerge when utilizing the conventional BEMT-based design methodology for the turbine in this study. These challenges can be compartmentalized into two main categories: The first category encompasses general challenges arising from the distinct operating conditions of the turbine, such as the wake generated by the hull and the low *Re* under which it operates. This highlights the need for adjustments to the conventional BEMT-based design approach. Furthermore, given the ambiguous design parameter selection philosophy inherent in BEMT approach, additional investigative research is warranted. The second category centers on the incongruence between the turbine's operating principles and the foundational assumptions of the traditional BEMT-based design approach. Specifically, the turbine in this study operates on a force-to-velocity principle, while the traditional BEMT design is tailored for velocity-driven turbines. This difference indicates that the foundational assumptions of the standard BEMT-based design might not suit the specifics of the turbine in question. Thus, there is a need to expand upon the century-old actuator disc theory and, from this expansion, craft a new turbine design methodology. In culmination, the goal is to introduce a refreshed design methodology that adeptly navigates both highlighted challenge categories, tailored specifically for the turbine within EHM.

2.5 Methodology for the development of the turbine-based EHM

The turbine-based EHM concept introduced in this research is promising, however, the turbine's operational mechanism and design methods remain to be delineated and refined. To advance this concept towards a practical implementation, a methodical approach encompassing both mathematical and numerical techniques is essential. For a deeper understanding of the design philosophy and operational mechanism of the turbine within the turbine-based EHM, this study

will leverage BEMT to formulate a mathematical model. This model will facilitate extensive design evaluations and analyses of the turbine. Following this, the study will employ high-fidelity CFD simulations to validate these outcomes, culminating in the affirmation of the turbine-based EHM's viability.

2.5.1.1 BEMT design and analysis method for the turbine

BEMT design method

As previously discussed, the turbine design method rooted in BEMT is extensively utilized and well-established for modern preliminary turbine design. Central to this method is the initial specification of the axial induction factor a. Betz's theory, detailed in Section 2.4.2, posits that to maximize C_p and energy yield, a should be fixed at a value of 1/3. In this context, the study adopts a_{design} to represent the desired axial induction factor during the design phase, as expressed in Equation 2-1.

$$a_{design} = 1/3 \tag{2-1}$$

As highlighted in the angular momentum theory by Burton et al. (2011), this study delineates the relationship between a and a'. From this, the design tangential induction factor (a'_{design}) can be computed. The correlation between a_{design} and its corresponding tangential induction factor a'_{design} is given in Equation 2-2.

$$a'_{design} = \frac{a_{design}\left(1 - a_{design}\right)}{\lambda_{design}{}^2 \mu^2} \tag{2-2}$$

where λ_{design} is the design TSR; μ is ratio of the local radius r^e to the total radius R, determined as $\frac{r^e}{R}$.

Subsequently, the design inflow angle (ϕ_{design}) can be determined using Equation 2-3 as follows:

$$\phi_{design} = \arctan\left(\frac{1 - a_{design}}{\lambda_{design}\mu\left(1 + a'_{design}\right)}\right) \tag{2-3}$$

The optimal twist angle (β) can be calculated as follows:

$$\beta = \phi - \alpha_{design} \tag{2-4}$$

where a_{design} is the design angle of attack.

Guided by BEMT, the change in angular momentum over time at each sectional radius is equivalent to the torque produced by that segment. This correspondence provides the basis for Equation 2-5, which is used to calculate the chord length (C) as follows:

$$C = \frac{8\pi\lambda_{design}\mu^2 a'_{design}\left(1-a_{design}\right)RU_{\infty}^2}{N\left(C_L sin(\phi) - C_D \cos(\phi)\right)W^2} \tag{2-5}$$

where N is the blade number.

Given that the design parameters for value of C and β are premised on $a_{design} = 1/3$, when the turbine operates under its designated working condition, a for the turbine with the specified C and β should be, or nearly be, 1/3. This aligns with Betz's theory, which posits that this value leads to the highest power coefficient (C_P).

BEMT analysis method

Understanding the design philosophy of the turbine in the turbine-based EHM necessitates extensive design and analysis. BEMT analysis method is favored for its efficiency and lower computational demand. While BEMT may not match the precision of underwater turbine CFD, its capability in optimizing turbine geometry and operation remains significant (Khchine et al., 2017).

In BEMT analysis, iterations determine a and a' induction factors for blade element loading calculations. Initially, both a and a' are set to zero. The inflow angle (ϕ) is derived using Equation 2-3, replacing λ_{design} with the operating TSR ($\lambda_{operating}$). Subsequently, the angle of attack (α) is determined by Equation 2-4, facilitating the calculation of lift (C_L) and drag (C_D) coefficients for each foil segment. Equations 2-6 and 2-7 then compute the tangential (C_t') and normal (C_n) coefficients for each segment.

$$C_n = C_L \cos(\phi) + C_D \sin(\phi) \tag{2-6}$$

and

$$C_t^{'} = C_L \sin(\phi) - C_D \cos(\phi) \tag{2-7}$$

The chord solidity (σ_r) can be determined through Equation 2-8 as follows:

$$\sigma_r = \frac{NC}{2\pi\mu R} \tag{2-8}$$

Given C_n and $C_t^{'}$, a and a' of the flow acting on the foil segment can be calculated through Equations 2-9 to 2-10.

$$a = \frac{1}{\frac{4sin^2(\phi)}{\sigma_r C_n} + 1} \tag{2-9}$$

$$a' = \frac{(1-a)\sigma_r C_t^{'}}{4\lambda_{operating}\mu sin^2\phi} \tag{2-10}$$

The newly calculated a and a' replace the previous a and a' and the calculation procedure restarts. The iteration stops until the residuals of a and a' are less than 0.01 in this study.

Once the iteration is completed, the result from the iteration including W , $C_t^{'}$, and C_n are used to evaluate the torque (δQ) and the thrust (δT_b) for each blade element through Equation 2-11 and Equation 2-12

$$\delta Q = \frac{1}{2}\rho W^2 NCC_t^{'} r^e \delta r \tag{2-11}$$

$$\delta T_b = \frac{1}{2}\rho W^2 NCC_n \delta r \tag{2-12}$$

The overall thrust (T) and power (P) of the turbine can be obtained, for calculating thrust coefficient (C_t) and power coefficient (C_p) through Equations 2-13 to 2-14, respectively.

$$C_p = \frac{P}{\frac{1}{2}\rho U_\infty^3 A_D} \tag{2-13}$$

$$C_t = \frac{T}{\frac{1}{2}\rho U_\infty^2 A_D} \tag{2-14}$$

As outlined in Section 2.4.2, BEMT operates on certain assumptions: steady, inviscid, and incompressible flow, devoid of radial and circumferential dependencies, among others. These assumptions can introduce discrepancies in accuracy. To enhance the precision of BEMT analysis, several typical corrections have been introduced in practical applications, such as Prandtl's tip loss correction (Glauert, 1935; Shen et al., 2005), turbulent wake state correction (Buhl, 2005), and three-dimensional (3D) correction (Chaviaropoulos et al., 2000).

Both the design and analysis using BEMT will be executed in MATLAB (Matrix Laboratory). This platform facilitates matrix manipulation, data visualization, algorithm development, and user interface creation, among other capabilities (Jalalvand et al., 2019). Moreover, MATLAB's proficiency in executing operations like addition, subtraction, multiplication, and division on extensive number sets makes it a suitable choice for computationally demanding tasks (Báez-López et al., 2019).

The computational prowess of MATLAB, when combined with the efficiency of BEMT, paves the way for creating a mathematical model that aids in designing and analyzing a multitude of turbines. Such a methodology is crucial for unravelling the design philosophy behind force-to-velocity turbines in the turbine-based EHM.

2.5.1.2 CFD verification for the mathematical model of EHM

While the mathematical model based on BEMT offers satisfactory accuracy for probing the design philosophy and operational mechanics of the turbine, it provides only an initial assessment of the energy-harvesting capability of EHM. A more detailed evaluation necessitates the use of high-fidelity CFD analysis.

CFD is a numerical methodology developed in the 1950s for simulating and analyzing fluid flow. It has been applied across diverse sectors, encompassing aerodynamics, combustion, propulsion

systems, biomedical engineering, and more. CFD has emerged as an essential instrument for engineers to understand complex fluid dynamics phenomena. It predominantly shines in offering precise solutions for problems too complex for analytical approaches. For instance, CFD can capture the interaction between UG hull and the turbine in the turbine-based EHM, an intricate scenario challenging to simulate solely through a BEMT-based mathematical model.

Numerous commercial CFD software packages, such as Star-CCM+, ANSYS Fluent, and OpenFOAM, have surfaced over the years. Researchers have extensively utilized these tools for examining tidal turbine hydrodynamics, facilitating performance forecasting, and aiding industries in realizing large-scale applications (Amiri et al., 2020, Harrison et al., 2010, Ahmed et al., 2017, Shi, 2017). These endeavors have endowed future researchers with invaluable insights into CFD simulations.

For optimal CFD modelling precision, it is imperative for researchers to root the numerical model in an authentic physical framework. This requires an intimate familiarity with simulation conditions. Additionally, mesh quality, especially in boundary layers, warrants careful consideration given its sensitivity to different turbulence model stipulations. While steady-state flows around the turbine permit a more economical steady-state modelling approach, situations marked by pronounced transient phenomena – such as irregular inflow velocities or significant turbine-induced vortices – necessitate transient analyses. Such endeavors underscore the importance of a profound grasp of EHM's operational dynamics, coupled with adept CFD expertise (Shi, 2017).

2.6 Conclusion

This chapter presented a literature review surveying the current landscape of UGs, OTEC-PCM, and specifically the turbine-based EHMs employed in UGs within this study. The review also touched upon pivotal research methodologies essential for the development of the turbine-based EHM. Several conclusions and existing knowledge gaps, which this research endeavors to bridge, emerged from the review, shaping the trajectory of this thesis:

- The review highlighted the prominence of UGs in ocean exploration, a domain poised to gain increasing significance for the global economy. One prevailing trajectory for UGs advancement centers around augmenting their range and endurance. However, energy constraints currently hamstring UGs progression.

- The literature emphasized that energy harvesting from the oceanic milieu presents a promising avenue to tackle UGs energy challenges. Many scholarly pursuits have delved into the application of OTEC-PCM to UGs, illuminating the feasibility of tapping oceanic thermal energy for its conversion into electrical energy, essential for UGs functionalities. Within this framework, NASA introduced a turbine-based EHM boasting enhanced reliability, diminished energy demands, and enriched operational versatility for UGs. While this paradigm holds potential advantages over its OTEC-PCM counterparts, its energy harvesting turbine demands further innovation and validation.

- The review uncovered two major research gaps: the first is "*extremely limited research about the working mechanism of the turbine in the turbine-based EHM*". The second is "*extremely limited research on the design method suitable for the turbine in the turbine-based EHM*". Addressing these knowledge gaps will enable further exploration of the turbine-based EHM's feasibility and bring it closer to practical application, which is this research's aim. These gaps are summarized in Table 2-2.

- These two main research gaps can be divided into the following components that will be explored in subsequent chapters of this study:

    1. Strategies to decipher the design philosophy inherent to the turbine in EHM;

    2. Unraveling the inherent design philosophy of the turbine in EHM, and discerning if it aligns with conventional turbines;

    3. Exploring avenues to refine the actuator disc theory (momentum theory);

4. In the event of an actuator disc theory enhancement, devising a groundbreaking design methodology predicated on this refined theory;

5. Assessing the energy harvesting prowess of EHM outfitted with a turbine crafted from insights culled from this research.

Table 2-2: Two main research gaps in this study

	Research gaps
1	Limited research about the working mechanism of the turbine in the turbine-based EHM
2	Limited research on the design method suitable for the turbine in the turbine-based EHM

3 Preparatory work before the study of turbine

3.1 Introduction

Chapter 3 serves as foundational groundwork preceding the detailed exploration of the turbine. While the turbine within this EHM stands central to the investigation, it is imperative first to delineate other pertinent elements within NASA's turbine-based EHM. This is especially crucial since NASA's turbine-based EHM currently exists as a conceptual outline, warranting meticulous elaborations in multiple areas. Further, given certain engineering constraints, specific aspects necessitate refinements. Upon finalizing these detailed designs and tweaks, the comprehensive examination of the turbine will commence in Chapter 4. Initially, attention is turned to alterations in NASA's turbine-based EHM. Analyzing the standard design attributes of UG, practical engineering challenges confronting the energy harvesting approach of NASA's turbine-based EHM, as depicted in Figure 2-18, are discerned. To mitigate these issues, this chapter embarks on refining the energy harvesting mode, bolstering the feasibility of EHM. Primary among these changes are the modification of UG operational trajectory and a revision of the initial technique for transmuting thermal to hydraulic energy.

Furthermore, details are provided regarding the overarching design parameters of the turbine-based EHM. These encompass UG's external configuration, the operational depth of the entire assembly, the prevailing water temperature at the designated operation site, and PCM's mass.

Structured within this framework, Section 3.2 delves into the enhancements made to NASA's turbine-based EHM's energy harvesting approach. Section 3.3 sheds light on the parameter choices for the turbine-based EHM as pursued in this study. Conclusively, Section 3.4 offers a summation of the chapter.

3.2 Modifications to the energy harvesting mode of NASA

EHM

This section delves into the engineering challenges associated with NASA's turbine-based EHM's energy harvesting mode, followed by a presentation of two modifications designed to overcome these challenges.

3.2.1 Engineering challenges with the energy harvesting mode of NASA EHM

Figure 2-18 illustrates the conceptual framework of NASA's turbine-based EHM, which envisions outfitting a turbine at the end of UG. This turbine is intended to harness the kinetic energy derived from UG's gliding motion, subsequently converting it into electrical energy to power UG during energy harvesting. Given the prevalent dimensions and design specifics of the system, this operational mode is not devoid of engineering challenges, primarily owing to UG's modest gliding velocity.

The diminished gliding speed is a direct consequence of the design constraints dictated by the standard size and structure of UG. Typically, UG spans a length of about 2 s with a hull diameter close to 0.2 m. Its hull, reminiscent of a torpedo's streamlined design, prioritizes hydrodynamic efficiency. These inherent design elements restrict UG's ability to house a sizable thermal engine. Typically, the thermal engine can encase merely about 10 kg of PCM, culminating in a restrained ballast force（B）. Consequently, UG's cruising velocity is capped at a maximum of 0.5 m/s. The integration of a turbine during the energy harvesting phase further accentuates this speed reduction.

As mentioned above, such nominal velocities signify the turbine blades' sluggish traversal through water, resulting in an abysmally low Re. This situation invariably leads to the formation of a LSB on the foil, a well-documented phenomenon (Munson et al., 1995, Burton et al., 2011, Schlichting et al., 1961). The emergence of an LSB can profoundly disrupt the flow dynamics over turbine blades, ushering in a cascade of turbine operational challenges. Primarily, LSB presence can intensify the pressure drag on blades, attributable to boundary layer thickening and an amplified

pressure gradient. This scenario severely compromises the turbine's efficiency. Furthermore, LSBs can induce flow irregularities, precipitating premature stall. This condition, where the lift coefficient precipitously wanes with an escalating angle of attack, can manifest as unexpected power output downturns, potentially destabilizing consistent power generation. The turbulent activity within the bubble can also trigger vibrations and noise, which, over extended periods, might compromise the turbine's structural integrity (Lissaman, 1983, Marxen et al., 2003). A typical LSB is depicted in Figure 3-1.

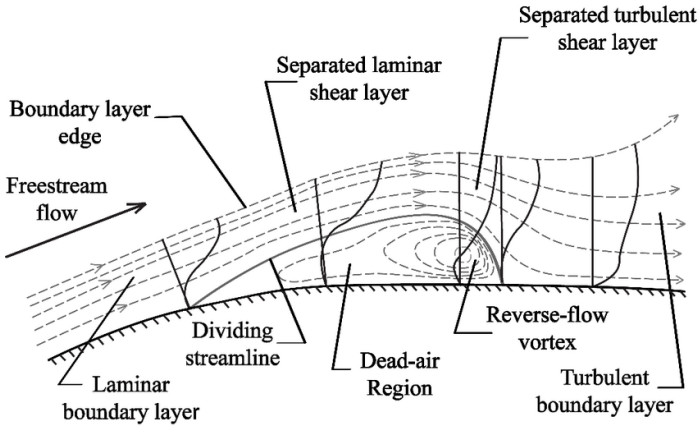

Figure 3-1. Schematic of a laminar separation bubble (Roberts et al., 2017)

Additionally, UG's gliding phase, combined with a spinning turbine at its posterior, could jeopardize its stability, amplifying the risks of wing stall. A wing stall occurrence might incapacitate UG's recovery mechanisms, compelling it to plummet into the ocean's abyss, eventually succumbing to the overpowering effects of profound water pressure. In summary, the energy harvesting mode as proposed by NASA presents formidable challenges, questioning its viability in practical implementations.

To address the engineering challenges, this study suggests two modifications to the energy harvesting mode of NASA's turbine-based EHM. The crux of these modifications lies in amplifying UG's movement velocity by augmenting the force propelling it forward.

3.2.2 First modification to the energy harvesting mode

The primary adjustment involves altering the working trajectory of UG. This change aims to help the turbine counteract the significantly reduced efficiency due to the low Re associated with UGs' slow velocity.

The force analysis of the entire UG in NASA's energy harvesting mode is shown in Figure 3-2. B can be broken down into two components: B_D, which is in line with UG movement, and B_L, which is perpendicular to UG movement. B_D opposes the total system drag in magnitude, while B_L counteracts the lift generated by the wings in magnitude. The system maintains equilibrium in this stable gliding state. It is clear that B_D is the force that propels the system forward and allows the turbine to generate electricity. However, as B_D is just a fraction of B, its magnitude is significantly smaller than B. The relationship between B_D and B is described by Equation 3-1.

$$B_D = B * sin\left(\phi_g\right) \tag{3-1}$$

where ϕ_g is the gliding angle, as shown in Figure 3-2.

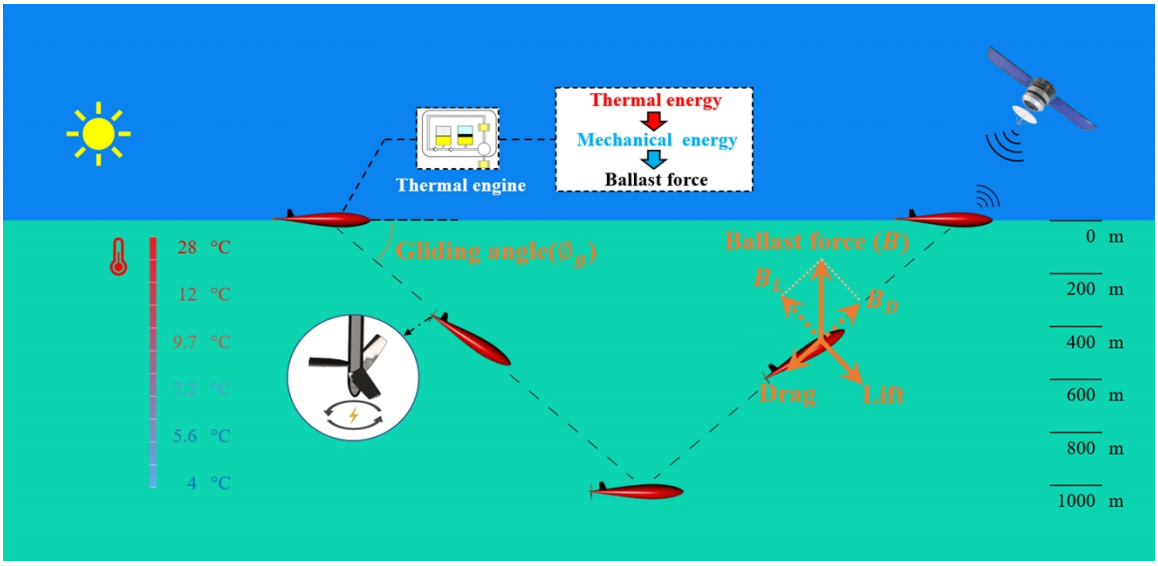

Figure 3-2. Force analysis of UG in NASA's energy harvesting mode

As previously discussed, the pressing need to make this EHM functional is to maximize B_D as much as possible. According to Equation 3-1, with a constant B, the sole method to augment B_D

is to amplify $sin(\phi_g)$. The relationship between the sine function and its angle is illustrated in Figure 3-3, where it peaks at a value of 1 at 90 degrees. Leveraging this property, this study suggests a novel energy harvesting mode where ϕ_g is set to 90 degrees. In this scenario, B_D will be equivalent to B.

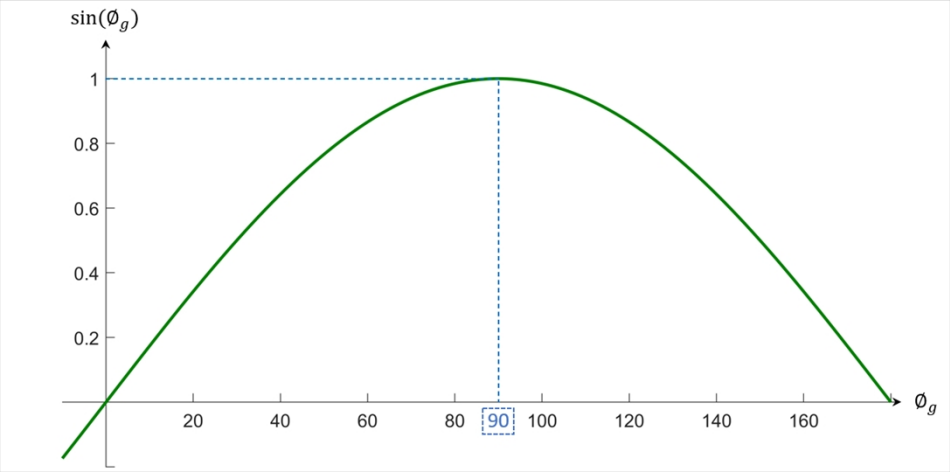

Figure 3-3. Relationship between the sine function and the angle

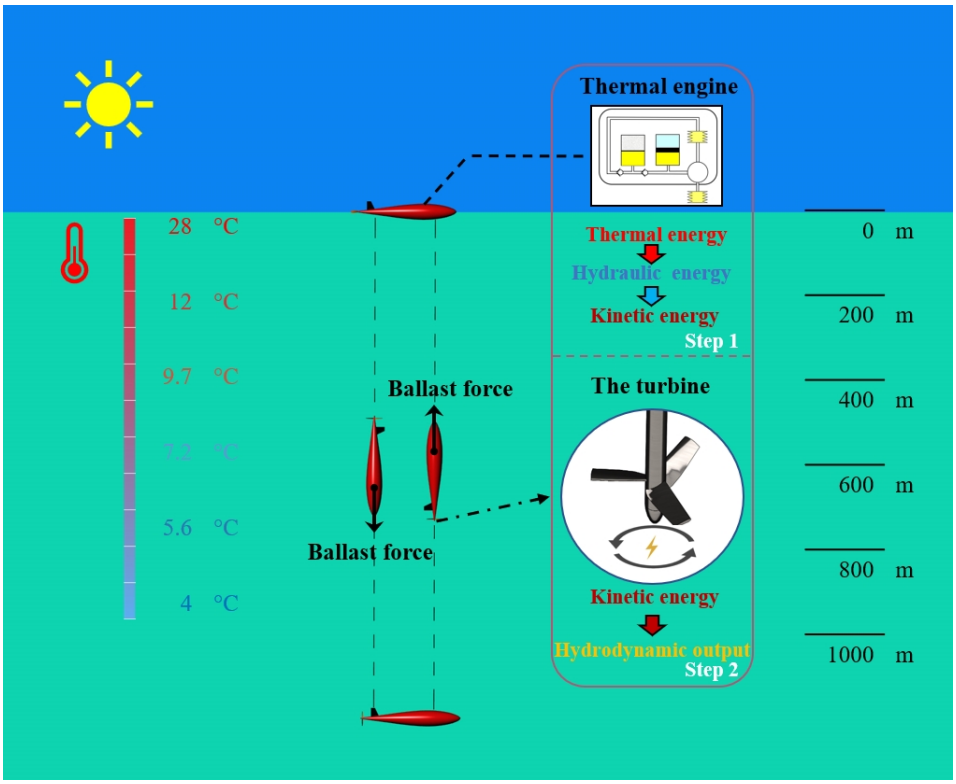

Figure 3-4. Proposed new energy harvest mode for EHM

In the proposed energy harvesting mode, the thermal buoyancy engines will harness thermal energy and produce a ballast force, propelling UG to move vertically in the ocean with the aid of an attitude adjustment unit. During this motion, the turbine at the rear of the hull rotates, driven by the fluid, to capture energy. This process is illustrated in Figure 3-4.

In the vertical motion trajectory adopted for UG, the ballast force is entirely harnessed to drive the system, leading to a marked increase in both the system's movement velocity and *Re* for the turbine blades. This mode of power generation also circumvents the potential wing stall scenario previously discussed in NASA's concept, caused by the turbine's presence.

3.2.3 Second modification to the energy harvesting mode

With UG's new movement trajectory, the ballast force is now fully engaged to power the entire system. It is evident that amplifying the ballast force can grant the system an even higher movement velocity, which further addresses the engineering challenges of the turbine-based EHM.

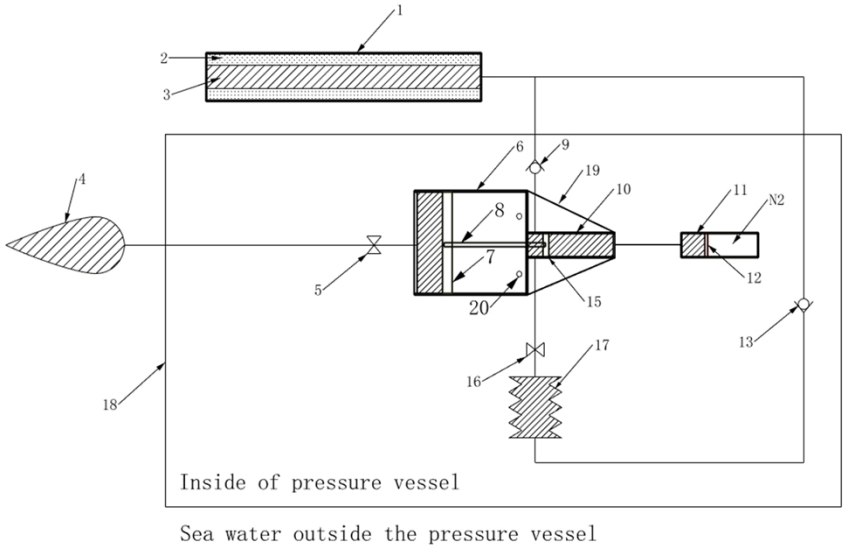

Figure 3-5. 2D concept diagram of the thermal buoyancy engines

Thus, the subsequent modification involves altering the original method used to convert thermal energy into hydraulic energy in order to achieve greater ballast force. In pursuit of this, a new-type

thermal buoyancy engine, offering a higher ballast force, has been introduced (Shi et al., 2022). A diagram of this thermal buoyancy engine is provided in Figure 3-5, and a breakdown of its various components can be found in Table 3-1.

The description of the various parts depicted in the drawings can be found in Table 3-1 as follows:

Table 3-1: Various parts in the thermal buoyancy engines

Part name	Number	Part name	Number
Heat transfer	1	PCM	2
Hydraulic oil	3	Outer oil bladder	4
Magnetic valve	5，16	Single-acting low-pressure cylinder	6
Piston in single-acting low-pressure cylinder	7	Hydraulic rod	8
Check valve	9，13	Double-acting high-pressure cylinder	10
Accumulator	11	Piston in accumulator	12
Piston in double-acting high-pressure cylinder	15	Inner oil bladder	17
Pressure vessel/UG hull	18	Rib	19
Air hole	20		

The underlying principle of the new-type buoyancy engine is to harness the high pressure that PCM can generate to its full potential. As previously mentioned, elevating the working pressure of PCM and integrating a high-low hydraulic pressure conversion mechanism between PCM and the hydraulic circuit emerges as a promising approach to amplify the efficiency and ballast force of the thermal engine (Falcão et al., 2016). To this end, the thermal buoyancy engines depicted in Figure 3-5 incorporates such a hydraulic pressure conversion mechanism. This conversion mechanism is composed of a high-pressure double-acting cylinder with a smaller cross-sectional area (10), a low-pressure single-acting cylinder with a larger cross-sectional area (6), and a hydraulic rod (8) that links the pistons in these two cylinders. When high-pressure oil is introduced into the high-pressure double-acting cylinder (10), the piston inside, designated as (15), is impelled to move. Due to the connection via the hydraulic rod (8), the piston in the low-pressure single-acting cylinder (7) moves

synchronously. During this action, the high pressure within the double-acting cylinder is converted to low pressure. When the accumulator discharges an equivalent amount of mechanical energy, a reduced oil pressure correspondingly signifies a larger oil volume, which subsequently implies a more pronounced ballast force.

Control method and principle of the new-type thermal buoyancy engines

Given the modifications made to the thermal buoyancy engines' design, its control method warrants reconfiguration as well. From a control standpoint, the entire operation cycle of the updated thermal buoyancy engines can be segregated into six distinct phases, as illustrated in Figure 3-6.

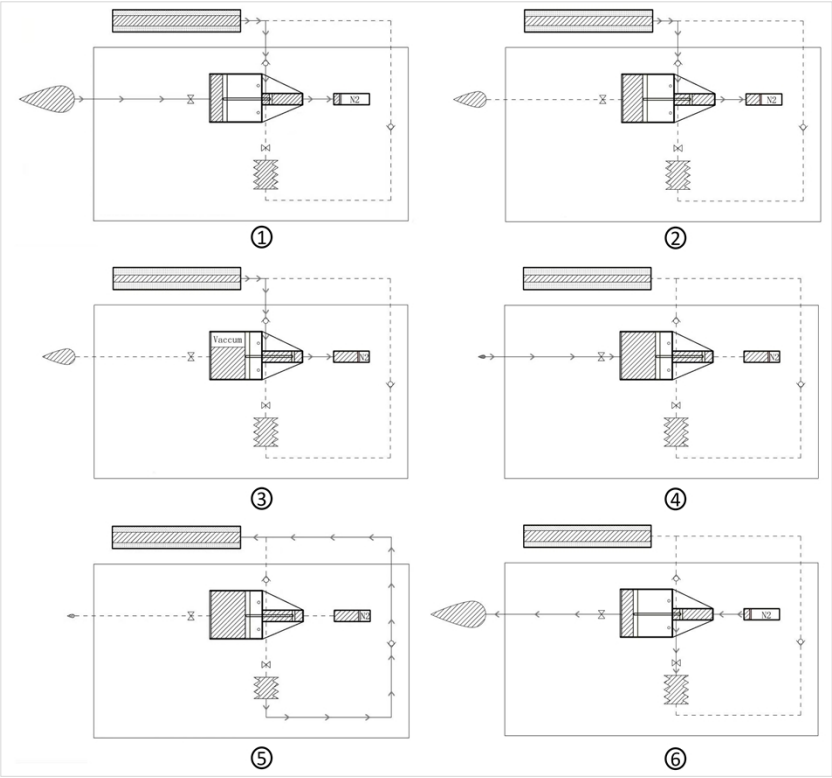

Figure 3-6. 6 steps of the thermal buoyancy engines in one cycle

In the first step, the engine is on the ocean's surface. PCM 2 melts, driving the hydraulic oil 3 out from the heat transfer 1. Both magnetic valves 5 and 14 are opened, while magnetic valve 16 remains closed. The hydraulic oil 3 propels piston 15 to move to the right, pushing the oil on the right side of piston 15 into the accumulator 11. Since piston 15 is linked with piston 7 via rod 8,

piston 7 also moves similarly. The atmospheric pressure forces the oil from the outer oil bladder 4 into the cylinder 6. In the second step, as PCM 2 is nearly half melted, the buoyancy slightly surpasses gravity. Magnetic valve 5 closes while magnetic valve 16 stays closed, stabilizing the buoyancy. The system remains on the warm sea surface. In the third step, as PCM 2 continues to melt, pistons 15 and 7 are driven forward, creating a vacuum in cylinder 6 due to the sealed piston 7. During the fourth step, once PCM 2 is fully melted, magnetic valves 14 and 16 are closed while magnetic valve 5 opens. This action allows the oil in the outer oil bladder 4 to move into cylinder 6. With the buoyancy now lesser than gravity, the thermal buoyancy engines begin their descent. In the fifth step, as the new thermal engine descends, the water temperature drops significantly. The solidifying and contracting PCM 2 prompts the oil in the inner oil bladder 17 to be directed into the transfer 1, assisted by the air pressure in the watertight shell 18. In the sixth step, the thermal buoyancy engines reach a predetermined depth (around 1000 m). All three magnetic valves – 5, 14, and 16 – open simultaneously. The accumulator 11's hydraulic oil gets directed into cylinder 10, pushing piston 15 in cylinder 10 to the left. Since pistons 15 and 7 are connected by hydraulic rod 8, piston 7 also shifts left. This movement forces the oil in cylinder 6 into the outer oil bladder 4 and pushes the oil on the left side of piston 15 in cylinder 10 into the inner oil bladder 17. With buoyancy now greater than gravity, the thermal engine commences its ascent. Upon reaching the sea surface, PCM 2 resumes melting, initiating the next cycle.

As elaborated in Section 2.3.2, the constrained ballast force of the thermal buoyancy engines result from the inefficient utilization of PCM, stemming from two primary factors. The first pertains to the non-ideal working pressure of PCM when converting thermal to mechanical energy. The second is the porosity phenomenon observed in PCM, which results from the restricted air pressure within the pressure vessel, bound by the external atmospheric pressure. The new-type thermal buoyancy engines address both these issues to enhance ballast force. Firstly, the new engine can elevate the working pressure of PCM to its thermodynamically optimal level. It then transfers this high pressure to UG's inherently low working pressure, surmounting the initial hurdle to achieve enhanced ballast force. Furthermore, the new-type thermal buoyancy engines are designed to

sustain high air pressure within UG hull, addressing the second impediment for increased ballast force. As highlighted in Section 2.3.2, in conventional thermal buoyancy engines, oil from the external oil bladder is drawn into the internal bladder, driven by the pressure differential between the atmospheric pressure and the internal air pressure. This necessitates the internal pressure to be maintained below the atmospheric pressure. However, since this internal air pressure also assists in channeling the oil back to the heat transfer, its reduced value leads to the porosity issue in PCM, culminating in suboptimal PCM efficiency. A prevailing approach to this challenge has been to embed a supercharging device within UG hull, tasked with guiding the oil from the internal bladder back to the heat transfer mechanism (Yang et al., 2016). Nevertheless, introducing such a device not only escalates energy consumption but also potentially compromises the entire system's reliability. In stark contrast, the new-type thermal buoyancy engines intake oil from the external bladder into the hull directly under the elevated pressure generated by PCM. This design bypasses the need to maintain the internal air pressure beneath the atmospheric threshold, thus permitting an augmented internal pressure. This alleviates the pronounced porosity issue, negating the requirement for any supplementary supercharging device.

3.3 Design parameters for the following study

In the following sections, different case studies will be presented. For consistency, the design parameters of UGs in each case study will be uniformly detailed, including aspects like UGs' working water depth, water temperature, PCM weight and volume, and glider dimensions.

In these cases, UGs' operational depth (d_w) is set at 1,000 m, which is acknowledged as a standard working depth for UGs. This depth was selected precisely because it represents the typical operational range, ensuring that the choice for EH mode is realistic and does not necessitate any alterations to the standard UGs specifications. The water temperature at the sea's surface (T_h) registers at 28 ℃, while the temperature at the operational depth (T_l) stands at 4 ℃. This temperature remains consistent at such depths owing to the ocean's thermocline (Kong et al., 2010).

At the specified depth (d_w), UGs operate under a pressure of about 10 MPa, corresponding to the hydrostatic pressure of seawater at 1,000 m.

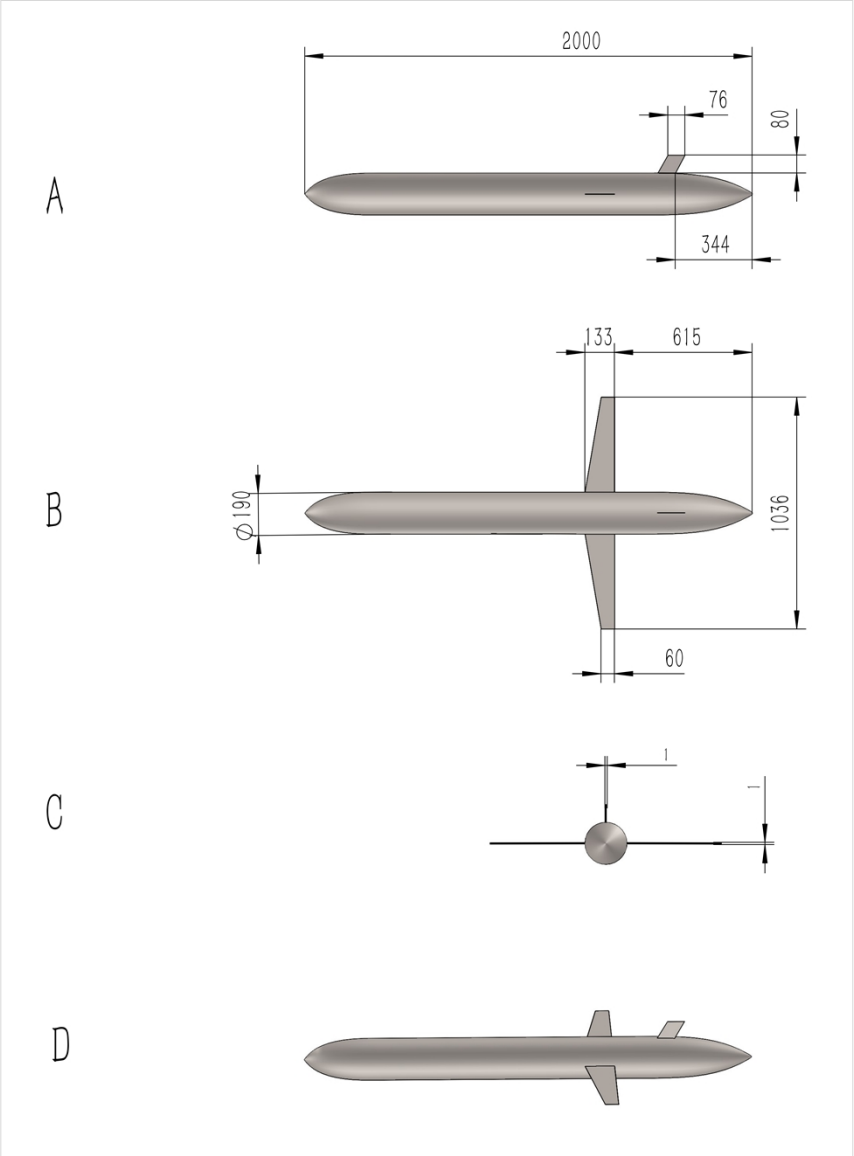

Figure 3-7. Size and configuration of proposed UG: (a) Side profile; (b) Top profile; (c) Rear profile; and (d) Perspective profile

As shown in Figure 3-7, UG in this study are designed with a torpedo-shaped hull. The hull length (L_h) measures 2 m, while its diameter (D) is 0.19 m. Such a torpedo-shaped design is prevalent among UGs. Examples of this configuration include Slocum by Teledyne Marine (Jones, 2012), the Spray by Woods Hole Oceanographic Institution (Sherman et al., 2001), and Petrel by Tianjin

University (Xue et al., 2018). It is also important to mention that in Chapter 5, due to purely theoretical calculations and the non-dimensionalization of the diameter in the primary conclusion, a new hull is used with a diameter of 0.2 m, which will be introduced specially in the Chapter 5.

In the case studies, n-Pentadecane is chosen as PCM for the thermal buoyancy engines. This PCM is frequently utilized in thermal buoyancy engines due to its efficacy (Yang et al., 2016). It operates effectively within the selected temperature range of 4 ℃ to 28 ℃ (Ma et al., 2016). The volume of PCM (V_{PCM}) in its solid phase is 12 L, approximately weighing 9.7 kg, which aligns with the payload capacity of existing UGs (Falcão et al., 2018).

The design parameters for the subsequent study are summarized in Table 3-2.

Table 3-2: Design parameters of the system for subsequent analysis

Length of UG hull	2 m
Diameter of UG hull	0.19 m
Working depth	1000 m
Working pressure	10 MPa
Water temperature	28 ℃ (sea surface)
	4 ℃ (working depth)
PCM choice	n-Pentadecane
PCM volume	12 L
PCM weight	9.7 kg

3.4 Summary

This chapter outlines the preliminary work conducted prior to studying the turbine. The energy harvesting mode proposed by NASA underwent modifications to address certain engineering challenges, including adjustments to the mov ing trajectory and the method of converting thermal energy to mechanical energy. Furthermore, this work specifies the design parameters of EHM,

encompassing aspects such as hull size, operational depth, temperature, PCM type, and others. Subsequent turbine studies will build upon the modified NASA's turbine-based EHM, incorporating the newly proposed energy harvesting mode and the outlined design parameters.

4 Design of the turbine in the turbine-based EHM

4.1 Introduction

Chapter 3 outlined the components of the turbine-based EHM for this research, laying the groundwork for subsequent chapters centered on the turbine. In this chapter, the thesis embarks on an in-depth study of the turbine within the context of this turbine-based EHM.

To design a turbine that optimizes energy output, the chapter focuses on formulating the design philosophy of the turbine within this EHM by constructing a mathematical model rooted in BEMT. Through this model, a multitude of turbines are designed and analyzed, highlighting the unique operational principles of such turbines and the influence of various design parameters on their energy harvesting capabilities. Moreover, to ensure BEMT-based design methodology aligns with the specific operating conditions of the turbine, as discussed in Section 2.4.3.1, necessary corrections have been made to BEMT-based design method to adhere to traditional BEMT assumptions. This chapter also offers a preliminary validation of the effectiveness of EHM through the mathematical model.

In terms of structure, Section 4.2 elucidates the approach to designing and optimizing the turbine. Section 4.3 delves into analyzing the results derived from the mathematical model. Finally, Section 4.4 encapsulates the key conclusions drawn from this chapter.

4.2 Design and optimization of the turbine

To design and optimize turbine geometry that maximizes energy yield, this chapter establishes a mathematical model rooted in BEMT. This model also provides a preliminary estimation of the system's energy harvesting capacity. Before delving into the mathematical model computations, adjustments are made to the traditional BEMT method. These adjustments are to account for the wake of the glider as an inflow condition and to include the effects of Re on the turbine.

4.2.1 BEMT with velocity corrections in this study

Section 4.2.1.1 validate the effectiveness of BEMT. Subsequently, in section 4.2.1.2, velocity corrections are applied to BEMT. The following steps will involve integrating the velocity distribution corresponding to the hull shape, as introduced in Chapter 3, into BEMT.

4.2.1.1 BEMT model validated versus experimental literature data

Firstly, this research presents a validation of BEM model as mentioned in Section 2.5.1.1, using experimental data available in the literature. Specifically, experimental data from (Shi et al., 2019) is taken into consideration. This data shows C_p and C_t curves of a pitch-adjustable tidal turbine with a radius of $R = 0.2m$. The blade section consists of an S814 section profile. The turbine's geometry is shown in Figure 4-1, while the chord length and twist angle of cross-sectional sections of the blades, located at r^e / R, can be found in Table 1.

The experiment maintained a relatively constant Re number, ranging from 142,000 to 170,000). The test was conducted in the towing tank of Kelvin Hydrodynamic Lab (KHL). Further details of the test and facility are available in (Shi et al., 2019). The uncertainty level of the experiment was as follows: 0.3% for TSR, 1.1% for C_p and 0.2% for $C_t/10$. These values were statistically computed from 7 individual tests at TSR = 4 (Shi et al., 2019).

Figure 4-1. Turbine in the experiment (Shi et al., 2019)

Table 4-1: Detailed geometry of the turbine in experiment

r^e / R	0.2	0.3	0.4	0.5	0.6	0.7	0.8	0.9	1
Chord length (mm)	64.4	60.1	55.8	51.5	47.2	42.9	38.6	34.3	30
Twist angle (deg)	27	15	7.5	4	2	0.5	-0.4	-1.3	-2

The details of the turbine and of the experimental conditions were incorporated into the hydrodynamic BEMT code. As a result, Re used in the simulation mirrors that of the experiment. The hydrodynamic performance of the turbine was then analyzed across various TSRs. Figures 4-2 and 4-3 illustrate the comparison between experimental results and BEMT simulation. A generally satisfactory agreement, with differences typically under 5%, was observed. However, notable discrepancies arose in the low TSR region where the turbine experiences stall. This is attributed to BEMT code, based on Xfoil simulation, not accurately predicting stall. Nevertheless, since the primary focus of the subsequent research is on maximum efficiency, BEMT demonstrates high accuracy in forecasting turbine performance.

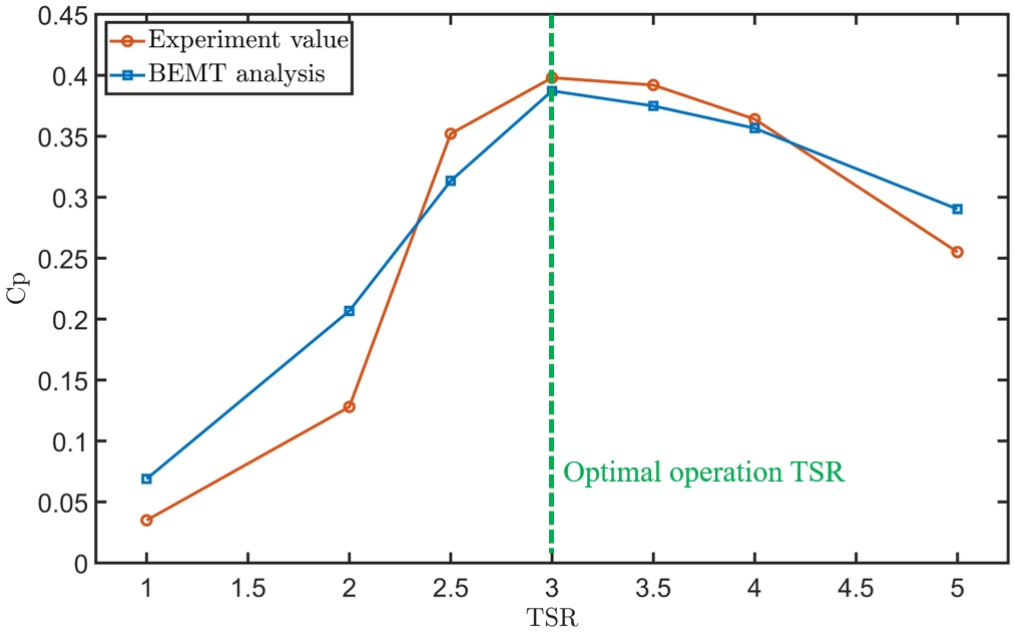

Figure 4-2. C_p of the experimental value and BEMT analysis

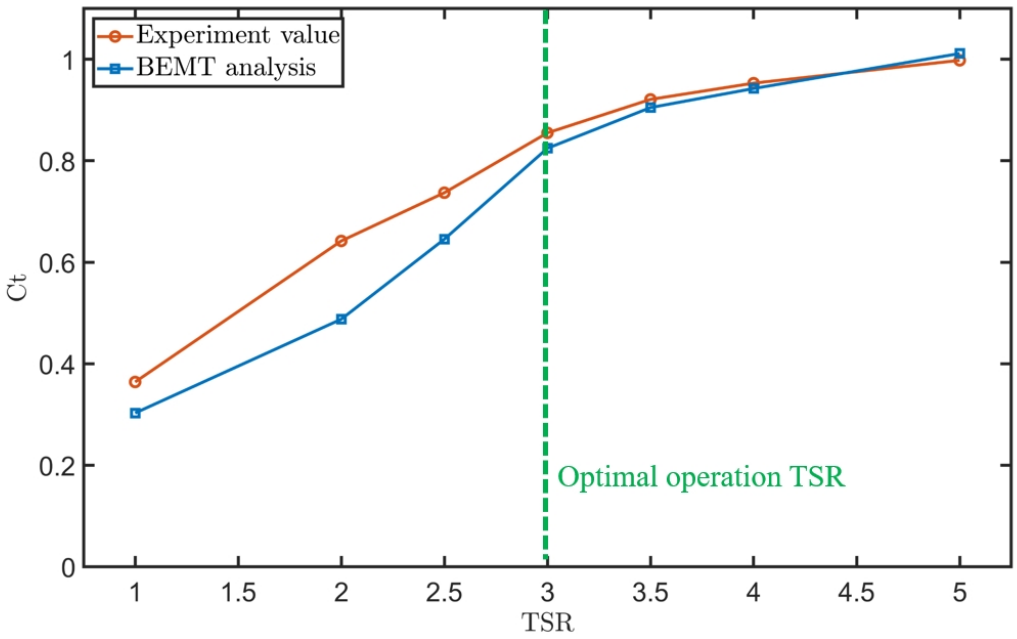

Figure 4-3. C_t of the experimental value and BEMT analysis *BEMT with velocity corrections*

Unlike conventional applications of BEMT, which operate under uniform free stream conditions, the turbine in this study exhibits two distinct characteristics. Firstly, all blade elements operate within a pronounced wake behind the hull. Secondly, the blade elements sometimes function at a low Re range, falling below 50,000 in certain instances. These unique conditions significantly influence turbine design. To account for these specialized working conditions, BEMT is adjusted for both wake and Re. While these corrections modify the outcomes of the traditional BEMT model, its foundational principles remain intact. The modified results should still provide an accurate physical representation of a turbine functioning in the wake of a glider. Given that both wake and Re are tied to velocity, these combined modifications are termed velocity corrections.

Corrections for wake behind the hull

In Section 2.4.3.1, it is noted that traditional BEMT presumes a uniform incoming flow velocity. However, in this study, the incoming flow arises from the wake of UG hull, leading to non-uniform velocity. Such non-uniformity challenges the assumptions of the traditional BEMT, resulting in potential inaccuracies. For instance, under non-uniform inflow, the design angle of attack (α) of

the blade element, corresponding to the foil's optimal hydrodynamic performance, varies. This variation is unaccounted for in the conventional BEMT model.

To address non-uniform inflow and enhance BEMT model, this research introduces modifications based on the wake distribution associated with UG hull, as detailed in Chapter 3. This refined approach can be viewed as a BEMT enhancement influenced by the hull's configuration. CFD simulations are executed using the commercial software STAR-CCM+, facilitating an exploration of wake characteristics near the hull shown in Figure 3-7.

Considering the balance of the thesis structure, the detailed specifics of CFD simulation setup have been placed in Appendix A, including the computational domain, boundary conditions, grid structure, solution methodology, and grid independence verification.

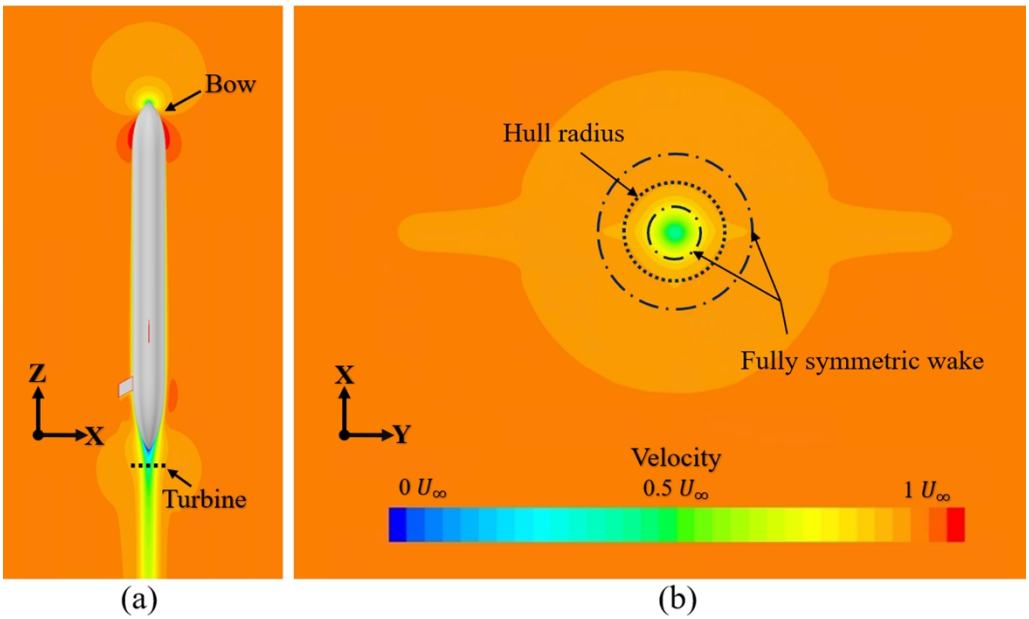

Figure 4-4. Typical wake distribution behind UG

Results can be observed in Figure 4-4(a). Given that the thermal engine can be designed as an interlayer-type to prevent alterations to UG's shape (Zhang et al., 2009b), CFD simulation does not account for any geometric impact of the thermal engine. The wake distribution, situated at 5% of the hull length (L_h) downstream from UG, is depicted in Figure 4-4. Figure 4-4(a) displays the zx-

plane, providing a top view of the glider, while Figure 4-4(b) represents the yz-plane, illustrating the glider's rear view.

As depicted in Figure 4-4(b), the wake exhibits approximate axial symmetry. This pattern emerges because UG's wings minimally impact the wake. Consequently, this study adopts an assumption of symmetric wake, delineated by the dot-dash lines in Figure 4-4(b). Interactions between the hull and the turbine that might modify the wake distribution are not considered in this research. Under these presumptions, the inflow velocity distribution preceding the turbine is demonstrated in Figure 4-5(a). Velocities for a blade segment, situated in plane A-A and referenced to the turbine, are displayed in Figure 4-5(b). It should be noted that plane A-A is also marked in Figure 4-5(a).

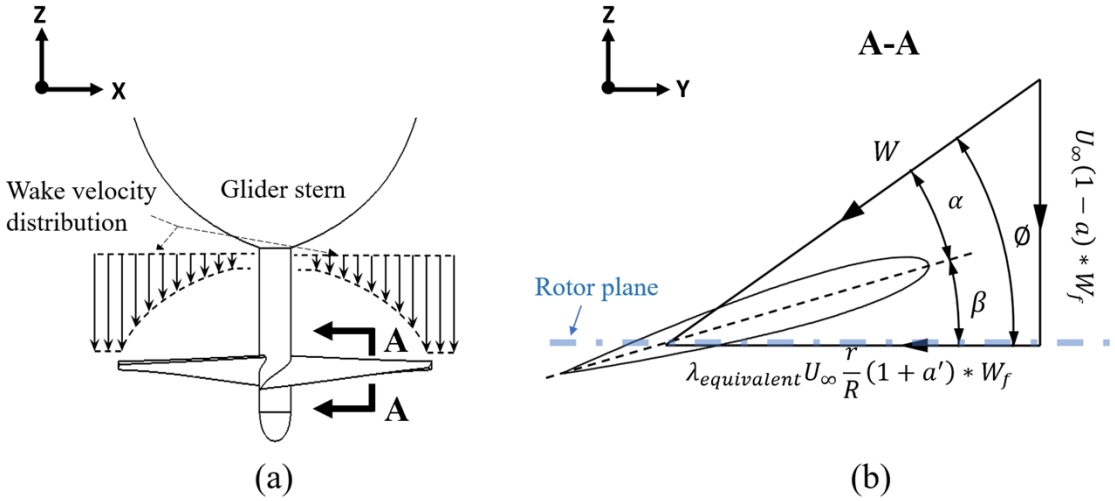

Figure 4-5. Velocities relating to the turbine blade in wake: (a) Side view; and (b) Foil section view

In Figure 4-5(b), W_f is the wake factor expressed through Equation 4-1 as follows:

$$W_f = \frac{V_{wake}}{U_\infty} \tag{4-1}$$

where U_∞ is the incoming velocity and V_{wake} is the flow velocity in the wake.

Subsequently, $\lambda_{equivalent}$ in Figure 4-5(b) can be expressed through Equation 4-2 as follows:

$$\lambda_{equivalent} = \frac{\lambda}{W_f} \tag{4-2}$$

Comparing Figures 4-5(b) and 2-33, the blade elements situated behind the wake operate at $\lambda_{equivalent}$. Therefore, in BEMT design process, shown from Equations 2-2 to 2-5, λ_{design} is converted to $\lambda_{equivalent}$ with Equation 4-2. This modification facilitates the recalculation of the twist angle and chord length for the turbine situated behind the glider. In BEMT analysis in Section 2.5.1.1, $\lambda_{operating}$ is also substituted with $\lambda_{equivalent}$ based on Equation 4-2. Hence, the values for ϕ, α, a, and a' can be recalculated. Subsequently, W in the wake is computed to determine the real power and thrust of the turbine.

By implementing this correction, the influence of wake on the pre-assumptions of traditional BEMT can be negated, allowing BEMT functions properly under the special operating conditions of this research.

Correction for low Reynolds number

This section involves corrections related to the low Re conditions of the system delineated in Chapter 3. In traditional BEMT design and analysis, the lift coefficient (C_L) and drag coefficient (C_D) curves overlook the effects of a fluctuating Re on turbine hydrodynamic performance. Given the system's low movement speed and the influence of the wake, turbine blades occasionally operate at a low Re ($Re < 50{,}000$). Within this range, the hydrodynamic performance of the blade element is compromised and becomes more sensitive to variations in Re (Deters et al., 2014, Li, 2013). The impact of Re on C_L / C_D ratio as a function of attack angle (α) for a NACA 0015 is illustrated through a 2D contour plot presented in Figure 4-6. In the figure, α spans from 0° to 17° on the vertical axis, while Re varies between 10,000 and 170,000 on the horizontal axis. C_L and C_D functions for this research are determined by calculating and interpolating the hydrodynamic performance of NACA 0015 under varying Re and a using the software Xfoil. Figure 4-6 reveals a decline in C_L / C_D ratio as Re diminishes. This characteristic complicates turbine design. Since the turbine's geometry and Re are both pivotal and uncertain factors in the design process, any

significant deviation between the design Re of the foil and the actual operational Re can affect turbine performance. In such instances, the momentum captured by the turbine deviates from the optimal momentum anticipated by BEMT.

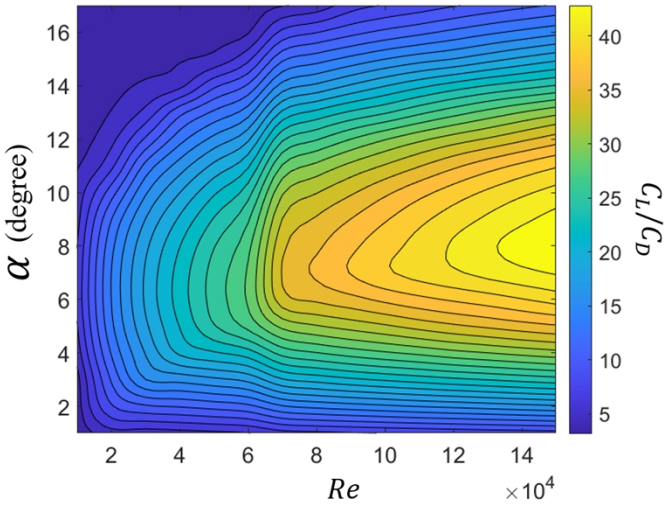

Figure 4-6. Lift-to-drag ratio of NACA 0015

In turbine analysis, as Re differs for each blade element, Re for each one is calculated based on its local velocity. Hydrodynamic data for each blade is then acquired corresponding to its specific Re value. This information is employed to determine the load each blade element experiences. The cumulative loads across all blade elements are integrated to deduce the turbine's comprehensive performance.

For turbine design, this research employs an iterative method to ascertain Re and the definitive blade geometry of the turbine using BEMT. The design methodology is depicted in Figure 4-8. At the commencement of this process, a, R, λ_{design}, and W_f serve as inputs to BEMT model with velocity adjustments. Subsequently, $\lambda_{equivalent}$ is determined using Equation 4-2. This $\lambda_{equivalent}$ supersedes λ_{design} in conventional BEMT for the calculation of a' and the chord length (C). Post computing a', the inflow angle (ϕ) and the twist angle (β) are derived from Equation 2-3 and 2-4, respectively. The relative velocity W, as illustrated in Figure 4-5(b), is then computed. The subsequent stage involves inputting C_L and C_D functions in terms of Re. An initial Re, preset to

100,000, is employed to initiate the iteration. C_L and C_D values are re-evaluated according to the Re derived from this iterative process. Utilizing C_L and C_D, the chord length is determined via Equation 2-5. With the chord length established within this loop, a fresh Re can be computed. This iterative sequence persists until Re residual falls below 1,000, a threshold which induces only negligible hydrodynamic alterations in the foil, even at exceedingly low Re values.

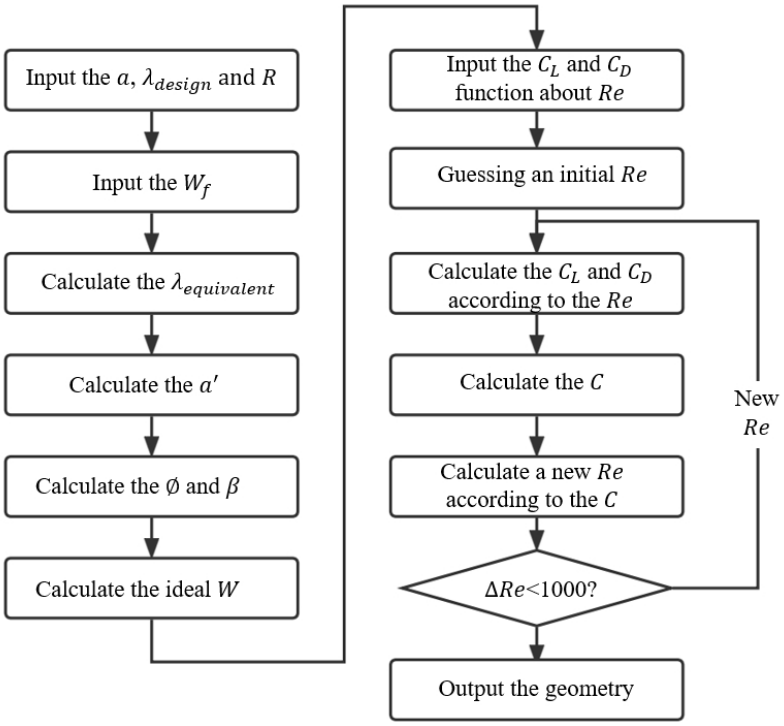

Figure 4-7. Modified turbine design process based on BEMT

Benchmarking BEMT with velocity corrections

This section compares BEMT model with and without velocity corrections. Each turbine blade is divided into 17 blade elements. Hydrodynamic parameters for each blade element, including C_L and C_D, are separately calculated based on local velocities. Loads including thrust and torque, on each blade element are determined through iteration, setting a convergence criterion at a residual value below 0.01.

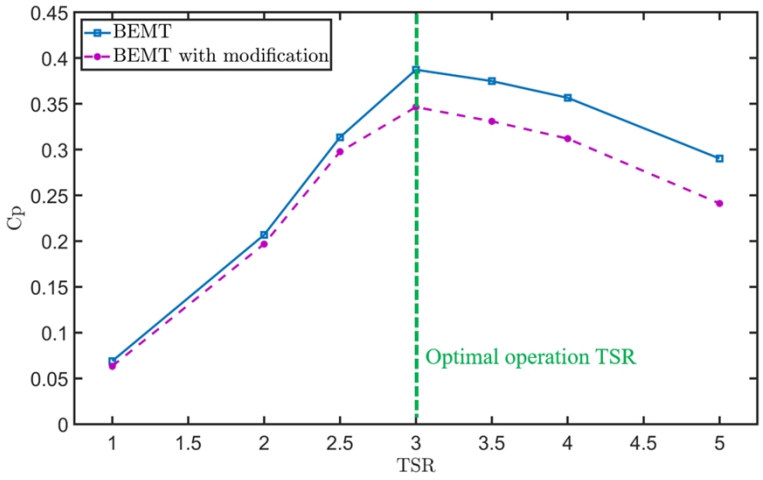

Figure 4-8. C_p in BEMT with and without velocity corrections

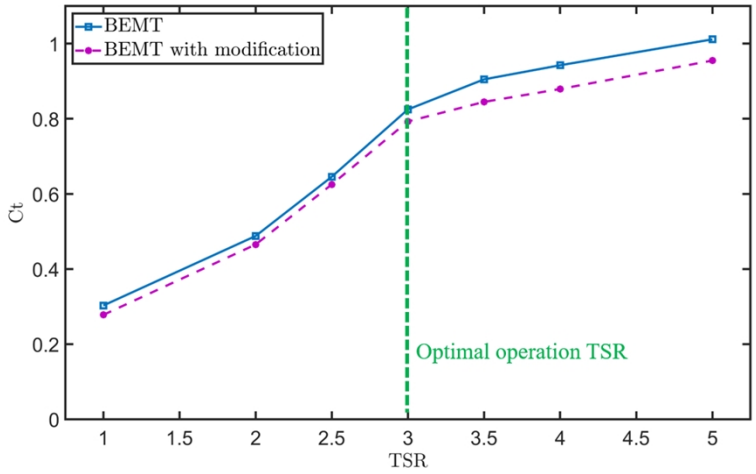

Figure 4-9. C_t in BEMT with and without velocity corrections

BEMT model with velocity correction analyses the turbine when it operates behind the wake of a hull. Consequently, the turbine experiences a nonuniform inflow and a low Re near the hub caused by the concave shape of the wake (Figure 4-4(a)). The results of the comparison are shown in Figure 4-8 and Figure 4-9. Observations indicate that both C_p and C_t decrease, approximately by margins of 16.5% and 7%, respectively.

The decline in C_p qualitatively similar to the results of a wind turbine located in the second row of a wind farm array (Barthelmie et al., 2009). This provides confidence that BEMT model,

integrated with velocity corrections, shows physically accurate data. It accounts for the effects of a turbine operating behind a blockage, in this case, UG hull.

The reduction in turbine performance, as portrayed in BEMT model with velocity corrections, is caused by three main reasons. Firstly, there is a deficit in wake energy. Secondly, Re number behind the wake is lower compared to Re number in open water. Lastly, there is a difference between the turbine design conditions (open water) and working conditions (wake), which corrects the blade elements' angle of attack. To quantify the first effect, the energy deficit E_d, this study divides the area within the radius of the turbine into 500 rings of equal-width but varying radii. The energy within each ring is then computed and added. Therefore, the energy deficit can be defined with Equation 4-3 as follows:

$$E_d = 1 - \frac{\sum_{i=1}^{500} \frac{1}{2}\rho(U_\infty * W_{fi})^3 2\pi r_i^e * \Delta r^e}{\frac{1}{2}\rho U_\infty^3 \pi R^2} \tag{4-3}$$

where W_{f_i} is the wake factor of the i th ring; r_i^e is the radius of the i th ring; and Δr^e is the width of each ring (R / 500).

Behind the hull, E_d is approximately 13%, which is similar to the estimated power drop of Figure 4-8 (approximately 16.5%). Therefore, the drop of C_p is mainly due to the reduced energy available in the wake. While the diminished Re caused by wake and the suboptimal angle of attack for some blade elements can impact the hydrodynamic performance of the turbine, their effect appears to be less significant.

4.2.2 Design considerations of UG

This section presents the design considerations for UG as the preconditions for the mathematical model used to design the geometry of the turbine for optimum energy extraction. The detailed flowchart of the mathematical model is introduced in the following section. Prior to introducing this flowchart, the study will detail four steps that form a crucial part of UG's design considerations.

Step 1： Input the working environment of UG (Section 3.3): The working depth of UG (d_w) is 1000 m; the water temperature at the surface (T_h) is 28 $°C$; and the water temperature at working depth (T_l) is 4 $°C$. At d_w , the working pressure of UG ($P_{working}$) is approximately 10 MPa.

Step 2: Input the information about UG hull (Section 3.3): The wake distribution and the resistance of the hull from CFD STAR CCM+ simulation is added into the mathematical model in function form. The radial wake distribution, located at 0.05 L_h downstream of UG, is expressed by the wake factor (W_f) in Equation 4-4.

$$W_f = -22071\mathrm{r}^5 + 11427\mathrm{r}^4 - 1851.5\mathrm{r}^3 + 56.632\mathrm{r}^2 + 9.8071\mathrm{r} + 0.3626 \tag{4-4}$$

Since the wake distribution varies limited with cruising speed, it is considered to be independent of the cruising speed and is only dependent on the radial coordinate r . The relationship between hull resistance (R_h) and cruising velocity V can be expressed with Equation 4-5.

$$R_h = 2.0681V^2 + 1.2188V - 0.279 \tag{4-5}$$

Step 3: Input the information about the thermal buoyancy engines: There are two assumptions about the thermal engine in the mathematical model: (a) The hydraulic components are considered ideal; (b) The temperature of N_2 in the accumulator is considered constant. PCM used in the engine for this case is n-Pentadecane. Its PVT relationships, which relate the pressure (*P*), volume (*V*), and temperature (*T*) of PCM, are expressed using Equation 4-6 and Equation 4-7 (Falcão et al., 2016):

$$V_{PCM_S} = 1.198 - \left(\frac{1}{55}\right)\left(P_{PCM} * 0.0143 - 0.0408 * \left(T_{PCM} + 5.5\right)\right) \tag{4-6}$$

$$V_{PCM_L} = 1.3195 - \left(\frac{1}{300}\right)\left(P_{PCM} * 0.1817 - 0.2733 * \left(T_{PCM} - 30\right)\right) \tag{4-7}$$

where V_{PCM_S} and V_{PCM_L} are the volume of PCM in solid and liquid phases, respectively.

Equation 4-6 and 4-7 are derived from Falcão, in which a new quasi-static model for a thermally driven volumetric pump used in UG is proposed by (Falcão et al., 2016). This PVT relationship is partly based on empirical values and is also designed to be in accordance with Maxwell relations.

Although it is not directly derived from experimental data, it is considered to introduce minimal error.

As mentioned in Section 3.3, the volume of PCM (V_{pcm}) is set as 12 L (about 9.7 kg) in solid phase which is compatible with the payload capacity of existing UGs. The pressure in the hull (P_{inner}) is set at 0.1 MPa. The maximum gas pressure in the accumulator ($P_{\max}$), when all PCM has melted, is at 90 MPa. Here, Pentadecane obtains its highest thermodynamic efficiency (Falcão et al., 2016). Pre-charge pressure (P_P) in the accumulator is 85 MPa. The maximum gas volume in the accumulator is 10 L. The buoyancy magnification (M_b) is 8.5.

Step 4：Calculate the ballast force (B) that the thermal buoyancy engines generate: Firstly, T_h and $P_{\max}$ are substituted into Equation 4-7 to calculate the unit volume of PCM in liquid phase (V_{PCM_L}). Subsequently, T_l and P_{inner} are input into Equation 4-6 to calculate the unit volume of PCM in solid phase (V_{PCM_S}). Finally, Equation 4-8 is used to calculate B, in this case, is 25 N.

$$B = \frac{V_{PCM_L} - V_{PCM_S}}{V_{PCM_S}} * V_{pcm} * \frac{M_b}{2} \tag{4-8}$$

This force is significantly greater than typical ballast forces obtained with conventional thermal engines using the same amount of PCM.

4.2.3 Construction of the mathematical model

Having established the design considerations for UG, the subsequent step is to develop the mathematical model to design the turbine for optimal energy extraction. This mathematical model is crafted to optimize λ_{design} and radius (R) based on BEMT with the velocity corrections outlined in Section 4.1. The model's procedure is depicted in Figure 4-10.

The flowchart illustrates that the mathematical model comprises three loops. The central, or innermost loop, encompasses Steps 5 through 9. Instead of describing the flowchart from top to bottom, this analysis begins with the inner (core) loop and then progresses outward. This approach

helps elucidate how the more complex components of the model relate to the broader considerations.

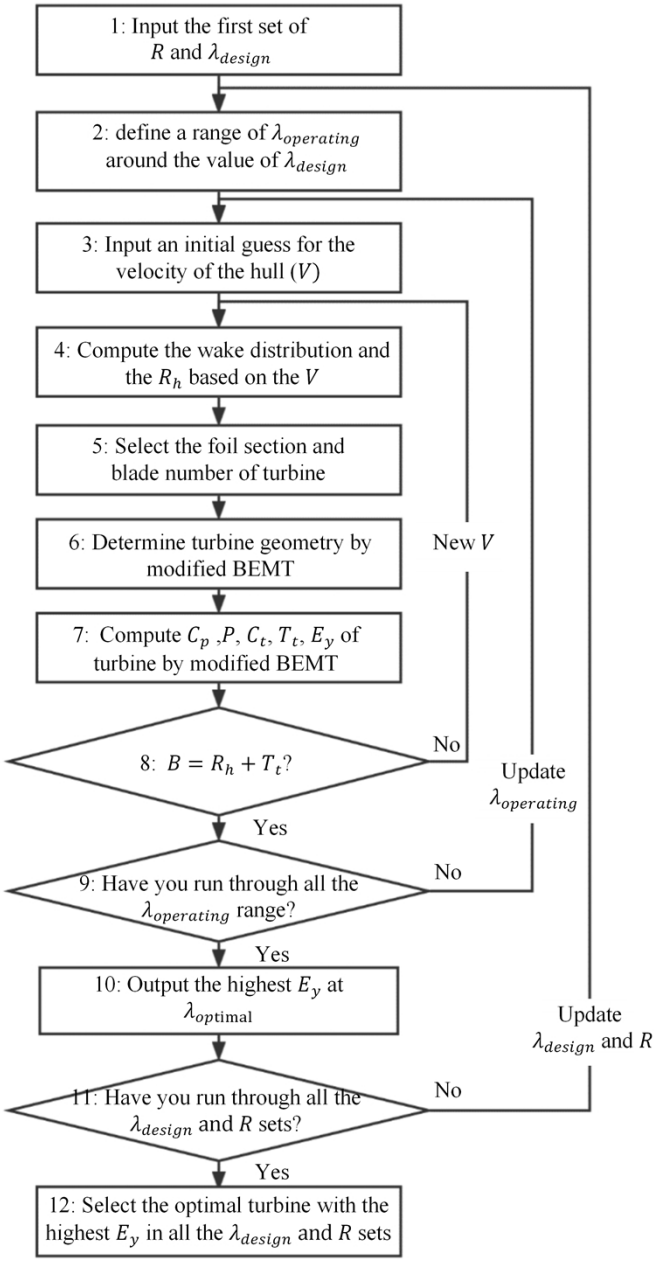

Figure 4-10. Second part of the mathematical model

The core of the model consists of Steps 4 through 8. Given a specific λ_{design}, design radius (R), operating TSR ($\lambda_{operating}$), and UG's moving velocity (V), this section autonomously designs and

analyzes a turbine using BEMT model with velocity corrections. The following details Steps 4 to 8:

Step 4: Upon receiving UG's moving velocity (V), Step 4 calculates the wake distribution and hull resistance (R_h) based on V using Equations 4-4 and 4-5.

Step 5: In this case, a NACA0015 foil section is selected, as shown in Figure 4-11. C_L and C_D of this foil at different Re and α are input into the mathematical model in function form. The turbine has 3 blades.

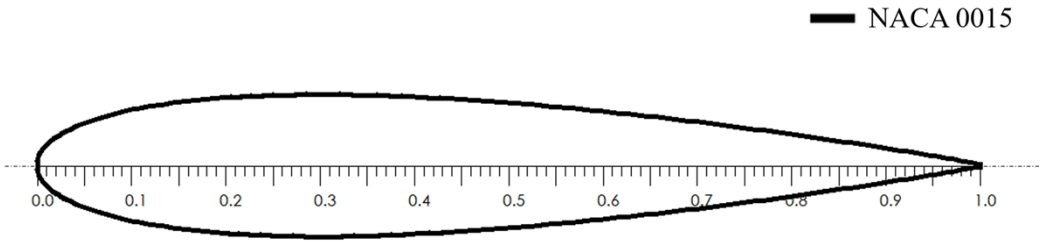

Figure 4-11. NACA0015 foil section

Step 6: This step determines the turbine geometry. Once Step 6 determines values of λ_{design}, R, V, C_L, C_D, and the wake distribution, it designs the turbine based on BEMT model with velocity corrections. The detailed turbine design process can be found in Figure 4-7.

Step 7: Step 7 analyzes the turbine based on BEMT model with velocity corrections. Once Step 7 obtains the values of $\lambda_{operating}$, V, wake distribution, and the turbine geometry, the mathematical model is used to compute the turbine's power coefficient (C_p), power (P), thrust coefficient (C_t), and thrust (T_t). The energy yield of the turbine in each descent-ascent cycle (E_y) can be expressed as follows:

$$E_y = \frac{P * d_w * 2}{U_\infty} \tag{4-9}$$

Given that the acceleration phase of the system accounts for only a small portion of the total depth, the entire system's velocity is approximated as constant. The turbine blades are divided into distinct blade elements, and individual calculations are conducted for each. During these calculations, the

specific velocity and chord length corresponding to the location of each blade element are input to determine Re for that element. Using this Re, the hydrodynamic analysis is performed for each blade element to ascertain the load it experiences. Ultimately, the loads from each blade element are integrated to compute the turbine's overall performance.

Step 8: It computes B via Equation 4-8. The force equilibrium state equation is validated through Equation 4-10:

$$B = T_t + R_h \tag{4-10}$$

In summary, the first loop implements Steps 4 through 8 and aims to find the real moving velocity of the system (V_{real}) that satisfies the condition imposed by Equation 4-10. While the results from Step 7 represent performance at a certain velocity, this velocity may not necessarily correspond to V_{real} of the entire energy yield mechanism, which is currently unknown.

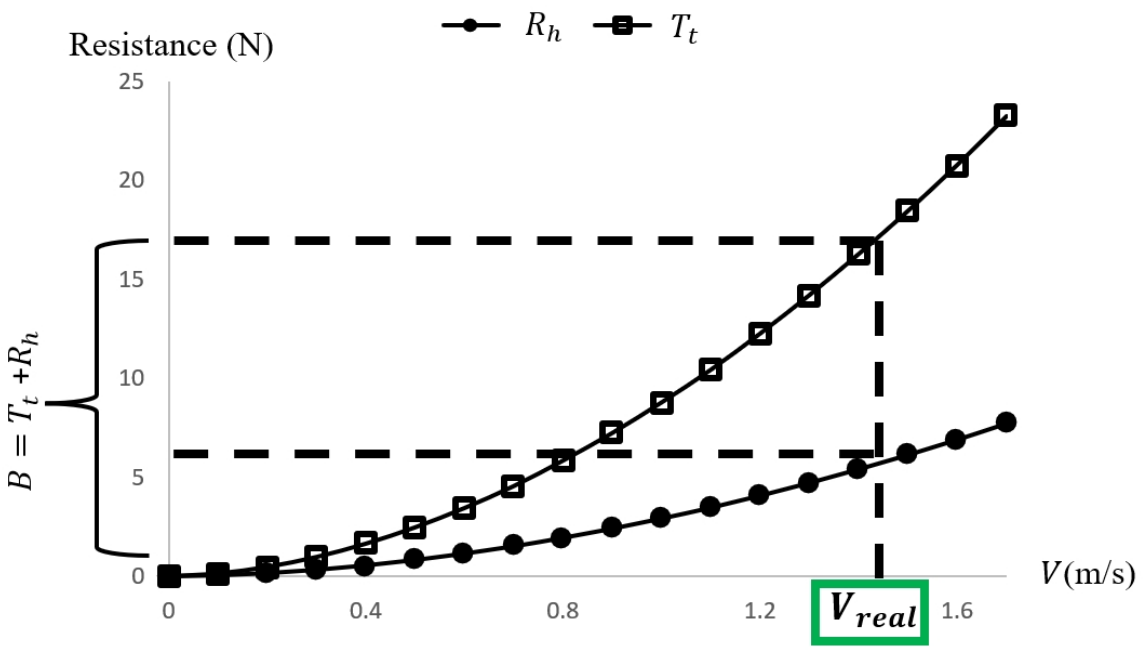

Figure 4-12. Function of the first loop

For any object to maintain a stable velocity, the external forces acting upon it must be in equilibrium. In the context of this study, the entire system comprises a turbine and UG hull. According to the force equilibrium equation (Equation 4-10), the combined resistance of UG hull

(R_h) and the turbine thrust (T_t) should equate to B . Thus, the inner loop introduces various values for V in order to pinpoint V_{real} that satisfies Equation 4-10. This process is depicted in Figure 4-12.

The second loop, running from Steps 2 to 9, functions as a counting loop. Steps 3 and 9 provide the mathematical model with potential operating TSR ($\lambda_{operating}$). This range is determined based on a specific value of λ_{design} . The lower bound of $\lambda_{operating}$ is set at 25%, while the upper limit is fixed at 200% of λ_{design} . Although each turbine within this mathematical model has its own λ_{design} , a turbine does not necessarily reach the highest energy yield E_y when running at λ_{design} . Hence, the second loop uses the inner loop (Steps 3 to 8) to find E_y for each $\lambda_{operating}$. This process then helps in identifying the optimal E_y for a specific turbine.

Step 10: This is an intermediate step between the second and the outermost loop, obtaining the optimal E_y among all $\lambda_{operating}$ of a specific turbine. This step validates the energy harvesting capability of a turbine. $\lambda_{operating}$ with the optimal E_y is defined as $\lambda_{optimal}$.

The outermost counting loop, spanning from Steps 1 to 11, provides the mathematical model with different sets of λ_{design} and R . This is done to explore the influence of λ_{design} and radius on the energy harvested (E_y). The objective is to determine the values of λ_{design} and radius that maximize E_y . Given that the optimal TSR for tidal turbines is approximately 4, and an exceedingly low λ_{design} can lead to oversized generators and power take-off mechanisms (Encarnacion et al., 2019), the range for λ_{design} is set from 2 to 6. Additionally, a very small radius can cause the turbine to operate within an intense wake, while an excessively large radius would render the turbine non-foldable and out of proportion relative to UG hull. Therefore, the radius is set to range between 0.06 m and 0.15 m.

Finally, upon finishing calculations across all loops, the mathematical model will yield the optimal turbine geometry that maximizes E_y across all λ_{design} and R values.

In this study, there are two coordinate system: Earth-fixed coordinate system and UG hull's own coordinate system. UG is moving in the coordinate system, whereas the turbine is rotating around the axis of UG hull.

4.3 Result of the mathematical model and the analysis

4.3.1 Optimal turbine

Upon completion of the flowchart shown in Figure 4-13, the mathematical model outputs the optimal E_y of turbines across various λ_{design} values and radii (R). This is illustrated in Figure 4-13(a). The output represents the turbine with the highest E_y, signifying it as the turbine optimally designed by the mathematical model. The geometry of this optimal turbine is depicted in Figure 4-13(b). Notably, the turbine has an expansive chord width. This is attributed to the mathematical model's determination that a low TSR results in the maximum E_y.

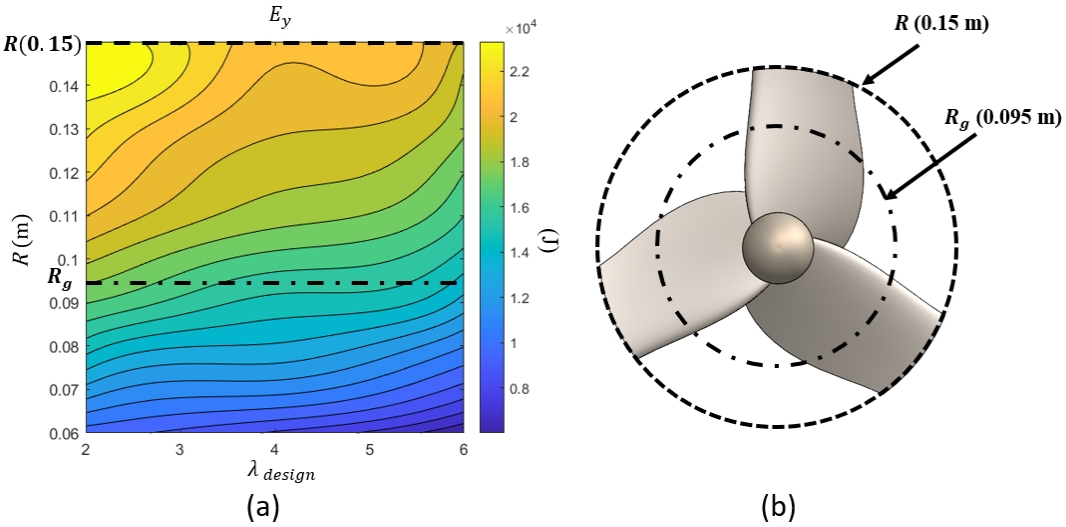

Figure 4-13. Turbine efficiency E_y comparison : (a) Various Radii and λ_{design}; and (b) Optimal turbine

4.3.2 Guidelines of mathematical model for turbine design

The result of Figure 4-13(a) can be used to guide the design principle in this study. Figure 4-13(a) shows that E_y increases with an increase in R and a decreasing in λ_{design}. E_y surges with an

increasing radius because the larger the radius, the more capable the turbine is at capturing energy, in competition with the hull. As depicted in Figure 4-14(a), during the entire energy harvesting process, the system moves vertically through the water. The hull can be simplified to represent a virtual disk that absorbs the kinetic energy from the flow, similar to the virtual actuator disc of the turbine, given its role in obstructing the incoming flow. Consequently, a part of the kinetic energy from the incoming flow is captured by the hull, with the turbine capturing the remainder. The process can be regarded as a contest between the hull and the turbine for kinetic energy, due to their sequential positioning illustrated in Figure 4-14(b).

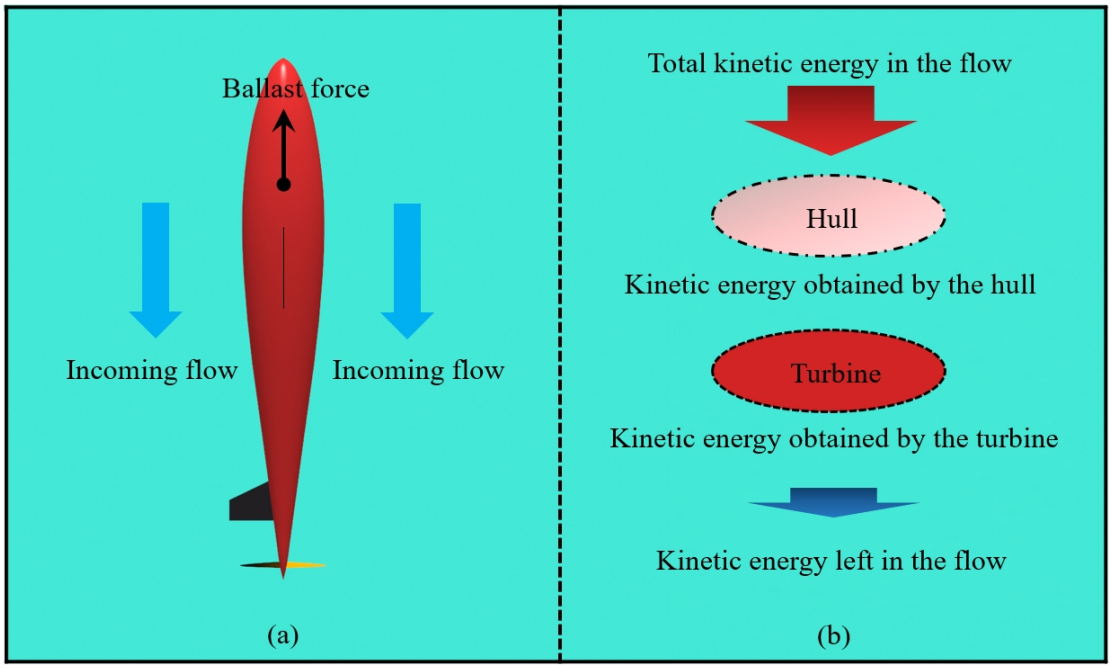

Figure 4-14. (a) Flow velocity; and (b) Kinetic energy competition

E_y decreases as λ_{design} because Re becomes smaller. As Re decreases, the hydrodynamic performance of the turbine deteriorates, as shown in Figure 4-6.

Figure 4-15 shows Re computed at 0.9 R of the turbine blade length, highlighting its changes across different R and λ_{design}. The position is chosen as 0.9 R, because in this section, Re asymptotes to the highest in the entire blade. In fact, the typical Re distribution along the radius of

the turbine blade is shown in Figure 4-15(b). Furthermore, it is notable that the blade element at 0.9 R contributes most to torque production.

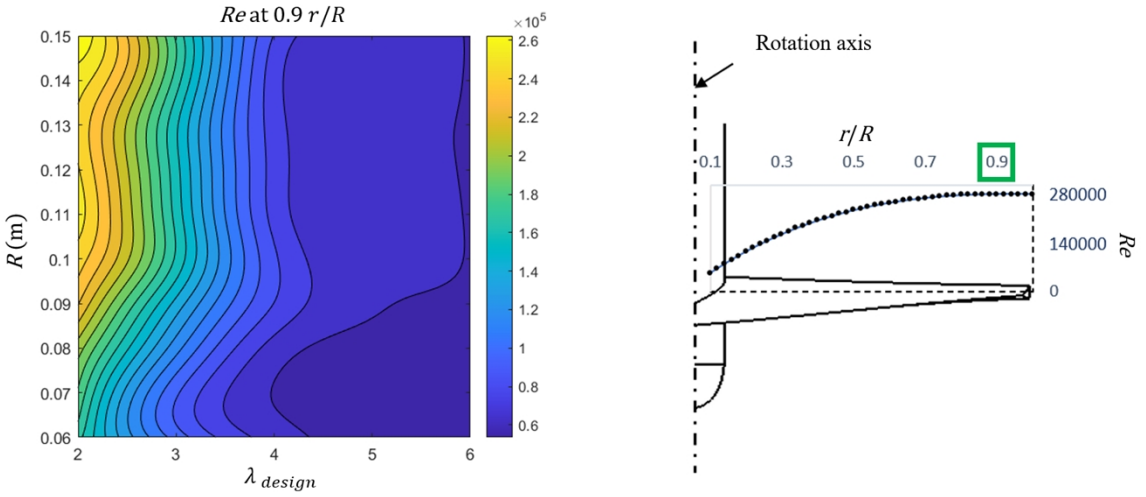

(a) (b)

Figure 4-15. (a) Re near the turbine tip (0.9 R) for different sets of λ_{design} and R; and (b) Typical Re distribution along the radius

The results from the mathematical model of a single case also show that high ratio of C_p and C_t ratio (C_p / C_t) should be pursued for a turbine design within this EHM. Figure 4-16(a) illustrates E_y and Figure 4-16(b) demonstrates C_p, C_t, and C_p / C_t versus $\lambda_{operating}$, for a turbine with R of 0.15 m and λ_{design} of 4. The results are plotted over $2 \leq \lambda_{operating} \leq 6$. C_p / C_t curve in Figure 4-16(b) exhibits the strongest correlations to E_y from Figure 4-16(a). E_y and C_p / C_t reach their maximum value at $\lambda_{operating} = 3$, while C_p peaks at $\lambda_{operating} = 4$.

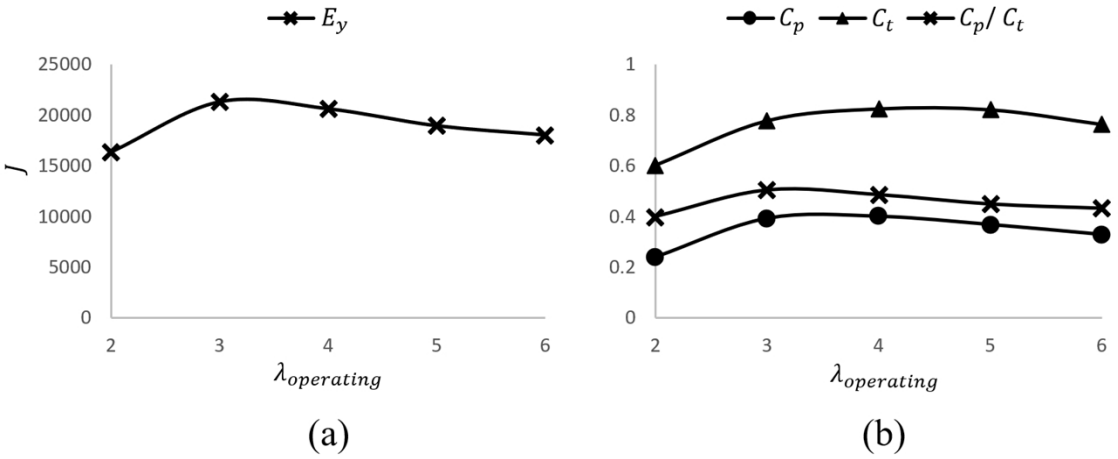

Figure 4-16. (a) E_y Vs $\lambda_{operating}$; and (b) C_p / C_t, C_p, and C_t Vs $\lambda_{operating}$

For turbines in EHM, it is evident that C_p / C_t provides a more accurate representation of E_y's pattern than C_p alone. This is because the working principle of the turbine differs fundamentally from that of traditional tidal turbines.

C_p is not a perfect indicator of energy harvesting capability anymore. This is due to the possibility of a higher C_p coexisting with a higher C_t, as illustrated in Figure 4-16(b). A high C_t can reduce the system's moving velocity, which also serves as the turbine's incoming velocity, subsequently diminishing the power and energy yield of the system. On the other hand, a high C_p / C_t ensures that the turbine can maintain a high C_p while mitigating the effects of reduced inflow speed caused by a high C_t. As a result, a high C_p / C_t leads to greater power and energy yield. Therefore, prioritizing a higher C_p / C_t becomes paramount during the design process of a single turbine in this EHM.

The multiple analysis of turbines with different sets of R and λ_{design} consistently supports the same conclusion. Figure 4-17 presents a comparison between C_p / C_t, C_p, and the power output (P) in Figure(a), (b), and (c), respectively, for various values of λ_{design} and R. Compared to C_p and P of the turbine, C_p / C_t displays a trend much more closely aligned with E_y as shown in Figure 4-13(a). Hence, the highest C_p / C_t yields the highest E_y. This correlation contrasts with the typical

operation of traditional turbine which solely aim for the highest C_p or P to maximise harvested energy only, without any consideration of thrust.

However, these conclusions are specific to UG hull in this study. The outcomes might change when choosing another hull with a higher C_t UG hull with a higher C_t might capture more energy in its competition with the turbine, resulting in a decreased E_y for the turbine and influencing the optimal C_p / C_t of the mathematical model.

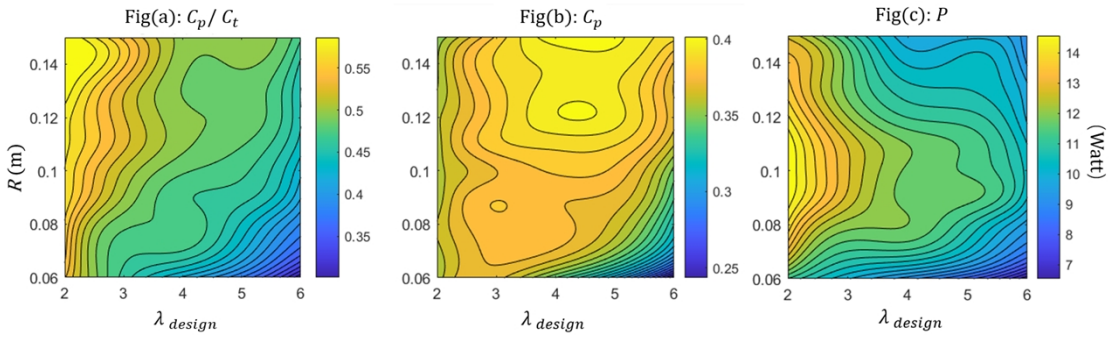

Figure 4-17. Turbin performances of turbines with different R and operating at different λ_{design}: (a) C_p / C_t; (b) C_p; and (c) P

As mentioned in Section 2.4.3.2, the turbine utilized for energy harvesting primarily operates as a force-to-velocity turbine. This operating principle differs from that of traditional velocity-driven turbines, which might be the reason for the unique relationship between E_y, C_p, C_t, and P when compared to traditional velocity-driven turbines.

The relationship between E_y, C_p, C_t, and P warrants thorough exploration and reflection. This research indicates that, for force-to-velocity turbines, achieving the highest C_p does not necessarily yield the highest P. More crucially, neither the highest C_p nor P directly correlates with the maximum E_y. In contrast, actuator disc theory, underpinned by the premise of a stationary actuator disc propelled by a defined incoming velocity, implicitly assumes that the maximum C_p corresponds to both the highest P and E_y. Therefore, it can be deduced that the dynamics between E_y, C_p, C_t, and P in force-to-velocity turbines deviate from the inherent assumptions of actuator

disc theory. This theory, which has guided preliminary turbine design for over a century, might face limitations when applied to the design of force-to-velocity turbines.

Furthermore, the phenomenon that a high C_p / C_t leads to a high E_y is of evident significance for designing force-to-velocity turbines. While this connection has been identified through extensive analytical data analysis, the underlying reasons for this phenomenon demand further exploration and comprehension.

4.3.3 Energy harvesting capacity of the system with the optimal turbine

The mathematical model indicates that this system can hydrodynamically harvest approximately 24.2 kJ of energy during one descent-ascent cycle in the energy harvesting mode when using the optimal turbine filled with 12 L (about 9.7 kg) of n-Pentadecane. Considering that the power consumption of a typical thermal UG during each descent-ascent cycle in gliding mode is approximately 6 kJ of energy (Davis et al., 2002, Falcão et al., 2018), it can be estimated that the energy harvested by the energy harvest system in a single cycle can support the energy consumption of UGs for four gliding mode cycles.

The hydrodynamic energy conversion efficiency (η_h) of the mechanism is defined as the efficiency from the hydraulic energy output of the thermal buoyancy engines to the hydrodynamic energy output of the turbine. η_h can be calculated by Equation 4-11.

$$\eta_h = \frac{E_y}{B_f * d_w * 2} \tag{4-11}$$

As mentioned above, the thermal buoyancy engines' ballast force is 25 N, and its working depth (d_w) is 1000 m. With an energy yield (E_y) of 24.2 kJ for one descent-ascent cycle on a hydrodynamic level, the energy harvesting system's efficiency (η_h) is approximately 48%. It is crucial to acknowledge that the energy yield reported in this study is calculated based solely on hydrodynamic forces, excluding the efficiency of the generator, which can range between 60% to 90%.

Additionally, system transmission losses have been overlooked. During the transition from thermal to hydraulic energy, the predominant transmission loss is due to hydraulic energy loss that transpires between the heat transfer and the accumulator. This loss primarily stems from the friction between the piston and the hydraulic cylinder's interior wall. Similarly, when converting hydraulic energy into the system's ballast force, the primary energy loss is in the hydraulic energy exchanged between the accumulator and the outer bladder, mainly because of friction between the piston and the cylinder wall. Hydraulic energy losses are contingent on the design and specificities of the hydraulic system, so an exact efficiency value cannot be established without a prototype. Generally speaking, the efficiency of hydraulic cylinders can reach 85% to 95%.

EHM's energy yield is contingent upon its operational depth, influenced by both working length and associated temperatures at different depths. To highlight the effect of working depth (d_w) on EHM's energy harvesting capability, varying depths d_w and their corresponding temperatures (T_l) were input into the proposed mathematical model. This provided the energy yield specific to each depth. The depth-temperature relationship is based on values measured by Argo program near the equator (Argo, 2023). The results are shown in Table 4-2, also showing the number of working cycles supported by different energy yields.

Table 4-2: Relationship between d_w , E_y , and cycle number

d_w (m)	T_l (°C)	E_y (kJ)	Cycle number
0	28	0 (Not functioning)	0 (Not functioning)
100	23.5		
200	12.9		
300	10.8		
400	9.8		
455	9.15		
500	8.3	11.3	1.9
600	7.2	13.8	2.3
700	6.3	16.5	2.7
800	5.6	18.8	3.1
900	5.1	21.2	3.5

When it is functioning, the results indicate that E_y gradually decreases as d_w decreases. This reduction is attributable to two primary factors: As demonstrated in Equation 4-9, d_w and E_y are directly proportional. Therefore, a shorter d_w corresponds to a decreased E_y; the increase in water temperature (T_l) with a smaller working depth (T_l) contributes to a reduced B. According to the working principle of the thermal buoyancy engine, the temperature of PCM (T_{PCM}) will drop to T_l at the given working depth. A higher T_l subsequently leads to a higher T_{PCM}. As indicated by Equation 4-6 and Equation 4-7, an elevated T_{PCM} at the working water depth causes an increase in V_{PCM_S}. Furthermore, as highlighted in Equation 4-8, this increased V_{PCM_S} consequently decreases B, leading to a further reduction in E_y.

For the given EHM, the critical depth is essential. EHM is unable to harvest energy in exceedingly shallow depths due to elevated water temperatures. The basic working principle of the thermal buoyancy engine stipulates that if the temperature at the underwater glider's working depth does not reach PCM's freezing point, the entire working cycle of the thermal buoyancy engine cannot be completed. This is because the hydraulic oil within the inner bladder does not return to heat transfer. In this study, the system's the critical depth is determined to be 455 m, aligning with a temperature of 9.15°C. This corresponds to PCM's freezing point employed, n-Pentadecane, as reported by (Vélez et al., 2015).

4.4 Conclusion

This study delves into a novel EHM designed for UG that employs a unique thermal buoyancy engine coupled with a turbine positioned behind the hull for energy harvesting. The conclusions derived from this work are as follows:

1. For efficient energy conversion between the engine and the turbine, a mathematical model was crafted using BEMT to discern the design aspects of an efficient turbine within this

system. To tailor BEMT to the distinct operating conditions of this turbine, the method was refined to account for the wake distribution following UG and the low operational Re.

2. Comprehensive analyses reveal that the relationship between E_y, C_p, C_t, and P for the turbine in this context deviates from conventional turbines. This distinction likely arises because the turbine used for energy harvesting functions as a force-to-velocity turbine, which operates fundamentally differently from traditional turbines.

3. The relationship between E_y, C_p, C_t, and P for force-to-velocity turbines is incompatible with the implicit assumptions of the actuator disc theory. This theory, which has steered preliminary turbine design for over a century, may face challenges when applied to the design of force-to-velocity turbines.

4. An intriguing observation from the mathematical model is that the design should lean towards a higher C_p / C_t ratio, as opposed to merely pursuing elevated C_p or P values, as seen in conventional turbine designs. While this observation stems from extensive analytical data, its underlying nature remains elusive and calls for more profound exploration in the future.

5. The mathematical model emphasizes the optimization of the turbine based on design TSR (λ_{design}) and radius (R). It suggests that the turbine's energy yield tends to rise with a decrease in λ_{design} and an increase in R.

6. Preliminary results from the mathematical model shed light on EHM's energy harvesting potential. The model demonstrates that the system, when loaded with 12 L (approximately 9.7 kg) of n-Pentadecane, can accumulate 24.2 kJ of energy in each descent-ascent cycle. With a working depth of 1000 m, the hydrodynamic energy conversion efficiency stands at 48%. This energy output could theoretically sustain UG's energy consumption for four gliding mode cycles, hinting at a self-sustainable UG system. This presents an optimistic perspective for explorative and rescue operations in marine environments, though component lifespan should

be considered. It should also be pointed out that EHM's energy yield decreases as the water depth reduces, and it will not operate at water depths less than 455m.

5 Expansion of the actuator disk theory and BEMT for the design of the force-to-velocity turbine

5.1 Introduction

Chapter 4, through rigorous data analysis, revealed that the relationship between E_y, C_p, C_t, and P in the turbine of EHM deviates from its counterparts in traditional turbines. A potential reason for this difference is that the turbine under study operates primarily as a force-to-velocity turbine, whereas traditional turbines function as velocity-driven turbines, each having its unique operating principles. The observed relationship for force-to-velocity turbines conflicts with the implicit assumptions made in the actuator disc theory, which envisages the actuator disc as stationary, propelled by a specified incoming velocity. Such divergence suggests that the actuator disc theory, an anchor in preliminary turbine design for over a century, may face challenges when applied to force-to-velocity turbines.

To delve deeper into the relationships between E_y, C_p, C_t, and P, as observed in Chapter 4, this chapter offers a mathematical explanation for the noted phenomena. This investigation led to a re-derivation and expansion of the actuator disc theory, one of BEMT's foundational pillars. Consequently, the conventional BEMT-based design methodology is also adapted based on the enhanced actuator disc theory. Moreover, understanding the relationship between E_y, C_p, C_t, and P remains paramount for designing force-to-velocity turbines.

Organized for clarity, Section 5.2 introduces the derivation of the Actuator Disk Theory for velocity-driven turbines. Section 5.3 expands upon the actuator theory specifically for force-to-velocity turbines and presents a revamped BEMT design approach. Section 5.4 validates the extended actuator theory and its associated design method. Section 5.5 elucidates the mathematical underpinnings of the relationship between E_y, C_p, C_t, and P as discerned in Chapter 4. Finally, Section 5.6 encapsulates the chapter's pivotal conclusions.

5.2 Derivation of the actuator disk theory for the velocity-driven turbine

As mentioned in Section 2.4.2, based on the momentum theory, (Betz, 1920) proposed a simplified actuator disc model and discerned that the turbine's efficiency or power coefficient C_P of a turbine possesses a theoretical upper limit of 59.3%, known as the Betz limit. (Betz, 1920) further observed that for the ideal turbine to achieve the Betz limit, it must be able to reduce the flow velocity by 1/3. This section presents the derivation process of Betz's theory. The side view of the simplified actuator disc and stream-tube model is shown in Figure 5-1. Here, U is the flow velocity; P is the pressure; P_D^+ is the pressure in front of the disc; and P_D^- is the pressure behind the disc. The symbol ∞ at subscript indicates the condition far upstream; D at subscript indicates the condition at the disc; and W at subscript indicates the condition far downstream.

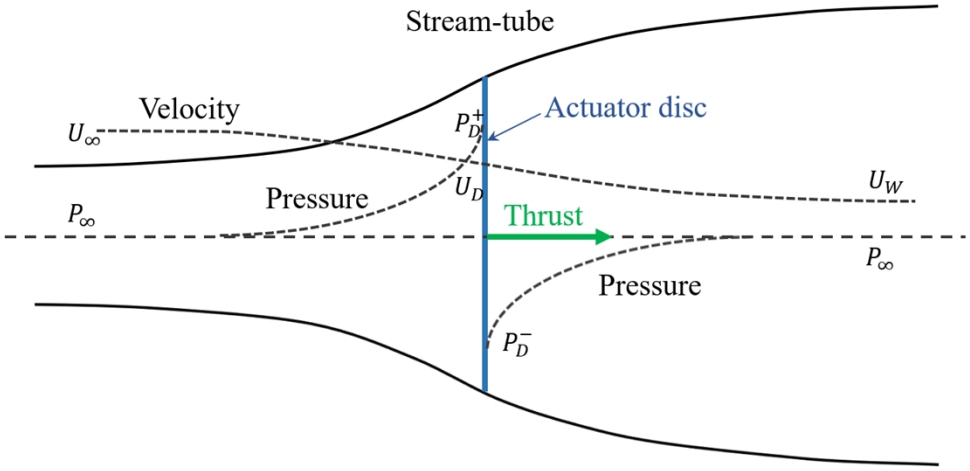

Figure 5-1. Side view of actuator disc and stream-tube model

With U_∞ and U_D, the axial induction factor a can be expressed by Equation 5-1 as follows:

$$a = \frac{U_\infty - U_D}{U_\infty} \tag{5-1}$$

The relationship between a and the power coefficient (C_P) along with the thrust coefficient（C_T）of the turbine can be derived using the momentum theory as follows (Betz, 1920):

As shown in Figure 5-1, the stream-tube keeps expanding from upstream to downstream. According to the mass conservation law, the mass flow rate keeps consistent everywhere, which can be expressed as follows:

$$\rho A_{\infty} U_{\infty} = \rho A_D U_D = \rho A_W U_W \tag{5-2}$$

where ρ is the flow density; A_{∞} is the cross-section of the stream-tube at far upstream; A_D is the cross-section of the stream-tube at the disc; and A_W is the cross-section of the stream-tube at far downstream.

As mentioned above, the flow passing through the actuator disc is shown below, which leads to the momentum change rate of the flow as follows:

$$Momentum\,change\,rate = \left(U_{\infty} - U_W\right)\rho A_D U_D \tag{5-3}$$

The force that leads to this momentum change rate is due to the pressure difference before and after the actuator disc, which can be expressed as follows:

$$(P_d^+ - P_d^-)A_D = (U_{\infty} - U_W)\rho A_D U_{\infty}\left(1 - a\right) \tag{5-4}$$

Bernoulli's equation is applied to the flow within the stream-tube. Derived from the principle of energy conservation, this equation asserts that the total energy of a fluid is conserved along a streamline in steady flow. This signifies that the sum of kinetic, potential, and internal energies within a streamline remains constant (Batchelor, 2000). Bernoulli's equation can be represented as follows:

$$\frac{1}{2}\rho U^2 + P + \rho g h = Constant \tag{5-5}$$

Considering the variation in total energy between upstream and downstream locations, Bernoulli's equation is applied separately to the upstream and downstream regions of the stream-tube.

By applying Bernoulli's equation to the flow upstream, the following expression is obtained below:

$$\frac{1}{2}\rho U_D^2 + P_D^+ = \frac{1}{2}\rho U_{\infty}^2 + P_{\infty} \tag{5-6}$$

Applying Bernoulli's equation in the downstream flow leads to equation as follows:

$$\frac{1}{2}\rho U_D^2 + P_D^- = \frac{1}{2}\rho U_W^2 + P_\infty \tag{5-7}$$

The relationship between Equations 5-6 and 5-7 can be expressed as follows:

$$\left(P_D^+ - P_D^-\right) = \frac{1}{2}\rho\left(U_\infty^2 - U_W^2\right) \tag{5-8}$$

To derive Equation 5-4 from Equation 5-8 through equating, it can be obtained as follows:

$$\frac{1}{2}\rho\left(U_\infty^2 - U_W^2\right)A_D = (U_\infty - U_W)\rho A_D U_\infty\left(1-a\right) \tag{5-9}$$

From Equation 5-9, U_W can be determined as follows:

$$U_W = \left(1-2a\right)U_\infty \tag{5-10}$$

Equation 5-10 indicates that 50% of the flow velocity reduction occurs upstream, and another 50% occurs downstream (Burton et al., 2011, Tony Burton, 2011).

By equating Equations 5-4 and 5-10, the thrust (T) acting on the actuator disc can be expressed through Equation 5-11:

$$T = \left(P_D^+ - P_D^-\right)A_D = 2\rho A_D U_\infty^2 a\left(1-a\right) \tag{5-11}$$

The thrust coefficient (C_T) can be expressed as follows:

$$C_T = \frac{T}{\frac{1}{2}\rho U_\infty^2 A_D} \quad . \tag{5-12}$$

With Equation 5-12, the relationship between C_T and a can be determined via Equation 5-13:

$$C_T = 4a\left(1-a\right) \tag{5-13}$$

Power (P) is the work done by T per second. Therefore, $P = TU_D$ can be expressed via Equation 5-14:

$$P = TU_D = 2\rho A_D U_\infty^3 a\left(1-a\right)^2 \tag{5-14}$$

The power coefficient (C_P) can be calculated as follows:

$$C_P = \frac{P}{\frac{1}{2}\rho U_\infty^3 A_D} \tag{5-15}$$

Consequently, the relationship between C_P and a can be expressed through Equation 5-16:

$$C_P = 4a(1-a)^2 \tag{5-16}$$

The relationship between C_T, C_P, and a is shown in Figure 5-2. The maximum value of C_P (0.5926), known as the Betz limit, is the theoretical maximum efficiency for any turbine.

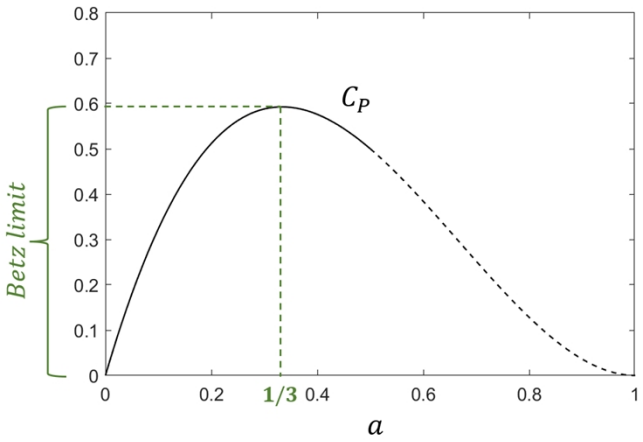

Figure 5-2. Relationship between C_P, C_T, and a

Also shown in Figure 5-2, a corresponding to the Betz limit is 1/3. This value can be obtained by computing the root of the function $\frac{dC_P(a)}{da}$ (De Lellis et al., 2018), which means for an ideal turbine to achieve the highest C_P. The turbine must reduce the flow velocity in front of it by 1/3 of U_∞. This conclusion forms the foundation of BEMT design method.

The above description highlights how Betz used the concept of an actuator disc to determine the optimal value of a for the actuator disc to achieve the maximum C_P based on momentum theory (Betz, 1920). However, in reality, a turbine is not just a simplified actuator disc; it consists of several blades. To determine the best geometry for these blades, one needs to integrate momentum

theory with BET. This integration leads to the development of BEMT, as extensively discussed in Section 2.4.2.

With the evolution of BEMT, the model for an ideal turbine and its design strategy can be determined based on the aforementioned the Betz limit and its associated optimal value of a. The main idea here is to set the momentum in the oncoming flow that the turbine should capture through the optimal a, and then deduce the best turbine geometry using this value. Given that the design basis for the turbine geometry is $a = 1/3$, when the turbine operates under its designed working conditions, the flow velocity in front of the turbine will be reduced by 1/3 of U_∞. This reduction leads to the maximum C_P as per Betz's theory.

5.3 Optimal a and design method for force-to-velocity turbine

For the force-to-velocity turbine, EHM is shown in Figure 3-4. While the relationship between C_P and a is still governed by Betz's theory, the velocity (U) passing through and driving the force-to-velocity turbine is the velocity of the platform. This velocity is also a function of the thrust generated by the turbine, linking with the axial induction factor a. For instance, the higher a means the turbine extracts more momentum from the flow, which leads to higher thrust slowing down the velocity. As a result, the highest C_P of the force-to-velocity turbine does not necessarily lead to the highest power (P) nor the highest energy yield (E_y). This means that $a = 1/3$ is no longer a prerequisite for the force-to-velocity turbine, and the design for this type of turbine remains uncertain.

In the following sections, this study aims to re-establish the actuator disk theory and BEMT for the force-to-velocity turbine, identifying the relationships among power P, energy E_y, and the axial induction factor a. This thesis expands and proposes a new BEMT design method, aiming to determine the optimal geometry of force-to-velocity turbines.

5.3.1 Expansion of the actuator disk theory for the force-to-velocity turbine

5.3.1.1 Optimal a for power

In Figure 2-5, the carrying platform of the force-to-velocity turbine is predominantly identified as an axisymmetric body, such as UGs. The turbine is defined as R. Its thrust coefficient is C_T. The radius of the carrying platform is r. The resistance coefficient of the platform body is C_d expressed as Equation 5-17.

$$C_d = \frac{R_h}{\frac{1}{2}\rho U^2 \pi r^2} \tag{5-17}$$

To study the relationship between a, P, and E_y for the force-to-velocity turbine, the turbine within EHM is similarly conceptualized as an actuator disc, consistent with Betz's theory (Betz, 1920) discussed earlier.

When the system is harvesting energy by driving the turbine up and down in the ocean, the system's ballast force (B) is the sum of the turbine thrust and platform resistance, as shown in Figure 5-3.

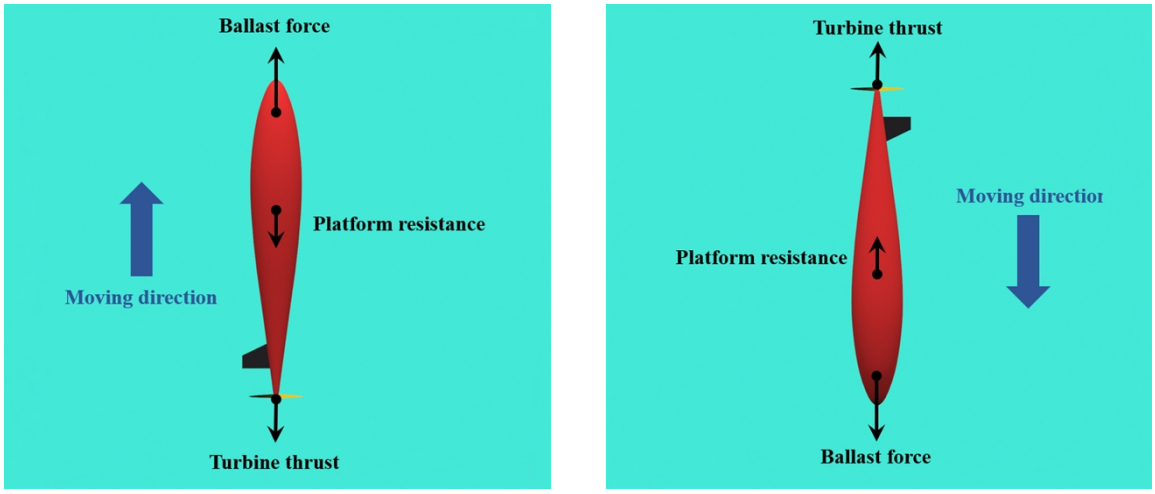

a) Ascending (Gravity<Buoyancy) b) Descending (Gravity>Buoyancy)

Figure 5-3. Forces of UG during the energy harvesting

The relationship can be expressed as Equation 5-18:

$$B = C_T \frac{1}{2}\rho U^2 \pi R^2 + C_d \frac{1}{2}\rho U^2 \pi r^2 \tag{5-18}$$

where ρ is the fluid density and U is the moving velocity of the whole platform.

According to the actuator disc theory, the function between a and C_T can be established, as shown in Equation 5-13. Substituting Equation 5-13 into Equation 5-18, the moving velocity (U) in below Equation 5-19 can be derived. The flow velocity through the turbine is contingent upon the specific designs of the turbines and platforms, which in turn directly impacts on the amount of energy harvested.

$$U = \sqrt{\frac{B}{\frac{1}{2}\rho\pi R^2\left(4a(1-a) + C_d \frac{r^2}{R^2}\right)}} \tag{5-19}$$

To calculate the maximum power that the system can harvest, by substituting Equation 5-19 into Equation 5-14, power (P) of the force-to-velocity turbine can be expressed as a function of a, as shown in Equation 5-20.

$$P(a) = B^{\frac{3}{2}}\left(\frac{1}{2}\rho\pi R^2\right)^{-\frac{1}{2}} \frac{4a(1-a)^2}{\left[4a(1-a) + C_d \frac{r^2}{R^2}\right]^{\frac{3}{2}}} \tag{5-20}$$

P is a function of B, R, r, C_d, and a. For a specific carrying platform, B and the platform radius (r) are predetermined according to the mission requirements, such as payload, volume of inner units. Therefore, this study normalizes these by setting their values to 1, rendering a non-dimensional power. Consequently, it is evident that the power is only relating to R, C_d, and a. To discern the relationship between P, R, C_d, and a.

This thesis examines P across different combinations of R, C_d, and a. within a reasonable range. The result is shown in Figure 5-4, where C_d is from 0 to 0.4, a is from 0.01 to 0.5, and R is from 0.1 to 2. The graph is colored based on power values.

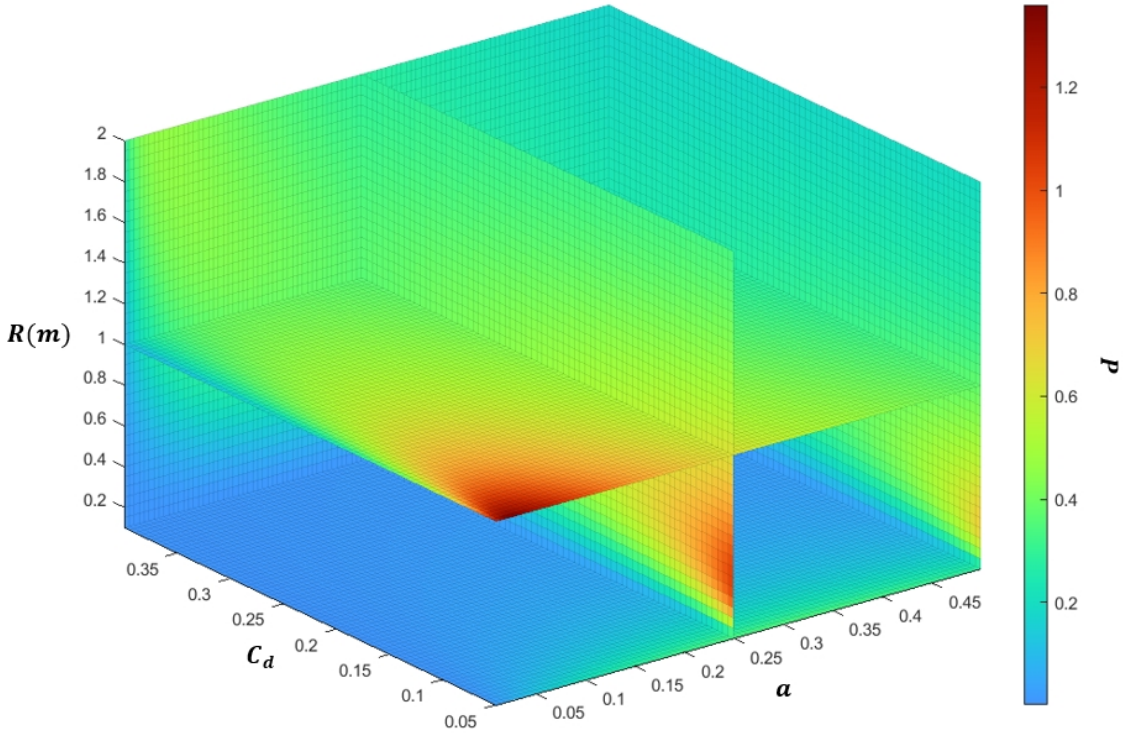

Figure 5-4. Relationship between R, C_d, a, and P

From Figure 5-4, it can be observations can be made: P decreases as C_d increases; P does not exhibit a monotonous behavior with variations in R. Most significantly, from the section where $R=1$, it can be observed that P is depending on the axial induction factor (a). To further understand this change, Figure 5-5 presents the corresponding conditions for the peak power to be achieved. Here, it can be observed that the optimal a for the peak power decrease with the increase of R and conversely, it increases with the increase of C_d.

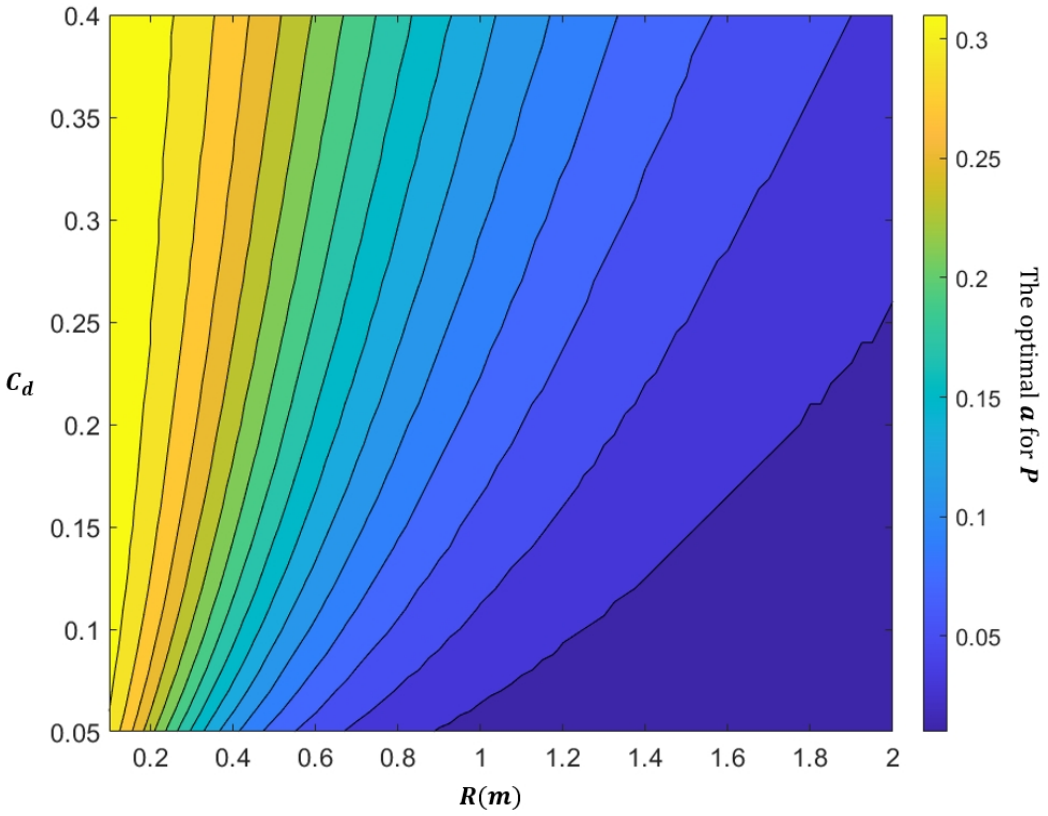

Figure 5-5. Optimum a with the highest P at different C_d and R

5.3.1.2 Optimal a for energy

Based on the derivations in the previous section, a question arises: Does achieving maximum power guarantee the highest energy yield: With the thermal glider as a use case — where gliders capitalize on thermal energy and undergo dive cycles to propel the turbine — this chapter shifts its focus to the energy yield per operational cycle and delves into the interplay between the energy yield and the axial induction factor a .

The operation cycle time (t) for the force-to-velocity turbine encompassing one dive and ascend cycle can be expressed by Equation 5-21:

$$t = \frac{L}{U} \tag{5-21}$$

where L is the working distance which is twice the working depth of the thermal gliders.

Subsequently, E_y can be expressed as follows:

$$E_y = P\frac{L}{U} \tag{5-22}$$

By equating Equations 5-19, 5-20, and 5-22, the expression can be obtained as follows:

$$E_y(a) = BL\frac{4a(1-a)^2}{4a(1-a)+C_d\frac{r^2}{R^2}} \tag{5-23}$$

The work input by the carrying platform is defined as W_k. According to the definition of work, W_k can be expressed via Equation 5-24:

$$W_k = BL \tag{5-24}$$

By equating Equations 5-23 and 5-24, the relationship between E_y and W_k can be defined as follows:

$$E_y = W_k\frac{4a(1-a)^2}{4a(1-a)+C_d\frac{r^2}{R^2}} \tag{5-25}$$

E_y is a function of L, B, R, r, C_d, and a. As mentioned in above section, for a specific carrying platform, B, r, and working length (L) are defined according to the mission requirement. This thesis sets these values as 1 to have a non-dimensional E_y. Therefore, E_y is only relating to R, C_d, and a. To study the relationship between R, C_d, and a. Figure 5-6 shows the correlation of E_y regarding to R, C_d, and a.

From Figure 5-6 and Equation 5-25, E_y increases with the increase of R. This is clearly opposite to the trend of P as observed in Figure 5-4. This underlines the necessity for a balanced turbine radius selection during design. While a turbine with a larger diameter may harvest more energy per cycle, it does so at a slower rate. In real-world applications, a larger diameter could also pose risks such as accidental collisions, leading to potential damage to the blades.

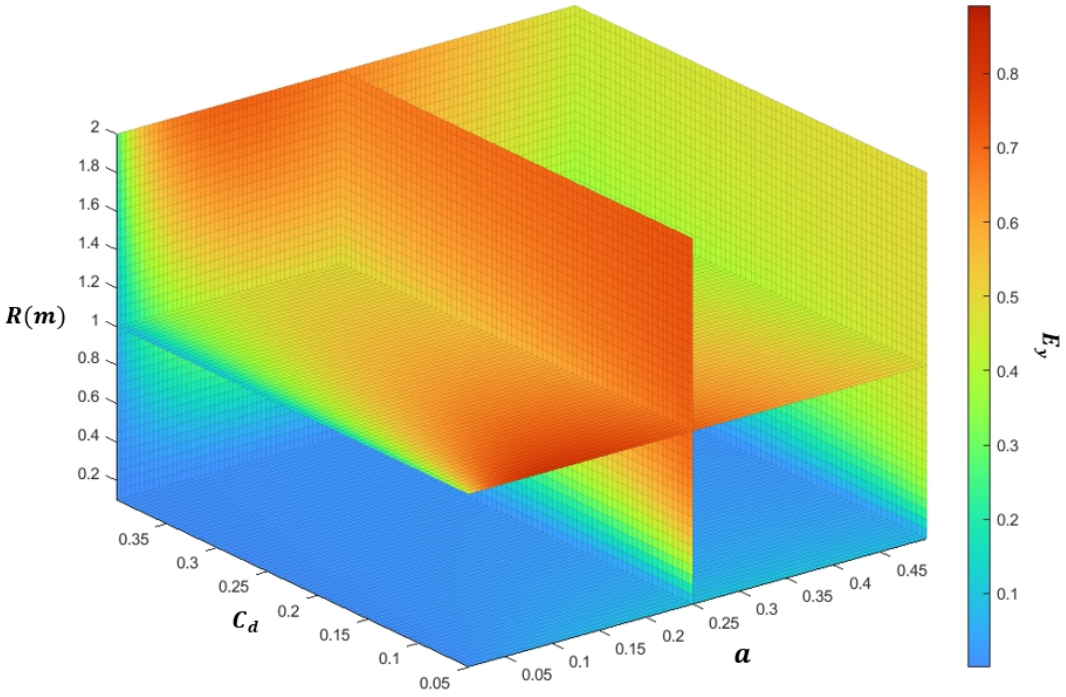

Figure 5-6. Relationship between R, C_d, a, and E_y

Furthermore, the power output from a turbine with a larger diameter might be too low for practical energy harvesting by generators. This distinctive behavior is a departure from what is observed in velocity-driven turbines and demands careful attention during design.

Similarly, as with P, E_y decreases with the increase of C_d. The highest E_y no longer occurs at $a = 1/3$. Figure 5-7 explains the corresponding conditions for peak E_y to be achieved. The optimal a for peak E_y, mirroring the pattern for peak P, decreases with the increase of R and increases with the increase of C_d.

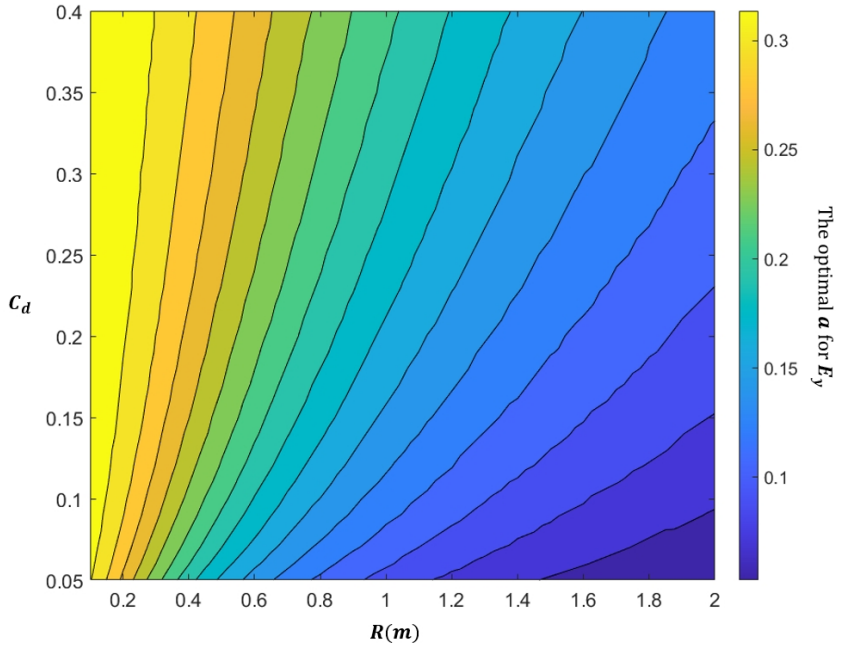

Figure 5-7. Corresponding a for the highest E_y at different C_d and R

5.3.1.3 Efficiency η_m

In traditional actuator disk theory used for the velocity-driven turbine, C_P describes the efficiency. Higher C_P leads to higher E_y. However, as previously mentioned, for force-to-velocity turbines, the highest C_P does not necessarily lead to the highest energy yield E_y. Therefore, there is a need to introduce a new efficiency parameter specifically for force-to-velocity turbines. In this chapter, η_m is proposed as the efficiency for force-to-velocity turbines, as presented in Equation 5-26.

$$\eta_m = \frac{E_y}{W_k} = \frac{4a(1-a)^2}{4a(1-a) + C_d \frac{r^2}{R^2}} \tag{5-26}$$

Optimal a derived from the Betz limit no longer applies to the force-to-velocity turbine, because the optimal a turns to the root of $d\eta_m(a)/da$ from the root of $dC_P(a)/da$. The maximum efficiency achievable by a force-to-velocity turbine is dependent on the resistance coefficient of the carrying platform, the radius ratio between the carrying platform and the turbine, and the turbine's axial induction factor. This efficiency does not necessarily peak when $a = 1/3$.

5.3.2 Development of BEMT-based design method for preliminary design of the force-to-velocity turbine

The preliminary design method for the force-to-velocity turbine varied from the preliminary design method for the velocity-driven turbine in Section 2.2.

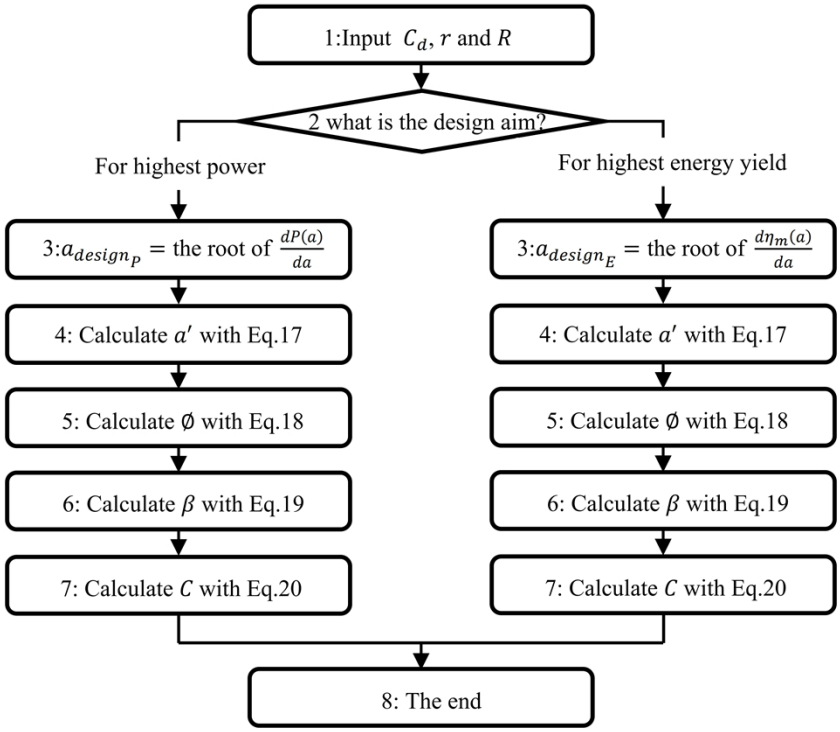

Figure 5-8. Flowchart of the new BEMT design method for the force-to-velocity turbine

The new design flowchart is shown in Figure 5-8 as follows: Step 1 determines the three design parameters of the carrying platform and the turbine, including C_d , r , and R ; Step 2 decides the design goal; Step 3 determines a_{design} by calculating the root of the function $dP(a)/da$ or $d\eta_m(a)/da$, which denote as a_{design_P} and a_{design_E} , respectively; This then calculates the optimal C and β with a_{design} using BEMT design method introduced in Section 2.2.

This design method holds significant relevance only when the projected area of the turbine and the hull in the direction of the incoming flow are roughly equivalent in magnitude. If the hull's projected area or radius is substantially larger than that of the turbine, the turbine's influence on

the system's moving velocity becomes marginal. In such cases, the turbine's operational state more closely resembles that of a velocity-driven turbine. Consequently, the turbine would behave similarly to the actuator disc in Betz's theory. Whether aiming for the highest P or E_y, its optimal a would approach 1/3. This behavior is evident in Figures 5-5 and 5-7, where the optimal a tends toward 1/3 as the turbine radius decreases. Thus, for RAT in the rocket-powered fighter illustrated in Figure 2-36, which has a size much smaller than the hull, this design methodology would only marginally alter the optimal a in Betz's theory, resulting in a negligible increase in P or E_y.

5.4 Verification

In the previous discussions, this work established the relationship between a, P, and E_y for the force-to-velocity turbine. The findings underscore that $a = 1/3$ does not invariably yield the highest P and E_y for a force-to-velocity turbine, marking a departure from Betz's theory for the velocity-driven turbine. Furthermore, attaining optimal power and energy necessitates varied turbine designs. This work subsequently introduced a new BEMT design methodology specifically for the force-to-velocity turbine, oriented either towards maximum power or energy. The next logical step is to validate this novel design approach via a case study.

Section 5.4 is organized as follows: In Section 5.4.1, the principle of BEMT analysis code is introduced with the case study configuration and the procedure of the verification; In section 5.4.2, the results are presented and discussed.

5.4.1 Verification method

In the verification, this study continues to employ BEMT analysis method mentioned in Section 2.5.1.1 to analyze the energy conversion performance for the designed turbines.

5.4.1.1 Reference carrying platform of the verification

Three parameters of EHM: C_d, r, and R are determined through the carrying platform. As mentioned in Section 3.3, the hull shape in this case remains unchanged from Section 3.3, with the

only difference being the radius. In this chapter, a new carrying platform is used, the radius of the carrying platform (r) is set to 0.1 m. The geometry is shown in the Figure 5-9.

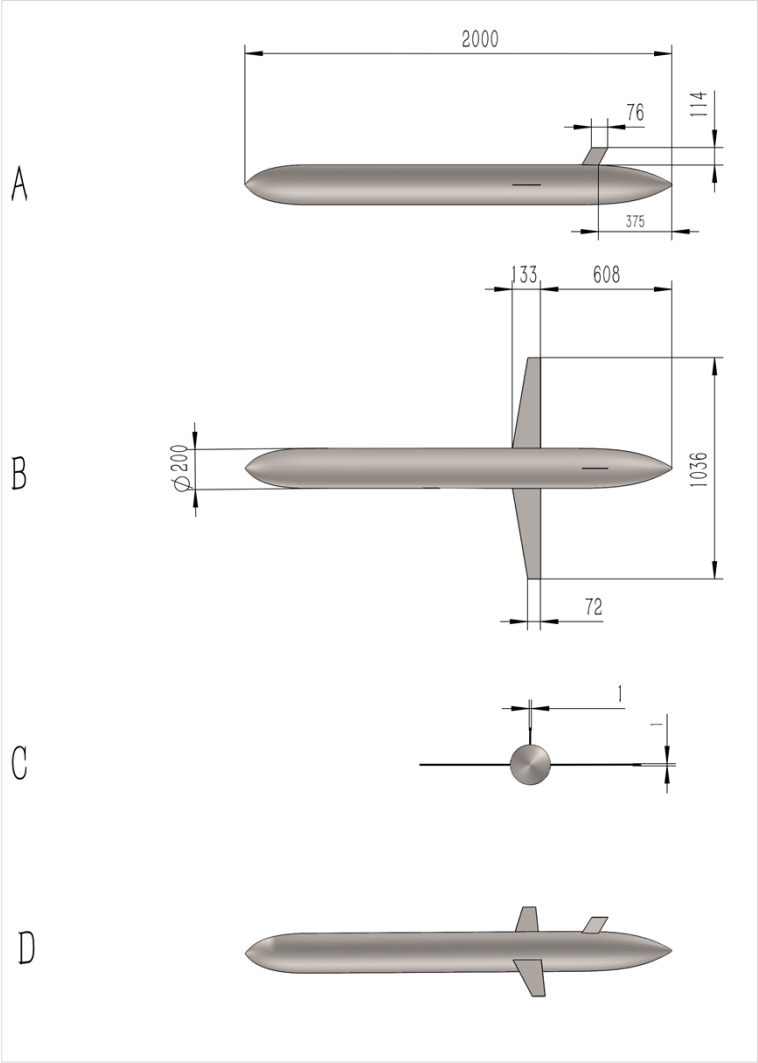

Figure 5-9. Geometry of carrying platform in Chapter 5: (a) Side profile; (b) Top profile; (c) Rear profile; and (d) Perspective profile

CFD simulations are executed using the commercial software STAR-CCM+, facilitating an exploration of C_d of the hull. Considering the balance of the thesis structure, the detailed specifics of CFD simulation setup have been placed in Appendix B, including the computational domain, boundary conditions, grid structure, solution methodology, and grid independence verification. CFD simulations show that C_d is around 0.2 in a wide speed range from 1 m/s to 4 m/s; for

simplicity, C_d of is set as 0.2. B is set at 25 N. After the consideration of the balance between E_y, P and risk of accidental collision, R is set at 0.15 m. The blade number (N) is set as 3.

To simplify the analysis, two assumptions have been made. Firstly, the hydrodynamic impact from the wake trailing the platform can be disregarded. While the turbine is positioned behind the carrying platform and might be influenced by the platform's wake, this effect is minimal. This is largely because carrying platforms are typically designed as streamlined symmetrical bodies that produce minimal wake shadowing. Secondly, the varying influence of Re on the turbine sections is overlooked. While Re of the blades might fluctuate across different designs and operational conditions, such variances are generally minimal within a specific range and can therefore be disregarded in this context. Thus, C_L and C_D characteristics of the blade sections remain consistent across different Re. The blade sections employ NACA0015 foil profile, with C_L and C_D displayed in Figure 5-10. C_L and C_D values for the foil are sourced from XFoil software simulations. The blade's design angle of attack (α) is set at 6 degrees, which corresponds to the foil's maximum lift-to-drag ratio. λ_{design} is established at 4, a standard value for tidal turbines (Encarnacion et al., 2019).

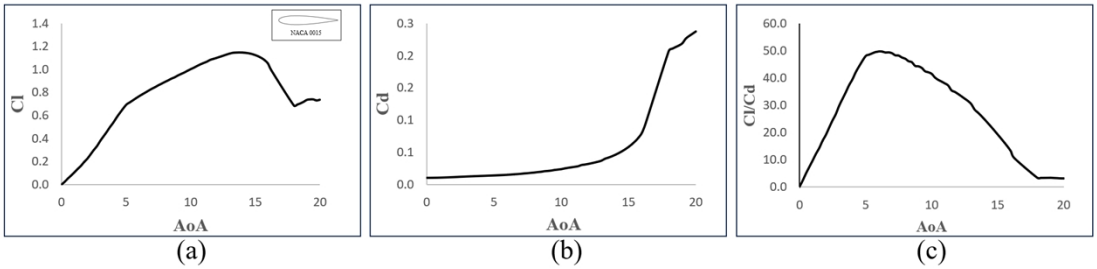

(a) (b) (c)

Figure 5-10. Hydraulic parameters of NACA 0015: (a) Lift coefficient; (b) Drag coefficient; (c) Lift-drag ratio

5.4.1.2 Procedure of the verification

In this verification, the turbine was initially designed using all potential axial induction factors. Subsequently, the designed turbines were analyzed with the carrying platform under all feasible operational conditions. This approach ensures that the newly developed design method can be

compared and verified with the optimum solutions, thereby fostering confidence in the method's effectiveness. The procedure of the verification is shown in Figure 5-11, which can be divided into 12 steps.

Step 1: Input the design parameters of the carrying platform and the turbine, including C_d, r, R, C_L, C_d, λ_{design}, N, and B.

Steps 2 and 11: Form a loop that can input a set of α to design and build all the possible turbine blades to be analyzed in all the possible working conditions. In this study, the investigated range of α is from 0.01 to 0.5 with an interval of 0.001, with 491 unique α in total. Therefore, 491 unique turbines have been simulated to find the optimum design.

Step 3: Set α as λ_{design}.

Step 4: Generate a turbine with λ_{design} based upon BEMT design method shown in Section 2.2.

Steps 5 and 9: Form a loop simulating different working conditions for the turbine generated from Step 5. The working conditions indicate the different operating TSR ($\lambda_{operating}$). The range of $\lambda_{operating}$ is from 1 to 7 with an interval of 0.25.

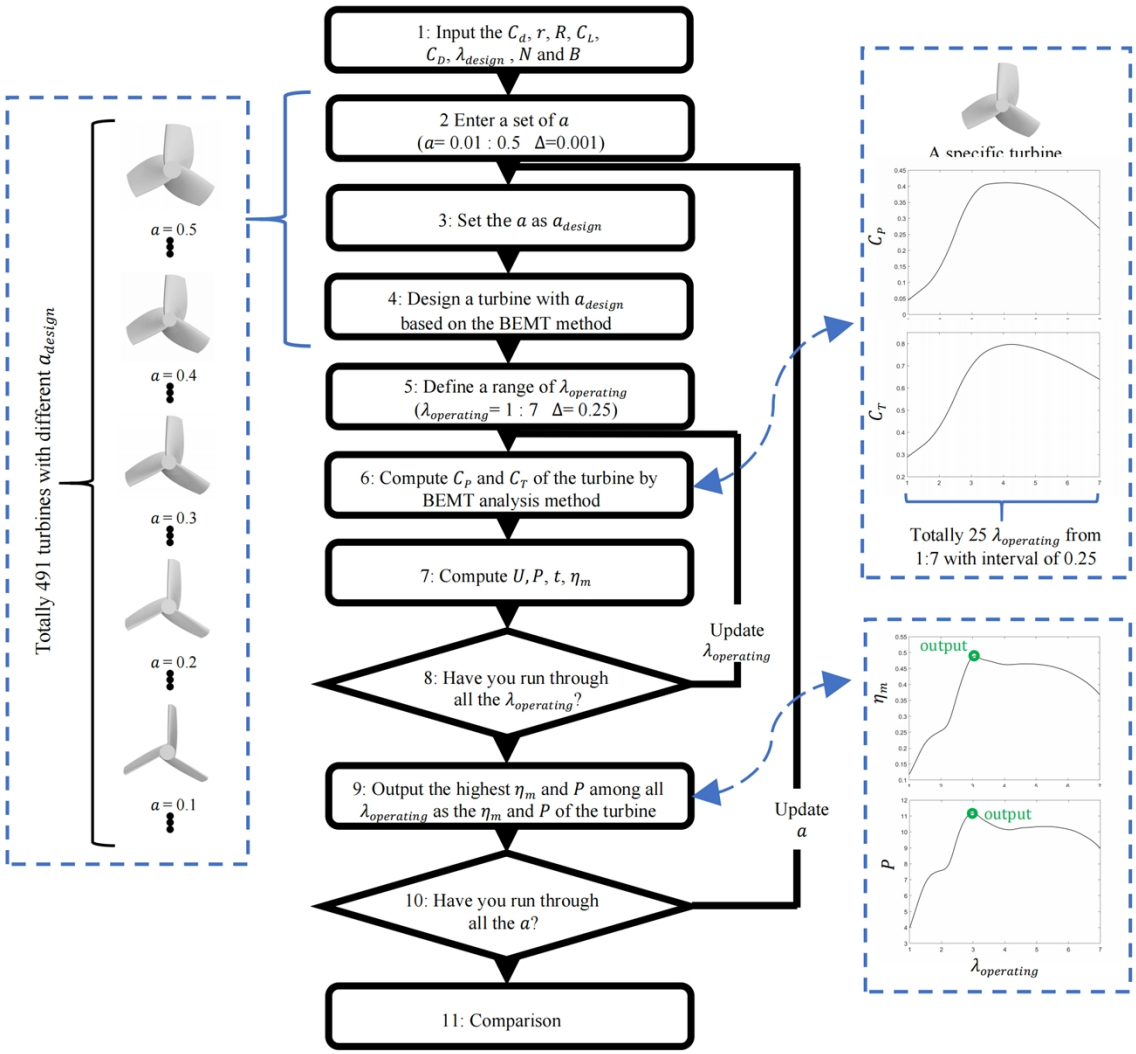

Figure 5-11. Flowchart of verification study for finding optimum turbine in operational conditions

Steps 6 to 8: Analyze η_m of the turbine under a specific $\lambda_{operating}$. The detail of these three steps is expressed as follows:

Step 6: Using BEMT analysis method, C_P and C_T were analyzed. For this purpose, each turbine blade was divided into 17 blade elements. Iterations were employed to pinpoint the values of α and a' for each blade element, allowing for the calculation of the foil load. Initially, both α and a' were set to zero. The inflow angle (ϕ) was then determined with Equation 2-3. The angle of attack (α) was computed using Equation 2-4, which then provided the values for C_L and C_D for

each blade element. Next, the tangential coefficient (C_t) and the normal coefficient (C_n) for every foil segment were deduced using Equations 2-6 and 2-7, respectively. The chord solidity (σ_r) was ascertained using Equation 2-8. With the known C_t and C_n values, α and a' for the flow impacting the foil segment were calculated using Equations 2-9 and 2-10. The recalculated α and a' values replaced the initial estimates, and the calculations were repeated. This iterative process continued until the deviation in a and a' values was less than 0.01 in this study. After iteration, results, including W , C_t , and C_n , were used to assess the torque and thrust for each blade element according to Equations 2-11 and 2-12. Subsequently, by integration, the overall thrust and power of the turbine were determined. Finally, the thrust coefficient and power coefficient were computed using Equations 2-13 and 2-14.

Step 7: Compute the moving velocity of the system (U), the power (P), the work time (t), and the energy conversion efficiency (η_m) of the turbine.

Step 9: Output the highest η_m and P of a turbine among all the possible $\lambda_{operating}$.

Step 11: Compare the result with the result obtained using the new method.

5.4.2 Result of the verification

In Figure 5-12, two curves are presented: First, it is the theoretical value of η_m from Equation 5-26 based on the actuator disk theory, demonstrating the relation of η_m and a . Secondly, the maximum value of η_m is analyzed using the proposed BEMT method at all possible *a*. Similarly, Figure 5-13 represents the theoretical value of P from Equation 5-20 based on the actuator disk theory and the analyzed maximum P with all the possible a .

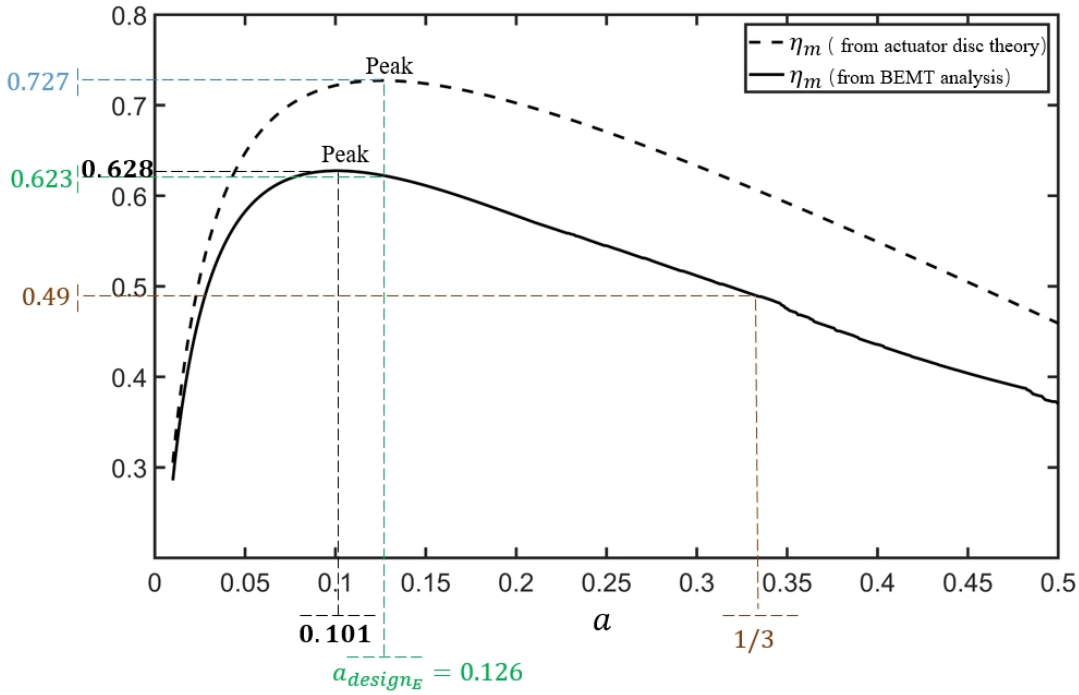

Figure 5-12. η_m based on actuator disc theory and η_m from the analysis

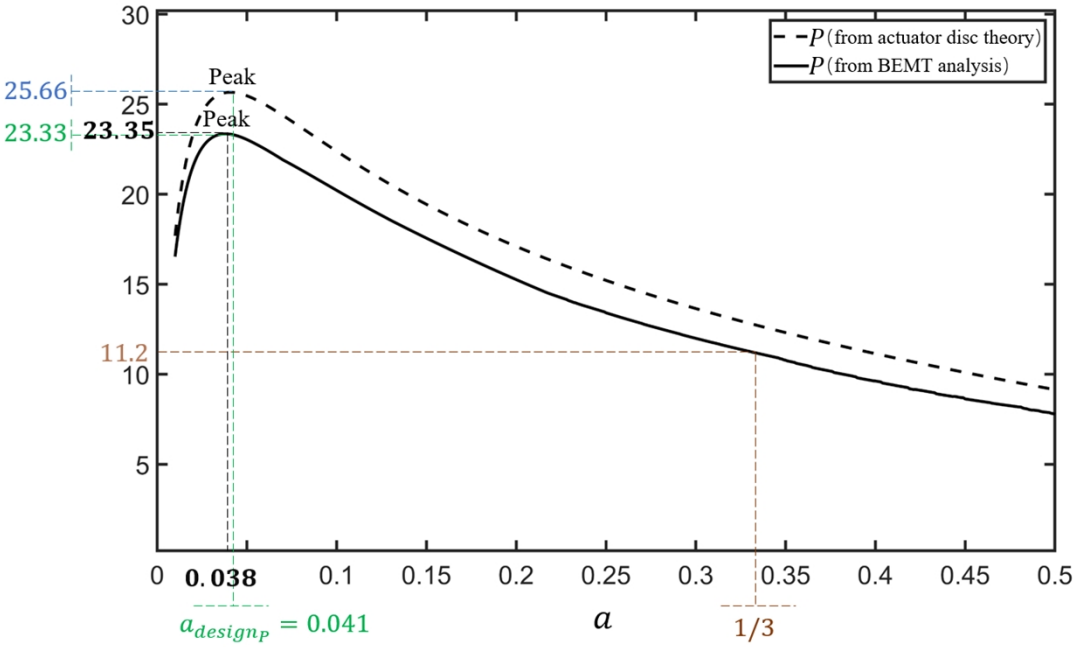

Figure 5-13. P based on actuator disc theory and P from the analysis

The results in Figure 5-12 and Figure 5-13 show that $a = 1/3$ no longer leads to the highest energy yield or the highest power for the force-to-velocity turbine. This confirms the previous findings based on the actuator disc theory. In this specific case, the analysis result shows that $a_{design} = 0.101$, it achieves the highest η_m and $a_{design} = 0.038$ results in the highest power.

In examining the results for the 491 turbines depicted in Figure 5-12 and Figure 5-13, it becomes evident that η_m and P values derived from the actuator disc theory consistently exceed those obtained from the analysis. This discrepancy stems from the inherent idealized assumptions of the actuator disc theory, which include considerations like a non-rotating wake, an infinite number of blades, and the assumptions of steady and inviscid flow, among others. Consequently, for the force-to-velocity turbine, both η_m and P as based on the actuator disc theory can be viewed as the theoretical maximum limits. These upper bounds are primarily influenced by C_d of the platform and the radius ratio. Conveniently, these upper bounds can be easily approximated during the design phase, providing valuable guidance for determining the design metrics of EHM at its initial stages. For instance, in Figure 5-12, the theoretical upper limit for η_m is 0.727, whereas the highest observed η_m from the 491 turbines stands at 0.628. Similarly, as displayed in Figure 5-13, the theoretical maximum P for this case study is 25.66 W, while the peak P from the analyzed turbines is 23.35 W.

From Figures 5-12 and 5-13, the variation trends of η_m and P from actuator disc theory closely align with those derived from BEMT analysis. Correspondingly, as shown in Figure 5-12, when targeting the highest E_y, a_{design_P} is 0.126 based on the actuator disk theory, while BEMT analysis method shows it can be achieved at $a_{design} = 0.101$. However, the difference caused by the shift of a_{design_P} is minimum. Therefore, a_{design_P} based on the actuator disk theory is feasible and effective to be used to design the turbine for the highest energy yield. As shown in Figure 5-13, when aiming for the highest P, a_{design_P} is 0.041 based on the actuator disk theory, and BEMT analysis method shows it can be achieved at $a_{design} = 0.038$ which is close to the predicted value.

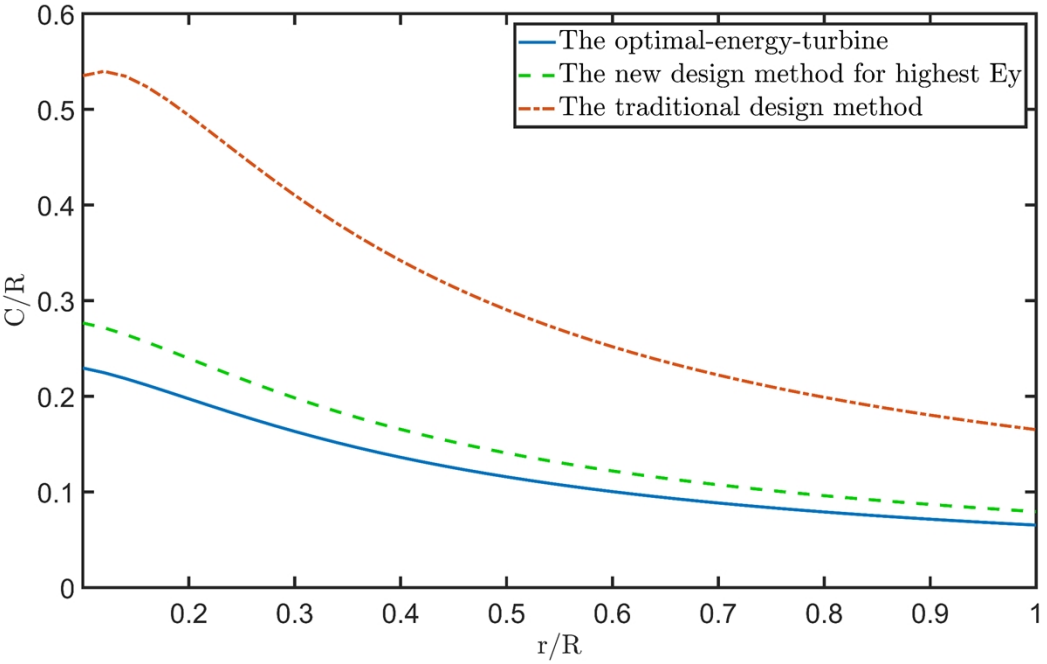

Figure 5-14. Comparison of dimensionless chord length

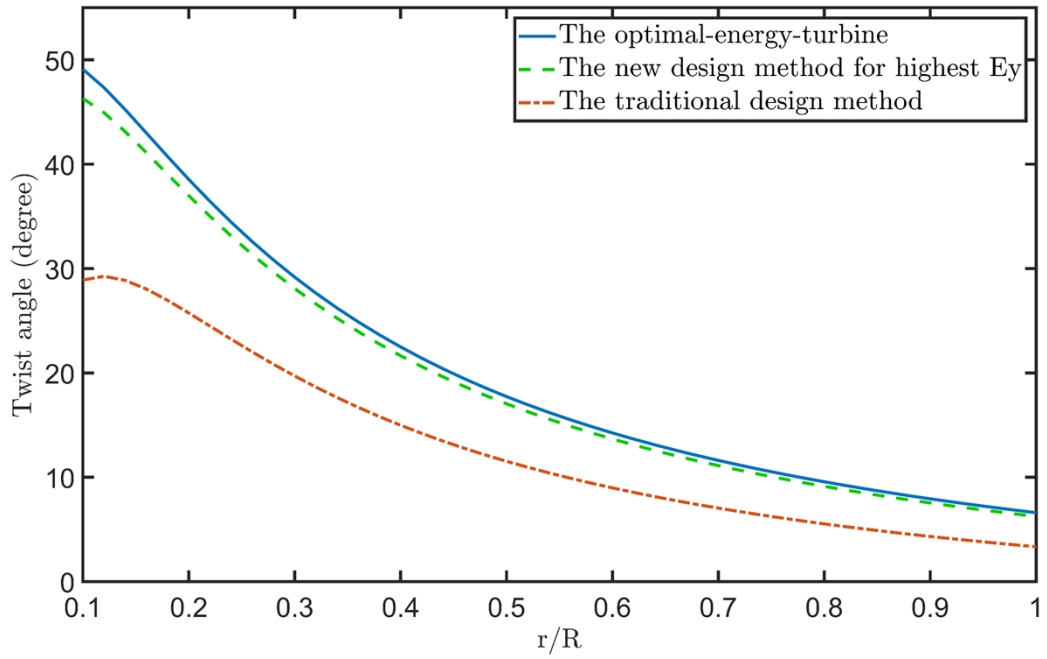

Figure 5-15. Comparison of twist angle

Furthermore, Figure 5-14 and Figure 5-15 compare the dimensionless chord length (C/R) and the twist angle (β) along the radius between the optimal-energy-turbine found among all possible designs, the turbine designed with the optimal a for energy based on the expanded actuator disk theory, and the turbine designed with a =1/3. The results clearly depict that the turbine designed leveraging the expanded actuator disk theory for the force-to-velocity turbine closely mirrors the optimal design. This indicates that the introduced theory effectively pinpoints optimal turbine designs, confirming its validity and applicability.

Similarly, Figures 5-16 and 5-17 compare the dimensionless chord length (C/R) and the twist angle (β) along the radius between the optimal-power-turbine found among all possible designs, the turbine designed with the optimal a for power based on the expanded actuator disk theory and the turbine designed with a =1/3.

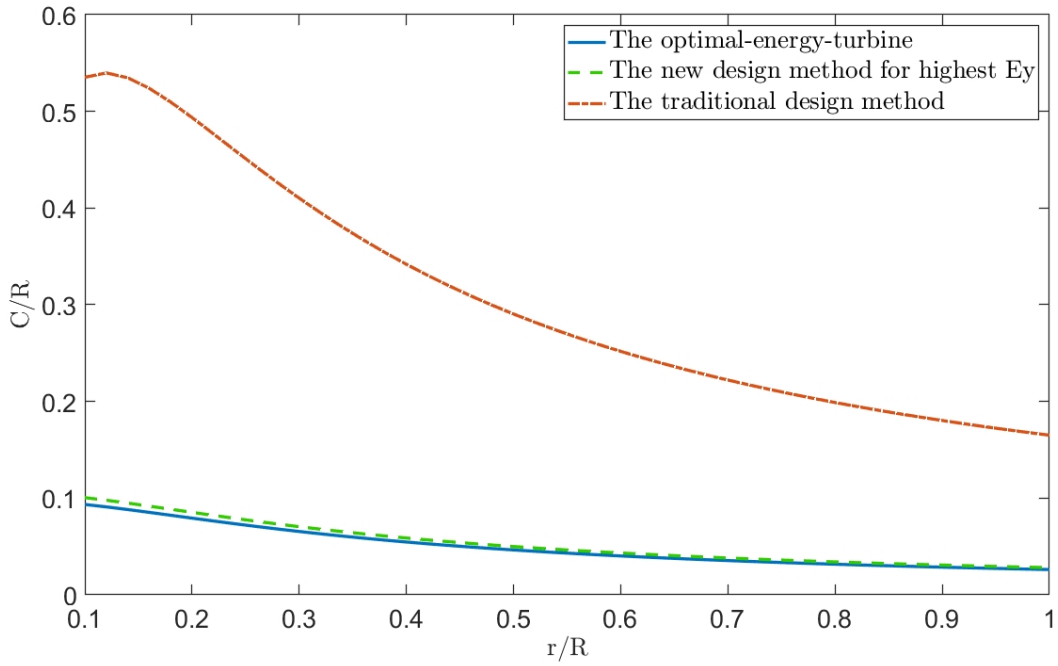

Figure 5-16. Comparison of dimensionless chord length

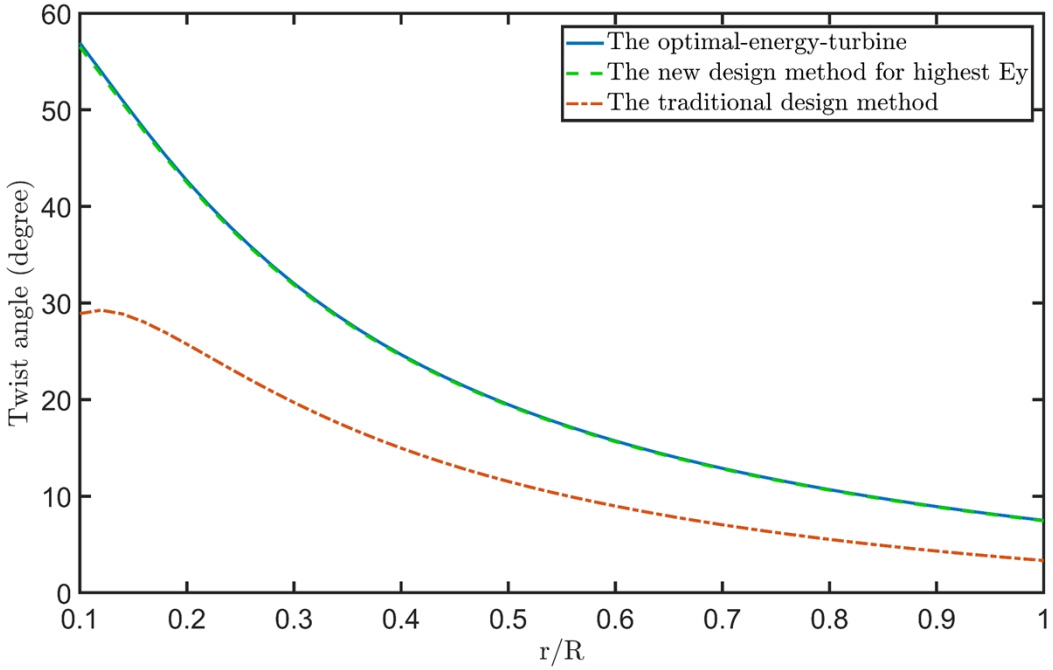

Figure 5-17. Comparison of twist angle

5.5 Explanation for the relationship between E_y, C_p, C_t, and P

In Chapter 4, a unique pattern was discerned: the relationship between E_y, C_p, C_t, and P for force-to-velocity turbines diverged significantly from that of velocity-driven turbines. One particularly striking discovery was that in force-to-velocity turbines, a higher C_p / C_t often resulted in a higher E_y. At that juncture, the selected grasp on the intrinsic cause of this phenomenon was preliminary, based largely on comprehensive data observation. Nonetheless, as the study delved deeper into the expanded actuator disc theory in the subsequent sections, the thesis garnered a mathematical comprehension that illuminated the intricacies of the observations from Chapter 4.

By substituting Equations 5-13 and 5-16 into Equation 5-20, the relationship between C_p, C_t, and P of the force-to-velocity turbine can be expressed via Equation 5-27:

$$P = B^{\frac{3}{2}} \left(\frac{1}{2} \rho \pi R^2 \right)^{-\frac{1}{2}} \frac{C_p}{\left[C_t + C_d \frac{r^2}{R^2} \right]^{\frac{3}{2}}} \tag{5-27}$$

By substituting Equations 5-13 and 5-16 into Equation 5-23, the relationship between C_p, C_t, and E_y of the force-to-velocity turbine can be expressed via Equation 5-28:

$$E_y = BL\frac{C_p}{C_t + C_d\frac{r^2}{R^2}} \tag{5-28}$$

Equations 5-27 and 5-28 provide a mathematical interpretation of the phenomenon, which is observed and the concluded in Chapter 4.

It is concluded that a high C_p / C_t ratio would yield a high E_y. However, Equation 5-28 provides a nuanced understanding of this relationship, suggesting that it is actually a high $C_p / (C_t + C_d * (r^2 / R^2))$ ratio that results in a high E_y, not necessarily C_p / C_t. This slight oversight in Chapter 4 can be attributed to the particularities of the case study, where $C_d(r^2 / R^2)$ values were relatively modest. In essence, the earlier conclusion was a generalization, which while mostly accurate for the specific case study, might not hold universally. However, it is crucial to highlight that this oversight does not drastically compromise the earlier findings. The parameters like C_d, r, and R selected for Chapter 4 case study were informed by practical considerations. For EHMs of this nature, $C_d(r^2 / R^2)$ values are not typically large, making the conclusions from Chapter 4 applicable in a majority of scenarios.

5.6 Conclusion

In order to adapt the actuator disc theory and the corresponding BEMT-based design method for the force-to-velocity turbine addressed in this study, this chapter expanded the actuator disk theory. It further developed BEMT design method tailored for the force-to-velocity turbine. A verification study was conducted, confirming the validity of the developed theories and methods. From this study, several conclusions can be drawn:

1. Based on the expanded actuator disk theory, $a = 1/3$ no longer leads to the highest P nor the highest E_y for the force-to-velocity turbine. Thus, Betz's actuator disc theory, which is suitable for velocity-turbine design, is not applicable to the force-to-velocity turbine.

2. New theoretical upper bounds for the energy conversion efficiency and the power of EHM have been identified for force-to-velocity turbine to guide the design.

3. An expansion of the actuator disc theory revealed that the power P is a function of B, ρ, R, r, C_d, and while E_y is a function of B, L, R, r, C_d, and a. A turbine designed for high power does not lead to a high-energy. Therefore, two different optimal design targets have been proposed.

4. A new BEMT-based design method for the preliminary design of force-to-velocity turbine has been developed. The method facilitates design of turbines aligned with specific objectives, be it achieving the highest E_y or the highest P.

5. The verification study has been conducted with BEMT method to design and simulate a plethora of potential designs across a spectrum of operating conditions. The results have been compared with the expanded actuator disk theory. The developed method proved highly effective in identifying the optimal designs.

6. The relationship between the C_t, C_p, P, and E_y for the force-to-velocity turbine observed in Chapter 4 is interpreted mathematically in this Chapter. The relationship between C_p / C_t and the E_y concluded in Chapter 4 is well explained by an equation. Concurrently, the chapter evaluates the effectiveness and limitations of C_p / C_t and E_y summarized in Chapter 4, offering a deeper understanding via mathematical insights.

6 CFD verification of the energy harvesting capability for the turbine-based EHM equipped with a turbine designed based on previous findings

6.1 Introduction

In previous discussions, this work exhaustively analyzed the operational mechanism of the turbine in the turbine-based EHM. Chapter 4 presented general design philosophies for the turbine, which can guide the selection of design parameters. Conversely, Chapter 5 deeply explored the operating principles of this turbine type, challenging traditional turbine design methodologies at their core. Chapter 6 seeks to synthesize the insights from both Chapters 4 and 5 to create a final turbine design and assess the energy harvesting prowess of a turbine-based EHM fitted with this turbine.

Previous chapters utilized a BEMT-based mathematical model, idealizing EHM working conditions and overlooking the hydrodynamic interplay between the hull and the turbine. The hull's rotation, resulting from turbine torque, was also set aside. Additionally, BEMT's framework posits certain idealizations, such as a steady, inviscid, incompressible flow without radial and circumferential variances, among others. Such idealizations may compromise model accuracy. However, the model's moderate accuracy sufficed for prior discussions, as it captured EHM's trend of E_y with design parameter variations. This facilitated the elucidation of the design philosophy and even allowed a mathematical interpretation of observed trends, an expansion of the actuator disc theory, and the birth of a design technique tailored for the force-to-velocity turbine in Chapter 5.

Nevertheless, when evaluating EHM's energy harvesting potential, BEMT model's moderate accuracy can offer only a preliminary result. Hence, high-fidelity CFD simulations are essential. This chapter employs the distilled turbine design philosophy and the newly-minted BEMT-based design method to design an optimal turbine. This turbine is then subjected to CFD analysis to confirm EHM's energy harvesting capabilities and viability. EHM's competitive edge against other

OTEC-PCM options is then gauged based on CFD findings. Additionally, this chapter juxtaposes BEMT model outcomes against CFD results to determine the mathematical model's precision.

Within this framework, Section 6.2 delineates CFD simulation's test case, while Section 6.3.2 elaborates on the simulation's numerical setup. Section 6.3.2.4 delivers the simulation findings and discussion. Finally, Section 6.4 encapsulates this chapter's primary takeaways.

6.2 Test case

This section discusses the design considerations of EHM in the verification process, including the carrying platform and turbine.

Choice of carrying platform

The choice of carrying platform (UG hull) and its working conditions remains consistent in Section 3.3. Therefore, the hull resistance remains unchanged and is expressed via Equation 4-5.

$$W_f = -36474r^5 + 19372r^4 - 3364.5r^3 + 162.79r^2 + 9.4378r + 0.1977 \quad (6\text{-}1)$$

In this chapter, the distance between the hull and turbine was set to 4 cm, where the relationship between the wake factor (W_f) and radial coordinate (r^e) is expressed through Equation 6-1 according to CFD simulation. The working depth (d_w) of the system is at 1000 m, and the ballast force (B) is 25 N.

Turbine design parameter considerations

The first step involves determining the turbine design parameters based on the design philosophy concluded in Chapters 4 and 5. These parameters encompass the radius (R), the design TSR (λ_{design}), and the blade number (N).

As mentioned in Chapter 4, for EHM in this study, a low Re of the foil leads to reduced energy yield (E_y). As illustrated in Figures 5-12 and 5-13, the new design method for force-to-velocity turbines lowers λ_{design} value compared to the traditional design method (1/3). A lower λ_{design} results

in smaller chord lengths and further decreases E_y. Consequently, turbines designed using the new BEMT-based method experience a reduction in E_y due to the low Re. To address this issue, appropriate design parameters should be selected to increase Re of the foil.

A promising approach to maintaining a higher Re is to increase the chord length without changing the rotational velocity, given that Re is proportional to the product of chord length and velocity. According to Equation 2-5, N is in the denominator on the right side of the formula. Decreasing N can increase chord length and Re under the foil operates. Therefore, N is set to 2.

In Chapter 4, it was concluded that low λ_{design} results in high Re and increased E_y. Therefore, λ_{design} is maintained at 2, consisting with the setting in Chapter 4.

Both Chapters 4 and 5 show that increasing the radius (R) can enhance E_y of the turbine, as illustrated in Figures 4-13 and 5-6. Consequently, R should be as large as possible, which remains at 0.15m.

The foil section continues to utilize NACA 0015, in line with previous chapters.

Turbine design method

In Chapter5, this study expanded Actuator Disk Theory and propose a new BEMT-based design method for force-to-velocity turbines based on this expanded theory. While the study was focused, the influence of wake and low Re were set aside, potentially causing discrepancies between BEMT's assumptions and the turbine's actual working conditions, as mentioned in Section 2.4.3.1. Although the influence of wake is marginal for turbines with $R = 0.15$, this chapter considers the velocity corrections to ensure thoroughness.

Therefore, the velocity corrections proposed in Section 4.2.1.2 will be incorporated into the new BEMT design method for force-to-velocity turbines proposed in Section 5.3.2. As a result, Figure 6-1 represents the final form of this new BEMT design method after incorporating the corrections, serving as the ultimate implementation of the concept presented in Figure 2-40.

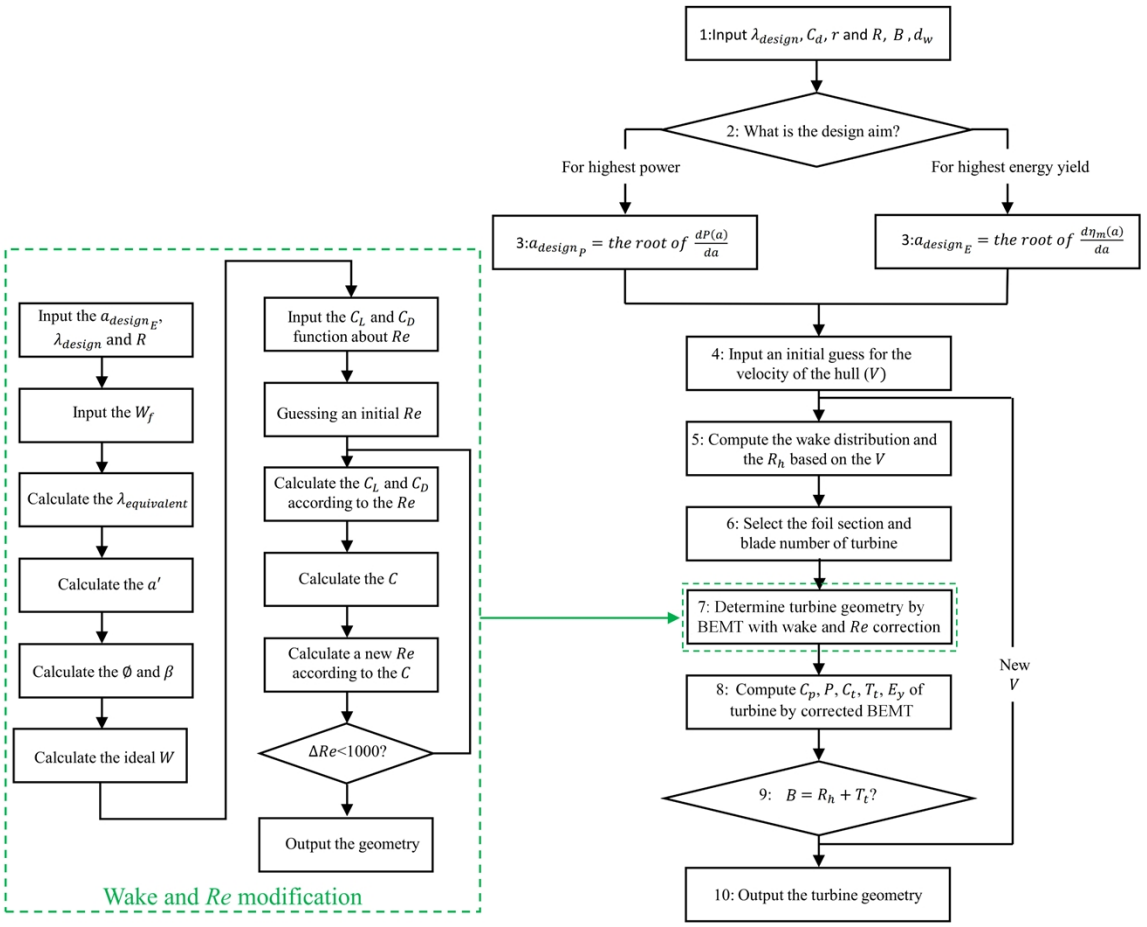

Figure 6-1. New BEMT-based design method for force-to-velocity turbine with the velocity corrections

From Figure 6-1, Steps 1 to 3 mainly correspond to Steps 1 to 3 of the new BEMT-based design method for force-to-velocity turbines shown in Figure 5-8. These steps include the aim judgment and the calculation of the optimal axial induction factor (a). Meanwhile, the first step also inputs the design parameters of the carrying platform and the turbine, including λ_{design}, r, R, B_f, d_w, which have been discussed earlier. Since C_d value in the considered area lies between approximately 0.21 to 0.19, this study simplifies the approach by assigning a C_d of 0.2 to calculate the optimal a for energy yield or power in the third step.

Upon identifying the optimal a, the next step is to integrate the turbine design stages that account for wake and Re effects, as discussed in Section 4.2, to Step 3. As highlighted earlier, in the design

process that takes Re into account, UG's moving velocity has a direct impact on the Re under which the blade operates. This, in turn, affects the turbine's ideal geometry. However, the initial movement velocity of UG remains undetermined. Therefore, this study integrates a loop within Steps 5 to 9 to discern the system's ultimate movement velocity and the related Re value that the turbine geometry should cater to. The seventh step focuses on the turbine's design with velocity adjustments, as previously detailed in Section 4.2.1.2. Subsequently, Step 8 utilizes BEMT analysis method, accounting for the effects of wake (Section 4.2), to predict the turbine's thrust (T_t). Given that Steps 4 to 10 have been extensively covered in Section 4.2, they will not be reiterated here.

Turbine geometry

This study focuses on designing a turbine with the highest E_y. Based on this design objective, the new method reveals an optimal axial induction factor for energy yield (a_{design_E}) of 0.121. Using a_{design_E}, the optimal turbine geometry is obtained, as displayed in Figure 6-2. The detailed information of the turbine geometry is shown in

Table 6-1. The complete geometry of the system is illustrated in Figure 6-3.

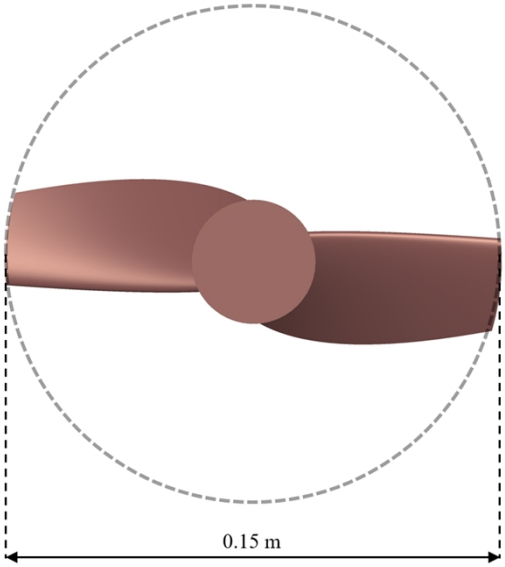

Figure 6-2. Turbine geometry in the verification

Table 6-1: Detailed geometry of the turbine in verification

r/R	0.25	0.3	0.4	0.5	0.6	0.7	0.8	0.9	1
Chord length (mm)	54.4	67.4	78.8	80.0	77.1	74.4	69.8	64.8	60.1
Twist angle (deg)	33.7	33.8	32.0	28.9	25.8	23.3	20.7	18.4	16.4

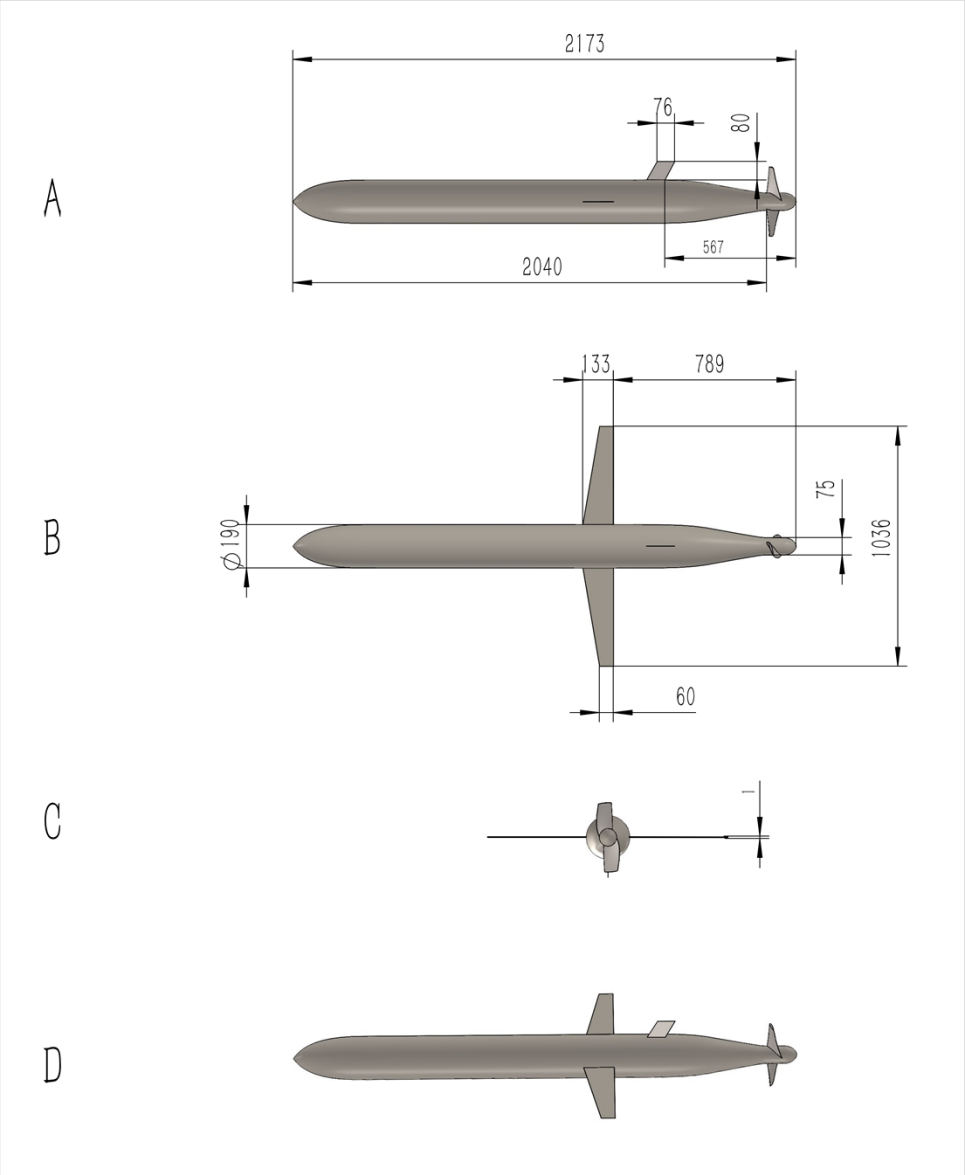

Figure 6-3. Geometry of the whole system in the verification: (a) Side profile; (b) Top profile; (c) Rear profile; and (d) Perspective profile

6.3 Numerical analysis method

In this chapter, the energy harvesting capability of the turbine-based EHM will be assessed using two numerical analysis techniques: BEMT and CFD.

6.3.1 BEMT method

In this chapter, BEMT analysis will utilize the mathematical model from Chapter 4. Chapter 4 presented a BEMT-based model tailored for evaluating the energy harvesting capabilities of the turbine-based EHM, as depicted in Figure 4-10. Using this model again, the primary distinction is that the turbine's design has been solidified with defined parameters, eliminating the need for further design input. With the turbine's geometry already ascertained, the relevant R and λ_{design} values are fed into the model at Step 1 as illustrated in Figure 4-10. Subsequently, Step 2 will automatically define varying λ_{design} or the turbine, allowing for the assessment of EHM under diverse operational conditions.

The process then engages a loop from Step 2 through Step 9, as outlined earlier, to holistically compute the energy harvesting capabilities of the turbine-based EHM. The established turbine geometry, encompassing blade chord lengths and twist angles, is inputted into Step 6.

After initiating this process, BEMT-based loop conducts automated computations to analyze the hydrodynamic performance of the turbine. For the purposes of this analysis, each turbine blade is segmented into 17 blade elements, with each element representing 0.05 of the blade's total length. Iterative methods are employed to ascertain the values of a and a' for each blade element, which are crucial for determining the load exerted on the foil. Initially, both a and a' are set to zero to establish a starting point. Following this, $\lambda_{equivalent}$ is computed using Equation 4-2. This value is then integrated into Equation 2-3 to deduce the inflow angle (ϕ). Consequently, the angle of attack (a) is derived from Equation 2-4. With α in hand, the lift coefficient (C_L) and drag coefficient (C_D) for each foil segment can be determined. At this juncture, Re for each blade segment is individually computed, taking into account the local inflow velocity and the specific chord length

of that segment. The determined Re provides the basis to extract the corresponding C_L and C_D functions relative to the angle of attack. Subsequent to this, the tangential coefficient (C_t) and the normal coefficient (C_n) for every foil section are calculated using Equations 2-6 and 2-7, respectively. This allows for the computation of the chord solidity (σ_r) via Equation 2-8. With the known values of C_n and C_t, a and a' of the flow influencing the foil segment can be ascertained using Equations 2-9 and 2-10.

Subsequently, the updated values of a and a' are employed, replacing their prior iterations, prompting the calculation process to restart. It is important to note that, when determining the new a', TSR in Equation 2-2 should be substituted with $\lambda_{equivalent}$. The iteration process persists until the residuals of a and a' fall below a threshold of 0.01 in this study. Upon the conclusion of the iterative process, the derived results, including W, C_t and C_n, are utilized to assess the torque and thrust for each blade element using Equations 2-11 and 2-12. Following this, the aggregate thrust and power of the turbine are deduced through integration. Conclusively, the thrust coefficient and power coefficient are determined using Equations 2-13 and 2-14, respectively. The loads across all blade elements are then integrated, producing the turbine's comprehensive hydrodynamic performance.

With the turbine's specific hydrodynamic performance in hand, the system's ultimate power and energy yield can be computed. These procedures, thoroughly outlined in Section 4.2, are well-established and will not be reiterated here.

6.3.2 Numerical setup of CFD simulation

6.3.2.1 Numerical approach

The energy harvesting capability of the mechanism is verified using CFD simulations through the commercial software, STAR-CCM+. For these simulations, URANS model is paired with K-ω SST turbulence model. K-ω SST model integrates the benefits of K-ω and K-ε turbulence models by employing K-ω formulation in the boundary's inner regions and transitioning to K-ε formulation

in the free stream. As such, K-ω SST model proficiently provides solutions for adverse pressure gradients and flow separations (Menter, 1993). Furthermore, this model finds extensive application in submarine propulsion simulations (Sezen et al., 2021, Liu et al., 2021).

Within the simulation setup, a rotating domain encompasses the turbine, while the adjacent space is marked as a static domain. DFBI method is incorporated to capture UG hull's movement resulting from external forces, thereby estimating UG's translational and rotational velocities. Specifically, DFBI motion encompasses two degrees of freedom: the forward translational movement of the hull and its rotation around its central axis, depicted in Figure 6-4(a) and (b), respectively.

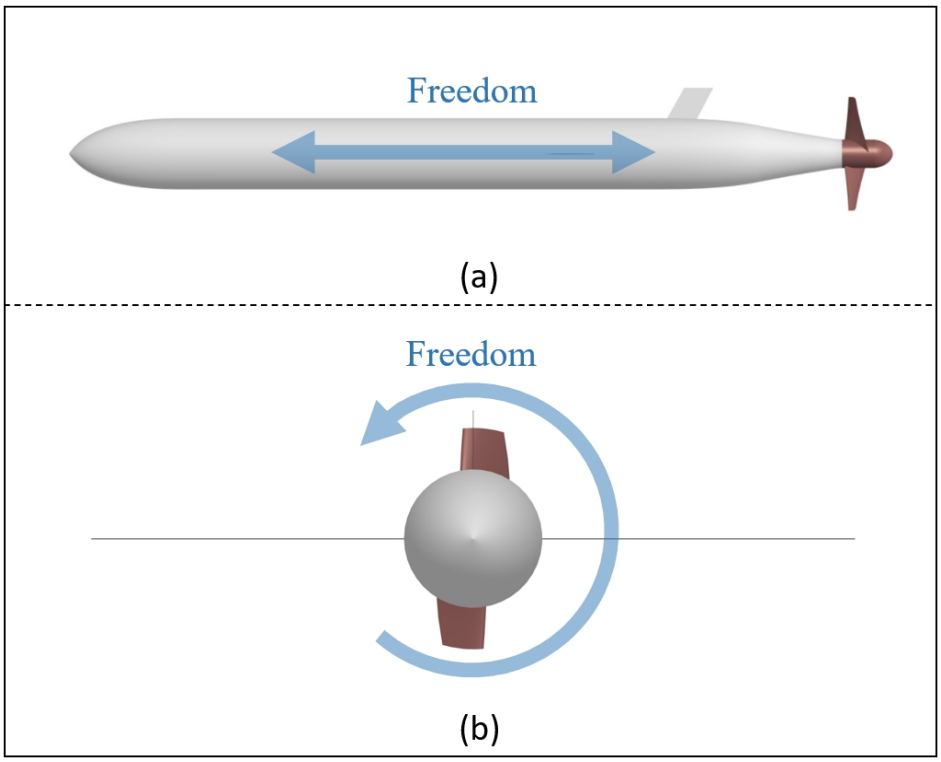

Figure 6-4. Two freedoms of the hull in DFBI simulation: (a) Translation along the forward direction; and (b) Rotation around the hull axis (roll)

DFBI technique incorporates B as the primary external force. As previously discussed, the entire system has the liberty to move in the forward direction. Consequently, under the influence of B, the system will proceed until it attains a certain velocity V_{DFBI}. At this velocity, a force equilibrium

is reached where B equates to the collective force from the turbine's thrust and the hull's resistance. Figure 6-5 represents the forces acting on the hull in the forward direction, as well as the velocity attained from DFBI simulation during this state of force balance.

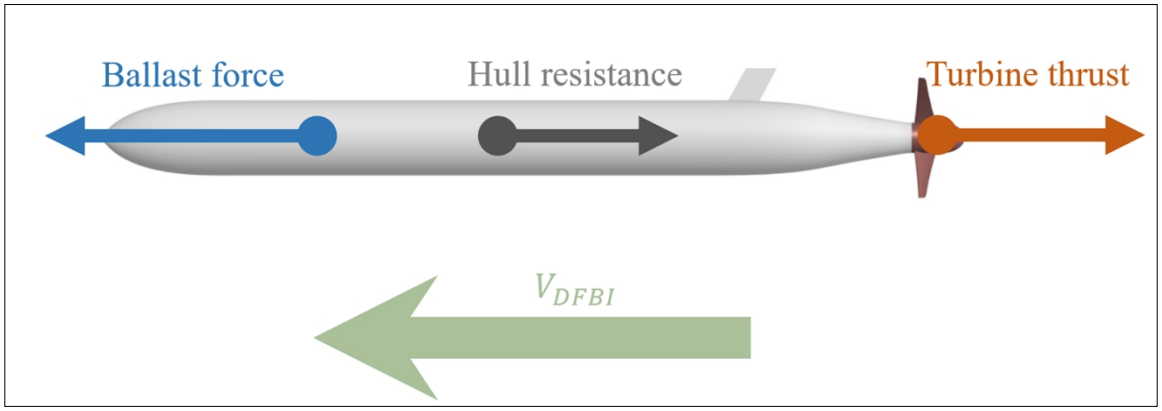

Figure 6-5. Analysis of hull forces and velocity in forward direction from DFBI simulation

In STAR-CCM+, using the superimposition motion technique, a sub-motion for the turbine is defined to follow UG's DFBI motion. Rigid Body Motion (RBM) method is employed to characterize the turbine's rotation and forecast its hydrodynamic performance in conjunction with the hull. The rotational velocity of the turbine is denoted by Ω_t. Simulations were run for a series of $\lambda_{operating}$ values, including 1, 1.5, 1.75, 2, 2.25, 2.5, and 3. Throughout the simulation, to preserve a consistent $\lambda_{operating}$, the turbine's rotational velocity (Ω_t) adjusted in real-time to the fluctuating forward velocity (V_{DFBI}) of the system, as dictated by DFBI solver. This relationship is formulated in Equation 6-2:

$$\Omega_t = \frac{V_{DFBI} * \lambda_{operating}}{R} \tag{6-2}$$

During its operation, the turbine creates rotational torque that powers the generator. This generator is rigidly attached to the hull, thus transferring the turbine's torque to the hull. As highlighted earlier, the hull has the capability to rotate freely around the same axis as the turbine. Therefore, under the turbine's torque influence, the hull rotates in the same direction. This rotation continues until it achieves a certain rotational velocity (Ω_h). At this point, a state of torque equilibrium is attained.

In this balanced state, the torque imparted onto the turbine by the fluid (Q) is equal in magnitude but opposite in direction to the torque imposed on the hull by the fluid (Q_h). Figure 6-6 illustrates the rotational speeds of both the turbine and the hull and provides an analysis of the torque equilibrium in DFBI simulation.

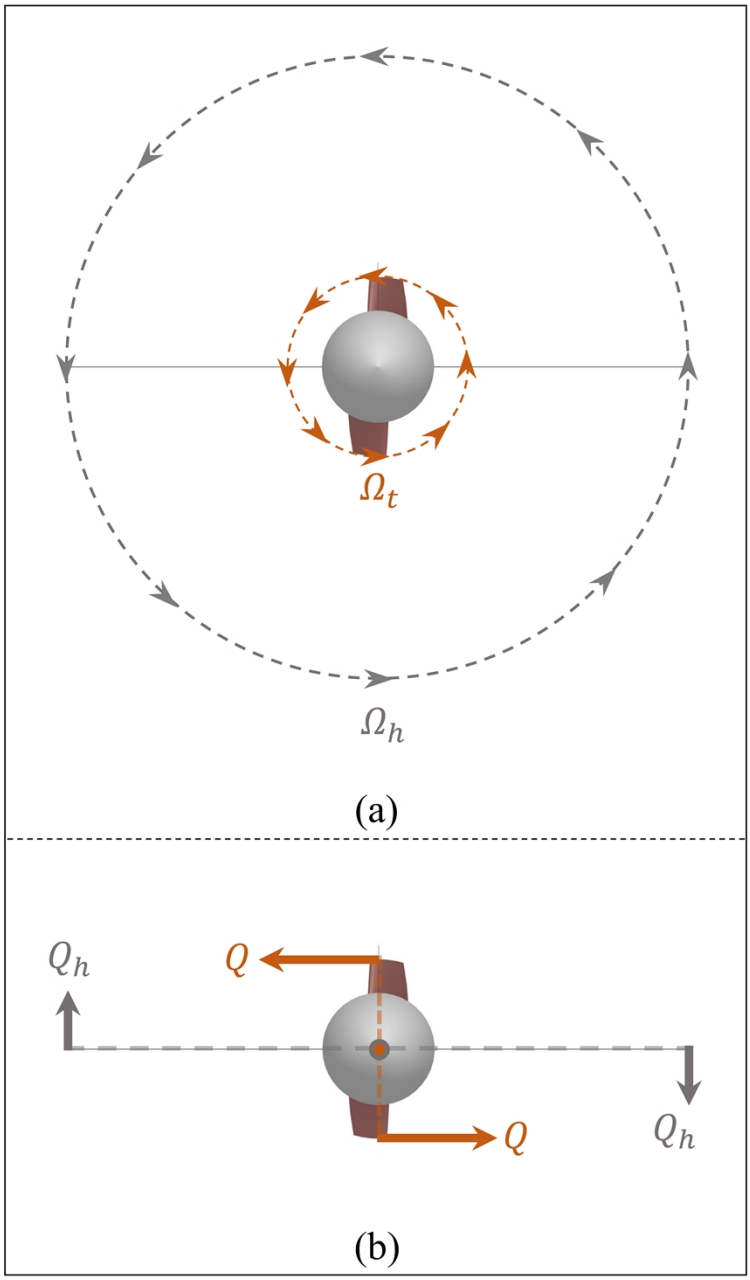

Figure 6-6. (a) Rotational velocity of hull and turbine; and (b) Torque balance in DFBI simulation

Concurrently, it is imperative to acknowledge that the rotation of the hull can influence the generator's power generation. This system harnesses electricity through a generator positioned inside the hull. The generator works on the electromagnetic induction principle, transforming mechanical energy into electric power. The generator is composed of two primary parts: the stator and the rotor. The stator is a stationary component featuring coils that encircle the generator. These coils, wound around an iron core, link to an external circuit. In contrast, the rotor is a rotating element attached to a shaft and has either permanent magnets or electromagnets, which are situated around its perimeter. These are connected to the outer circuit via slip rings and brushes. When the rotor spins, it generates a fluctuating magnetic field that, through electromagnetic induction, produces a current in the stator coils (Say et al., 1995).

Traditional wind turbines have a stationary stator, which is rigidly connected to a fixed bracket. In contrast, the stator in EHM rotates with the rotating hull at a speed of Ω_h. Given that the rotor, driven by the turbine, also rotates in the same direction at a speed of Ω_t, the relative rotational speed between the rotor and stator decreases. This relative rotation speed is the real effective rotation speed for the generator. It is represented by Ω_e and can be determined via Equation 6-3:

$$\Omega_e = \Omega_t - \Omega_h \tag{6-3}$$

The power of EHM in DFBI simulation (P_{DFBI}) can be expressed as follows:

$$P_{DFBI} = \Omega_e * Q \tag{6-4}$$

Considering that a complete dive and ascend cycle of UG covers a distance of 2000 m, the computational cost required for a CFD simulation is prohibitively expensive. To calculate the final E_y, the stabilized P_{DFBI} in the simulation is multiplied by the duration of one cycle. Therefore, Equation 6-5 is employed to calculate the amount of E_y for one cycle.

$$E_y = \frac{P_{DFBI} * d_w * 2}{V_{DFBI}} \tag{6-5}$$

where d_w is the working depth.

With E_y in Equation 6-5, the hydrodynamic energy conversion efficiency (η_h) at each $\lambda_{operating}$ can be calculated through Equation 4-11.

The time-step ensures that the turbine rotates approximately 1.5 degrees per time-step, adhering to the recommendations of ITTC, which suggests a time-step between 0.5 degrees and 2 degrees (Stark et al., 2021).

6.3.2.2 Computational domain and mesh generation

As illustrated in Figure 6-7, a rectangular computational domain was chosen to analyze the flow around UG hull. The length of UG is defined as L_h. The inlet boundary is defined as a velocity inlet 4L upstream from the hull, while the outlet boundary is set as a pressure outlet 10 L downstream from the hull. The surrounding boundaries are designated as symmetry planes, positioned 3L away from the hull. Both the hull and the turbine are considered no-slip walls. The rotating domain was incorporated into the simulation to emulate the turbine's rotation, and it is separated from the surrounding volume of the static region by an interface. The selected domain dimensions are consistent with ITTC recommendations (ITTC, 2011).

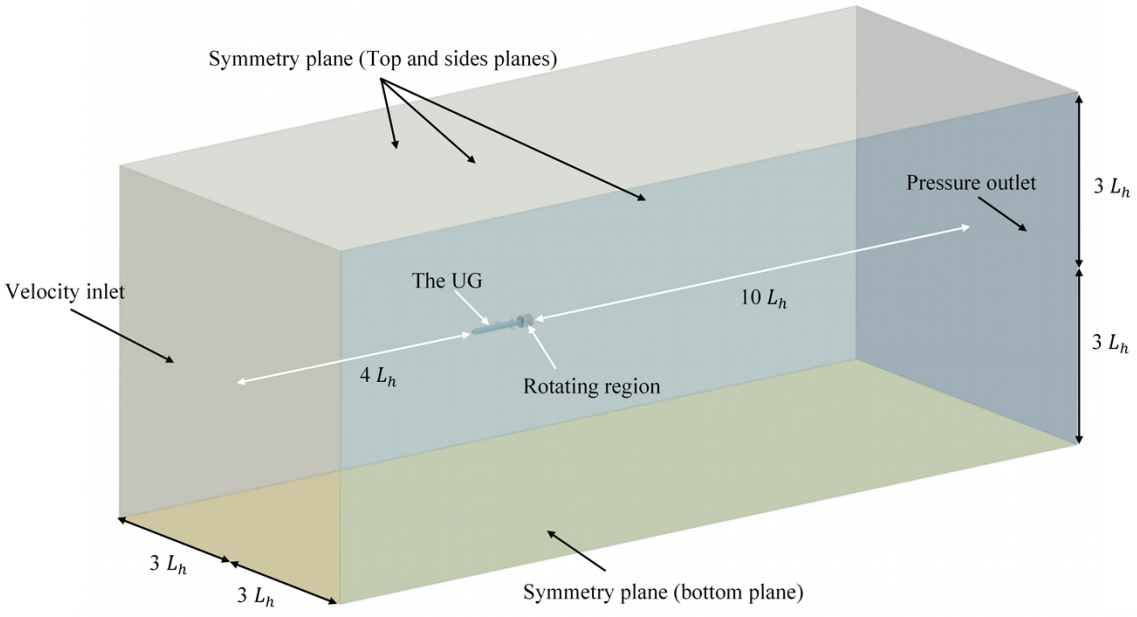

Figure 6-7. Domain and boundary condition of the simulation

The region-based automatic meshing tool, equipped with volumetric controls, was employed to generate a mesh comprising approximately 9.7 million cells. A polyhedral mesh was employed for the simulation domain, which has been proved accurate in predicting the experimental result in self-propulsion CFD simulations of submarines (Takahashi et al., 2019). The boundary layer is solved using prism layers. All y + wall treatment was used, ensuring the average y + remained below 1.

The space between the turbine and the hull is refined to capture the hydrodynamic interactions between them. The spaces in the vicinity of the turbine, especially in the downstream direction, receive additional refinement to ensure detailed capture of the flow around the turbine as well as the wake structure trailing it. The cell structure around UG hull and the turbine is displayed in Figure 6-8.

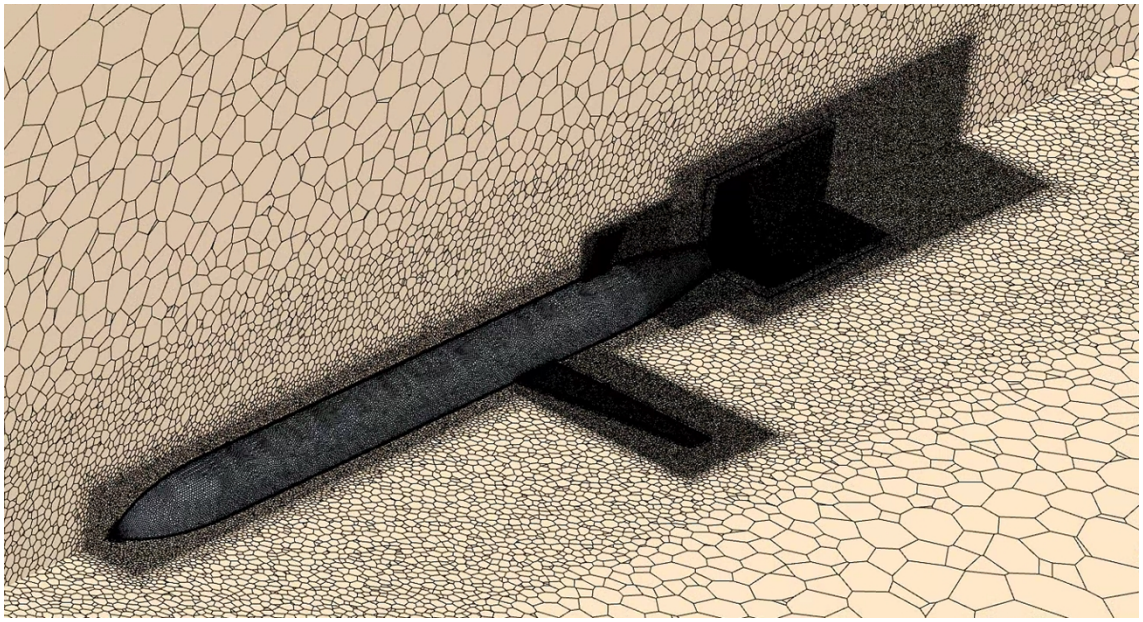

Figure 6-8. Cell structure around the hull and turbine

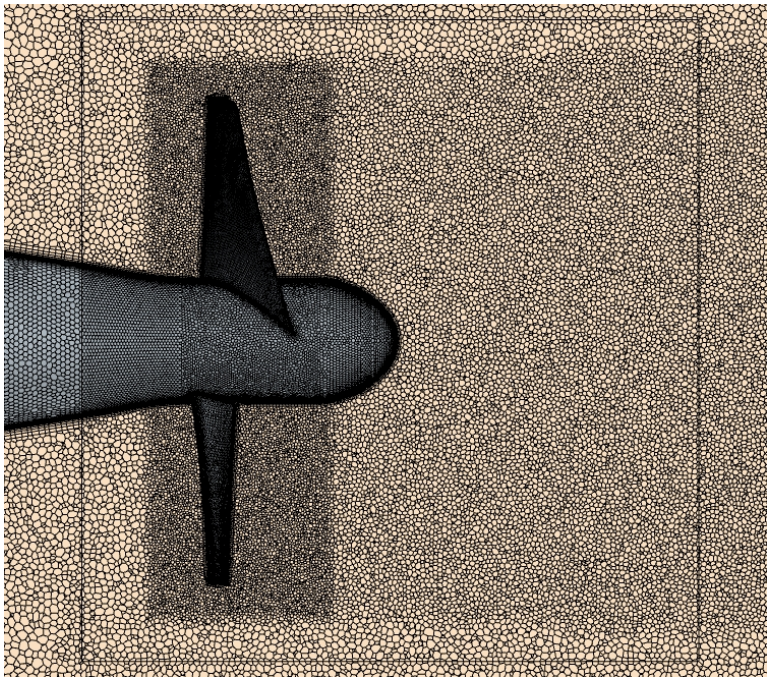

Figure 6-9. Cell structure near the rotation region

The surface meshes of the hull and the turbine are shown in Figure 6-10.

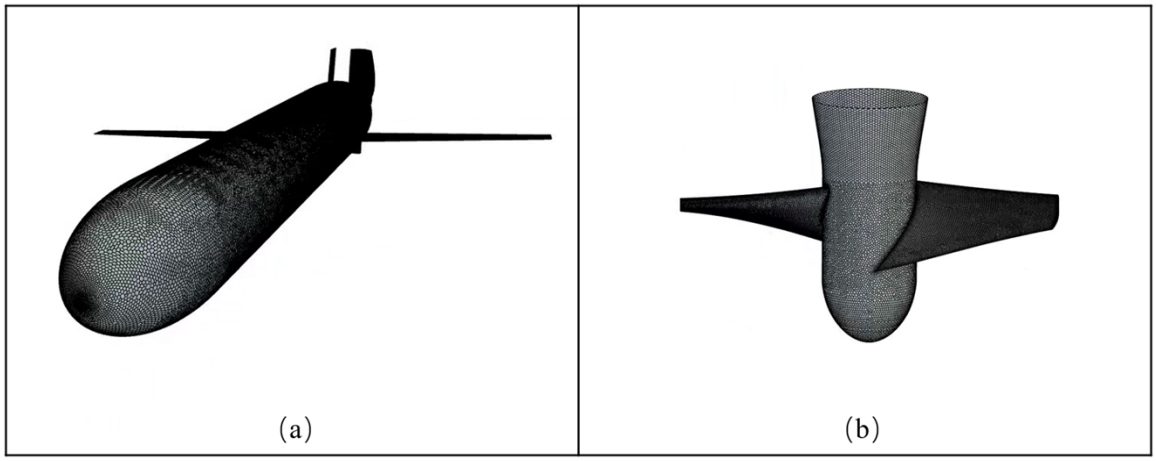

Figure 6-10. Surface mesh: (a) Hull; and (b) Turbine

6.3.2.3 Grid convergence analysis

A verification study was conducted to assess the uncertainty of CFD simulations using Grid Convergence Index (GCI) technique, originally proposed by Roache (Roache, 1998) and based on Richardson (Richardson, 1911). The comprehensive methodology implemented in this study was

developed by Celik (Celik et al., 2008). ITTC also endorses this method as a means to compute the numerical error of a solution. In this study, E_y and P were chosen as the integral variables at $\lambda_{operating} = 2$. At this operating condition, the maximum E_y is achieved among all tested $\lambda_{operating}$ in the simulation. The study uses three different mesh cell counts: coarse, medium, and fine, with the meshes comprising 2.5, 5.1, and 9.7 million cells, respectively.

Table 6-2: Uncertainty analysis of E_y

	φ_1	φ_2	φ_3	$N_1^{'}$	$N_2^{'}$	$N_3^{'}$	$R^{'}$	$\%\mathrm{GCI}_{\mathrm{FINE}}^{21}$
E_y	22.7	22.5	22.2	9.7 M	5.1 M	2.5 M	0.43	0.79%
p	20	19.9	19.7	9.7 M	5.1 M	2.5 M	0.5	0.81%

The tabulated uncertainty results for E_y (kJ) and P (W) are shown in Table 6-2. φ_1, φ_2, and φ_3 represent the result of fine, medium, and coarse mesh grids, respectively. $N_1^{'}$, $N_2^{'}$, and $N_3^{'}$ represent the grid number of fine, medium, and coarse mesh grids. The difference between the solution scalars ε_{21} (ε), including and ε_{32} can be calculated through Equations 6-6 and 6-7:

$$\varepsilon_{21} = \varphi_2 - \varphi_1 \tag{6-6}$$

$$\varepsilon_{32} = \varphi_3 - \varphi_2 \tag{6-7}$$

With ε_{21} and ε_{32}, the ratio of solution scalars, which is used to determine the convergent condition, can be obtained via Equation 6-8:

$$R^{'} = \frac{\varepsilon_{21}}{\varepsilon_{32}} \tag{6-8}$$

By using the ratio of solution scalars, the solution type can be determined. There are four solution types: $0 < R^{'} < 1$ represents the monotonic convergence; $-1 < R^{'} < 0$ represents the oscillatory convergence; $R^{'} < -1$ represents the oscillatory divergence; and $R^{'} > 1$ represents the monotonic divergence. Subsequently, GCI index can be determined through Equation 6-9:

$$\%\mathrm{GCI}_{\mathrm{FINE}}^{21} = \frac{1.25 e_a^{21}}{r_{21}^{p} - 1} \tag{6-9}$$

where e_a is the approximate relative error and p is the apparent order. More detailed information for the uncertainty assessment can be found in Celik's research (Celik et al., 2008).

As depicted in Table 6-2, the convergence conditions ($R^{'}$) for E_y and p are 0.43 and 0.5, respectively, indicating that the simulation exhibits monotonic convergence. The uncertainty errors for E_y and p are 0.79% and 0.81%, respectively. Consequently, based on the uncertainty assessment at $\lambda_{operating} = 2$, the fine mesh consisting of approximately 9.7 million cells was chosen.

6.3.2.4 DFBI simulation results and discussion

Simulations were completed under different values of $\lambda_{operating}$. Figure 6-11 shows the typical velocity contour of the operating system during simulation.

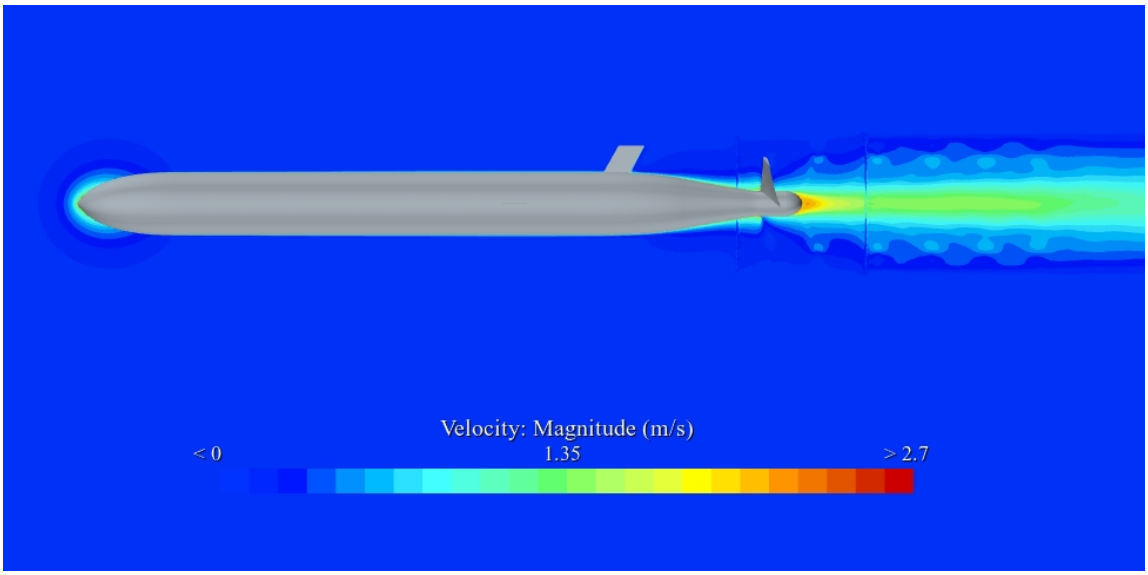

Figure 6-11. Typical velocity contour of the operating system ($\lambda_{operating} = 2$)

Figure 6-12 shows the comparison between P (in W) derived from the mathematical model and P from CFD simulation. A satisfactory agreement is observed, typically with a difference of around 10%. This alignment is particularly prominent under the working conditions of primary interest in this study, where $\lambda_{operating}$ is approximately 2. The mathematical model predicts a

maximum power output of 20.3 W at $\lambda_{operating}$ of 2.5, while CFD simulation estimates the highest power output to be 20 W at $\lambda_{operating}$ of 2.

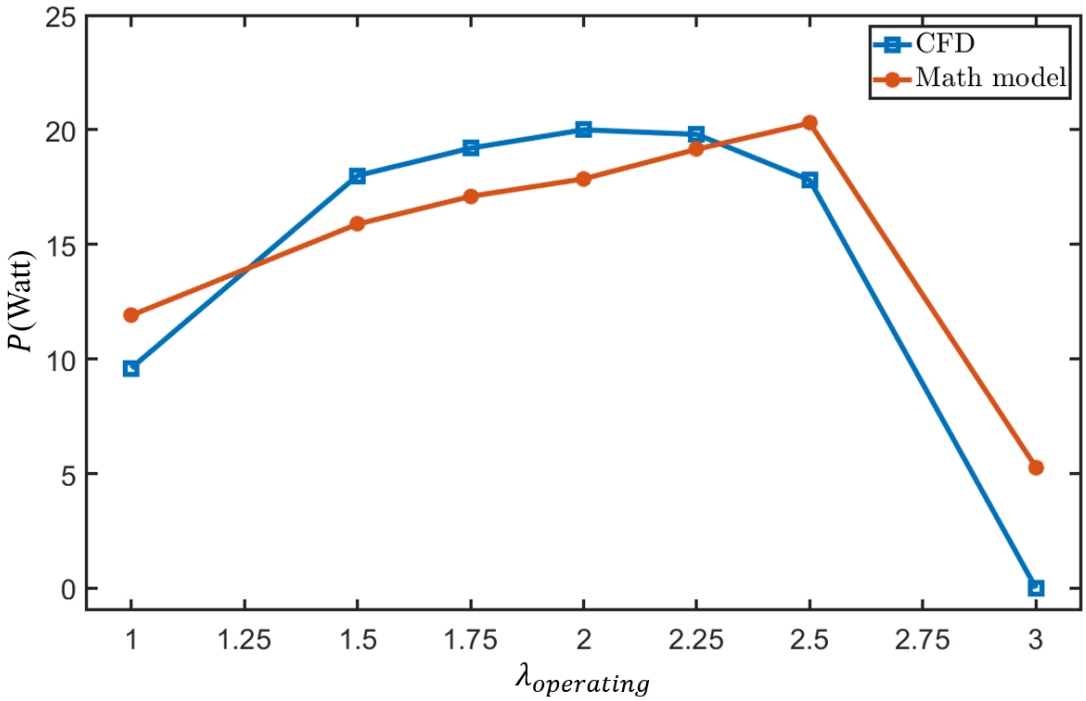

Figure 6-12. Comparison of P in the mathematical model Vs CFD simulation at different $\lambda_{operating}$

E_y from DFBI simulation at different $\lambda_{operating}$ is displayed in Figure 6-13, along with E_y from the mathematical model. An acceptable agreement between the two is achieved. When evaluating the simulation results of E_y at different TSRs, the primary focus of this thesis is on the highest value among all $\lambda_{operating}$, since this peak value best represents the energy harvesting capability of the system. As illustrated in Figure 6-13, the mathematical model predicts a peak E_y of 26.4 kJ for the system when $\lambda_{operating} = 2.25$. In contrast, CFD simulation shows that the system's E_y can reach a maximum of 22.7 kJ when $\lambda_{operating} = 2$. Therefore, the mathematical model overestimates E_y by 16.2%.

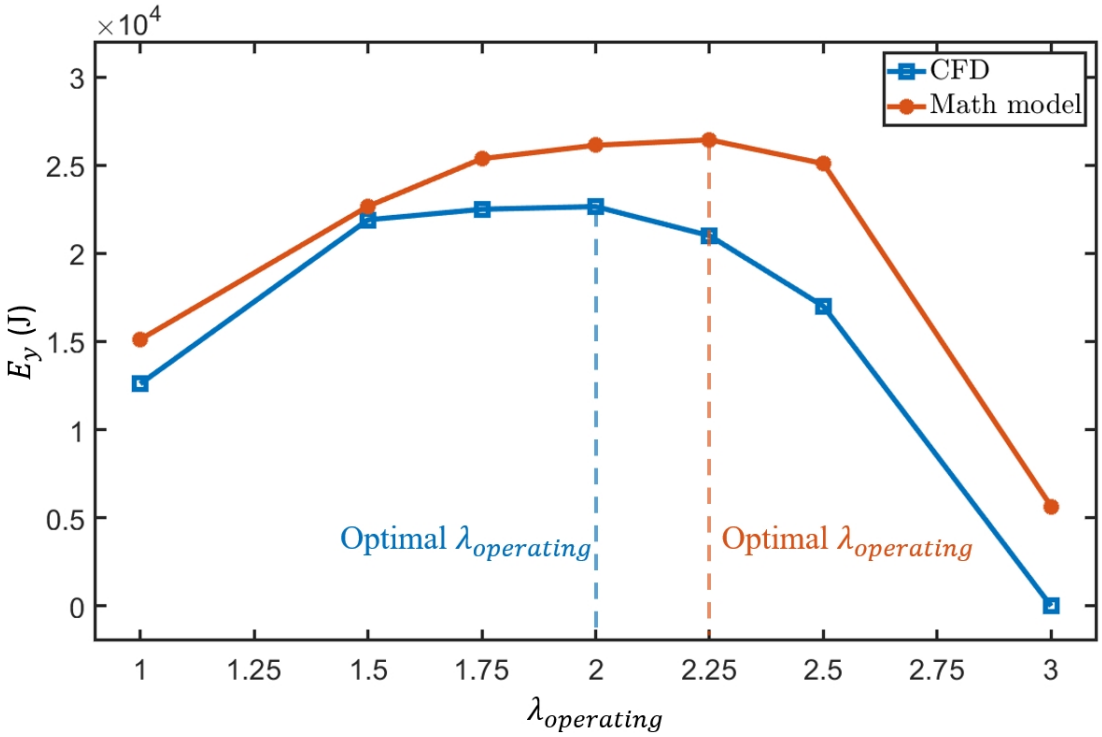

Figure 6-13. Comparison of E_y in the mathematical model Vs CFD simulation at different $\lambda_{operating}$

This discrepancy primarily arises from the idealizations inherent in the mathematical model. A significant assumption in the mathematical model is the overlooking of hydrodynamic interactions between the hull and the turbine. In reality, these interactions not only influence the wake velocity behind the hull but also modify the wake distribution. Unlike the mathematical model, CFD captures this hydrodynamic interaction between the hull and the turbine with great precision, providing an accurate representation of its impact on E_y. Figure 6-14 showcases the axial velocity contours in the wake of both the bare hull and the integrated system, positioned 5 cm upstream from the turbine. Concurrently, Figure 6-15 depicts the absolute pressure contours under the same conditions and location. Both figures vividly underscore the substantial effects of the hydrodynamic interactions between the hull and the turbine on the flow characteristics in that region.

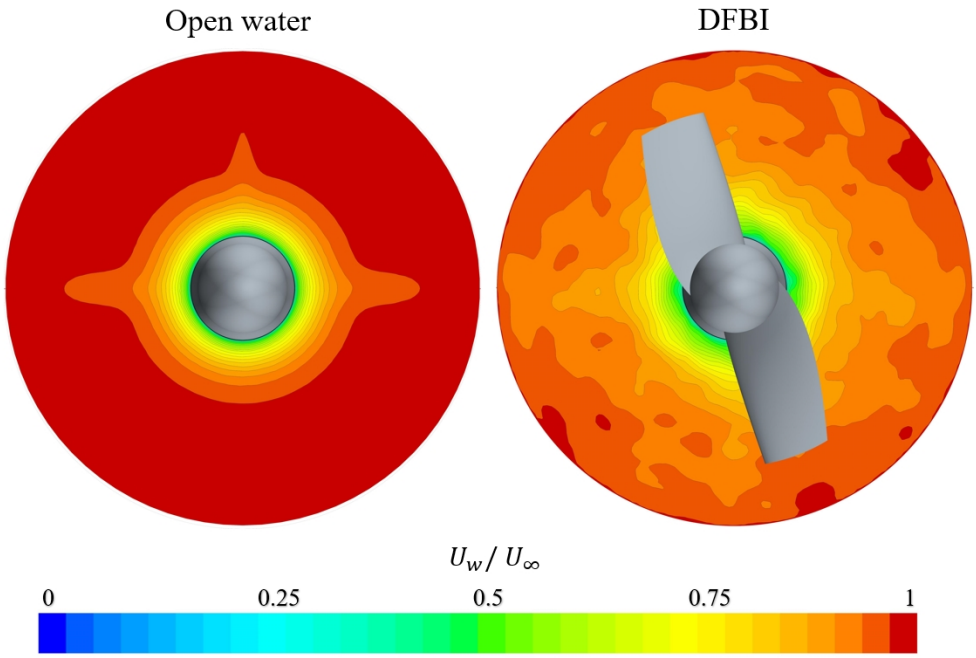

Figure 6-14. Contours of axial velocity in the wake of bare hull and the whole system (5 cm upstream from turbine)

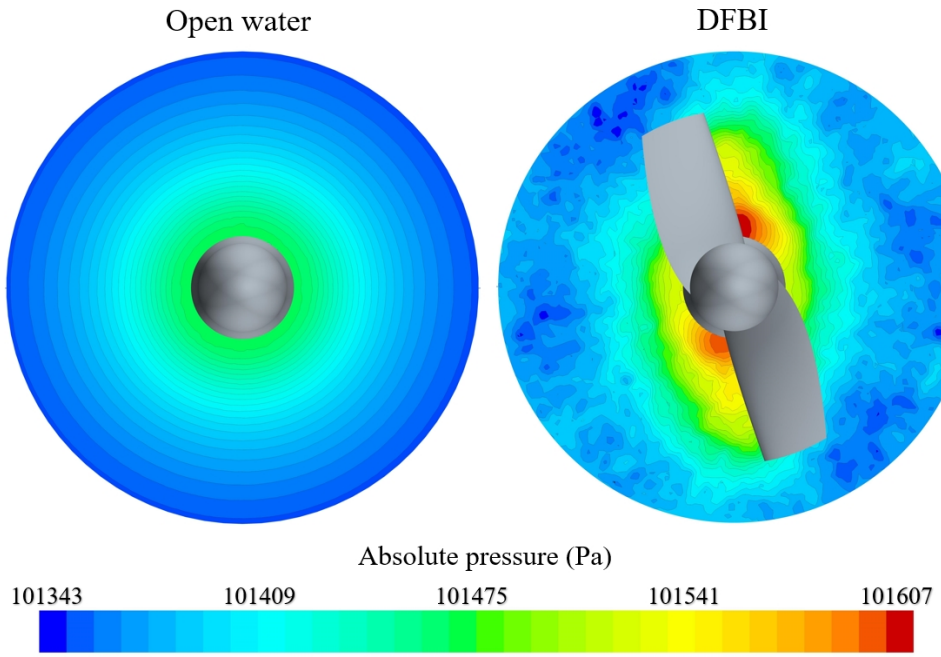

Figure 6-15. Contours of absolute pressure of bare hull and the whole system (5 cm upstream from turbine)

By comparing the drag coefficient of the bare hull ($C_{T_h}{}^b$) and the drag coefficient of the hull subjected to hydrodynamic interaction in DFBI ($C_{T_h}{}^i$), the influence of hydrodynamic interaction can be intuitively understood. The expression for C_{T_h} is given by Equation 6-10.

$$C_{T_h} = \frac{R_h}{0.5 * \rho * V^2 * S} \tag{6-10}$$

where R_h is the hull resistance; ρ is water density; V is the velocity; and S is the wet surface of the hull.

$C_{T_h}{}^b$ and $C_{T_h}{}^i$ at different $\lambda_{operating}$ are presented in Figure 6-16. Hydrodynamic interaction exhibits a significant impact on C_{T_h} of the hull. Generally, $C_{T_h}{}^i$ is lower than $C_{T_h}{}^b$ by approximately 25%.

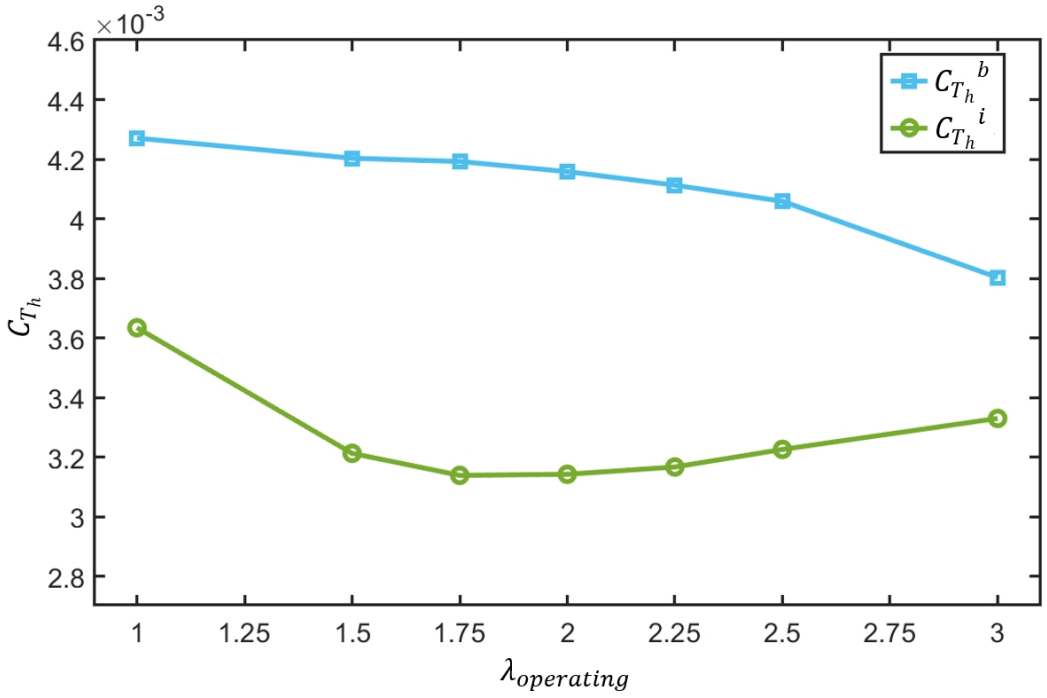

Figure 6-16. $C_{T_h}{}^b$ and $C_{T_h}{}^i$ at different $\lambda_{operating}$

Another simplification in the mathematical model is the omission of the hull's rotational velocity around its own axis (Ω_h). In contrast, DFBI solver in CFD can accurately simulate this rotation and its effects. The presence of Ω_h not only reduces Ω_e but also cause energy consumption during the hull's rotation. Furthermore, it affects both the velocity and distribution of the wake. These

three factors lead to a reduction in the overall energy yield of the system. Figure 6-17 presents DFBI simulation results for Ω_h (in degrees) at different $\lambda_{operating}$ values.

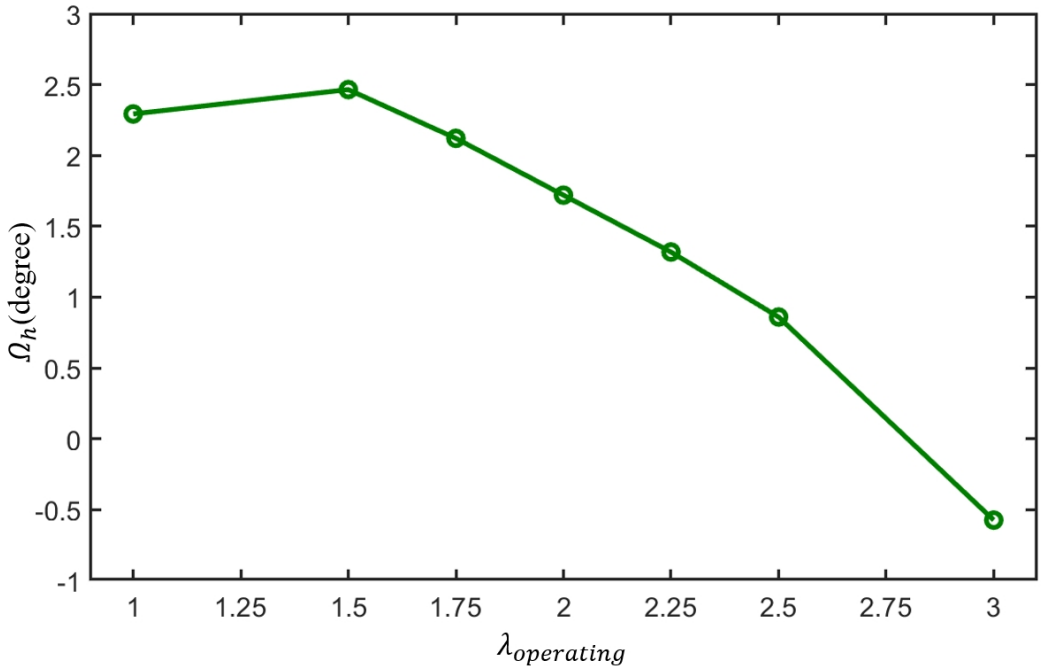

Figure 6-17. DFBI simulation results for Ω_h at different $\lambda_{operating}$

Furthermore, the mathematical model is grounded in BEMT, which carries several idealizations as discussed in Section 2.4.2. These simplifications can influence the precision of the turbine performance analysis. This has been quantified in Section 4.2 and will not be reiterated here.

The focus of this chapter is energy harvesting capability of the mechanism, as determined by DFBI simulation. As mentioned above, the simulation shows that E_y can reach peak at 22.7 kJ. Considering that a typical Thermal UG requires approximately 6 kJ of energy for each descent-ascent cycle in gliding mode (Davis et al., 2002, Falcão et al., 2018), this result confirms the feasibility of applying this EHM into UG, achieving a theoretical unlimited range. However, the energy yield in this study is based on the hydrodynamic forces, excluding the efficiency of the generator and system transmission losses.

Additionally, the data suggests that this EHM could harness PCM more effectively for electricity generation compared to conventional OTEC-PCM. Specifically, it can produce 22.7 kJ of electricity using just 9.7 kg of PCM, equating to 2.34 kJ of electricity per kilogram of PCM. This is a stark contrast to traditional OTEC-PCMs which generate significantly less electricity per kilogram of PCM, as detailed in Table 6-3.

Table 6-3: Energy yield per kilogram of PCM of different OTEC-PCM

System	kJ / kg of PCM
OTEC-PCM (Tianjin University)	1.12
Slocum-TREC glider(Clark)	0.648
SOLO-TREC	0.612

While this EHM has the potential to outperform the power generation capabilities of current OTEC-PCM systems, it offers an avenue for developing an auxiliary propeller for UG. Such an addition would notably enhance the mission capabilities of UG, as outlined in Section 2.2.2. Therefore, it can be inferred that EHM explored in this study stands as a formidable competitor to conventional OTEC-PCM.

However, it is imperative to note certain caveats in this comparison. The energy yield computed in this study is derived solely from hydrodynamic forces, sidelining other pivotal factors. For instance, the efficiency of the generator, which typically ranges between 60% and 90%, is not considered.

Moreover, the system's transmission losses have not been accounted for. During the conversion from thermal to hydraulic energy, the primary transmission loss stems from the hydraulic energy dissipated between heat transfer and the accumulator. This loss predominantly arises from the friction between the piston and the interior of the hydraulic cylinder. Likewise, in the transition from hydraulic energy to the system's ballast force, the primary energy drain lies in the hydraulic exchange between the accumulator and the outer bladder, mainly due to friction between the piston and the cylinder wall. While hydraulic energy losses are contingent on the specifics of the hydraulic

system's design, a definitive efficiency cannot be pinpointed until a working prototype is available. However, in general terms, the efficiency of a hydraulic cylinder can achieve 85% to 95%. Furthermore, unlike traditional OTEC-PCM, UG's EHM mandates a halt in cruising during energy harvesting mode. Even though UG does not cruise incessantly, this stipulation could introduce challenges in planning and might, to a degree, impinge on the overall efficiency.

6.4 Conclusion

This chapter integrates the force-to-velocity turbine design philosophy outlined in Chapter 4 with the design method based on the expansion of the actuator disc theory presented in Chapter 5. The aim is to conceptualize an optimally efficient turbine. This turbine was employed to assess the energy harvesting capability of the proposed EHM in this thesis:

1. To validate the energy harvesting capability of the mechanism with high precision, a DFBI simulation of the entire system was conducted using CFD software.

2. CFD results demonstrate that the power (P) can reach 20 W, and the energy yield (E_y) of EHM can achieve 22.7 kJ per descent and ascent cycle.

3. CFD simulation shows that the mathematical model tends to overestimate E_y by approximately 16.2%. This discrepancy primarily results from the idealizations within the mathematical model, particularly the neglect of hydrodynamic interaction between the hull and turbine.

4. CFD analyses validate that the energy yield of EHM per descent-ascent cycle in energy harvesting mode significantly exceeds the energy consumption of a typical Thermal UG per descent-ascent cycle in gliding mode. This affirms that, in theory, endlessly operational UG is achievable, if the component lifespan within the system is disregarded.

5. In this EHM, each kilogram of PCM can generate 2.34 kJ of electricity. This suggests its potential to surpass the power generation capacity of existing OTEC-PCM.

6. Consequently, without compromising on E_y, EHM obtains the potential to work as a propeller, significantly expanding the mission capability of UG. This underlines the prospective competitiveness of EHM against other prevailing OTEC-PCM systems.

7 Conclusions and recommendations for future research

7.1 Introduction

Section 7.1 of this thesis serves as an introduction. This is followed by Section 7.2, which presents a comprehensive overview of the thesis. Section 7.3 synthesizes the key findings and conclusions derived from the research, and Section 7.4 furnishes recommendations for subsequent research in the domain.

7.2 Overall review of the thesis and contributions to the state-of-the-art

There is a growing consensus around the pivotal role oceans will assume in the imminent global economy. As such, ocean monitoring by UGs is paramount for deepening our comprehension of marine dynamics and the vast potential resources they conceal. To mitigate energy constraints faced by UGs, numerous devices dedicated to harnessing ocean thermal energy have emerged since the turn of the century. Among these innovations, a pioneering turbine-based EHM promises to significantly elevate the efficiency of UGs, if successfully materialized. This mechanism possesses the capacity to not only augment the operational scope of UGs but also fortify their reliability and resilience. However, prevailing technological impediments have stymied the evolution and maturation of this concept.

To enhance the effectiveness of NASA's turbine-based EHM, this doctoral study has provided unique and valuable perspectives on the turbine used within the EHM system. The research sheds light on two primary aspects: understanding the turbine's operating mechanism and proposing an innovative design approach for it. To realize these objectives, the inaugural phase involved a meticulous dissection of the turbine's mechanism and its foundational design principles. Subsequently, a pioneering turbine design methodology was articulated and put to the test. The juxtaposition of outcomes from both the mathematical model and CFD simulations have fortified

the assertion that EHM—equipped with a turbine sculpted by this research's findings—holds promising prospects for tangible deployment in forthcoming technological iterations.

As outlined in Chapter 1, this research delineated five primary objectives, which have been successfully addressed in the subsequent chapters.

Objective 1: Conduct a comprehensive literature review on the state-of-the-art design and optimization of turbines within EHM. This will facilitate a deeper comprehension of prevailing research topics, highlighting areas However uncharted, thus marking knowledge gaps this study aims to bridge. A strategic research methodology tailored to actualize the study's goals is also proposed.

Objective 2: Propose a more feasible energy harvesting mode for the mechanism, according to the practical engineering constraints.

Objective 3: Design and optimize the turbine within EHM based on BEMT. This entails constructing a mathematical model for the mechanism and rigorously analyzing a plethora of turbine designs to decode the inherent design philosophy and operational tenets of the turbine.

Objective 4: Explain the phenomena observed in *#Objective 3* at a mathematical level. This involves deepening the grasp on the turbine's functionality within EHM by recalibrating and broadening the actuator disk theory, one of BEMT's foundational pillars. Based on this improved comprehension and the expanded actuator disk theory, a new BEMT-based design method is forged, tailored to the turbine operating under this unique working principle.

Objective 5: Verify the energy harvesting capability of the mechanism when equipped with a turbine designed based on the findings in *#Objectives 3* and *4* through CFD simulation.

To accomplish the aforementioned objectives, a comprehensive literature review was executed. This served as a cornerstone for the empirical analysis and mathematical derivations articulated in the core segments of this study, all underpinned by state-of-the-art literature numerical methodologies.

In Chapter 2, the study embarks on a comprehensive literature review, delving into state-of-the-art research concerning the ocean thermal EHM utilized in UGs. This encompasses the thermal buoyancy engines, the turbine, and the most recent research methodologies. Notably, Chapter 2 underscores the scant research concerning the turbine in NASA's turbine-based EHM, pinpointing significant gaps that warrant further exploration. Hence, a call for deeper investigation into the turbine's operation and its efficient design is emphasized. Furthermore, Chapter 2 also demarcates the most fitting research methodology for steering this study, fulfilling *#Objective 1*.

Chapter 3 introduces a new energy harvesting mode for EHM, aligning with real-world design parameters of standard UG. In this revamped mode, the thermal buoyancy engines propel UG vertically through oceanic waters by generating ballast force while simultaneously spinning the aft-located turbine to harness energy from the fluid. Additionally, NASA EHM's traditional method of transforming thermal energy to hydraulic energy undergoes a modification. This avant-garde energy harvesting mode amplifies EHM's viability, achieving *#Objective 2*.

Chapter 4 delves deep into understanding the turbine's design philosophy. A mathematical model anchored in BEMT is formulated for a holistic design analysis. Catering to the turbine's distinct operational conditions, a refined BEMT model is embedded within this mathematical framework. Comprehensive design analyses yield insights into the turbine's design philosophy, notably the optimal mix of parameters for the turbine, design TSR selection, and radius determination. The model illuminates divergences from traditional turbine design principles, realizing *#Objective 3*.

In Chapter 5, the study deepens the grasp on the turbine's operational dynamics, prompting the rederivation and expansion of the Actuator Disk Theory. This expanded theory clarifies the nexus

between axial induction factor, power, and energy yield of force-to-velocity turbines. Rooted in these revelations, a fresh BEMT-centric design methodology tailored for force-to-velocity turbines is introduced. A subsequent case study validates this method, indicating its efficacy in pinpointing optimal turbine designs, culminating in the achievement of *#Objective 4*.

Chapter 6, through high-fidelity CFD simulations, validates EHM's energy harvesting prowess. Using a conventional UG hull, and a turbine optimized through prior revelations, a DFBI simulation of EHM is undertaken employing STAR CCM+. CFD results not only paint a picture of a theoretically self-sustaining UG but also indicate EHM's potential to rival existing OTEC-PCM systems, marking the accomplishment of *#Objective 5*.

Apart from the research presented in this thesis, several parts of the research in various reputable journals and international conferences. The list of publications is provided below:

Thesis related publications:

1. HOU, H., ARREDONDO GALEANA, A., SONG, Y., XU, G., XU, Y. & SHI, W. 2023. Design of a novel energy harvesting mechanism for underwater gliders using thermal buoyancy engines. Ocean Engineering, 278, 114310.
2. HOU, H., SHI, W., XU, Y. & SONG, Y. 2023. Actuator disk theory and blade element momentum theory for the force-driven turbine. Ocean Engineering, 285, 115488.
3. HOU, H., SHI, W., GALEANA, A. A. & SONG, Y. A Novel Energy Harvesting Mechanism and Its Design Methodology for Underwater Gliders Using Thermal Buoyancy Engines. The 32nd International Ocean and Polar Engineering Conference, 2022. ISOPE-I-22-067.

Additional publications during PhD

1. HOU, H., KRAJEWSKI, M., ILTER, Y. K., DAY, S., ATLAR, M. & SHI, W. 2020. An experimental investigation of the impact of retrofitting an underwater stern foil on the resistance and motion. Ocean Engineering, 205, 107290.

Additionally, the new-type buoyancy engine proposed in Chapter 3 has been filed for a patent, with the author of this thesis listed as a co-inventor.

Patents during PhD

1. SHI, W., HOU, H., XU, Y. & MEHMET, A. 2022. A new thermal buoyancy engine and its control method. GB2010890.8

7.3 Primary conclusion

Refining the aforementioned conclusions and summaries of each chapter, the primary conclusions of this thesis are as follows:

1. This study investigates and enhances the feasibility of EHM. It contributes original and valuable insights to the latest research on the turbine of the turbine-based EHM. Furthermore, the study lays the necessary technical foundation for the implementation of EHM.

2. Comprehensive analyses through the mathematical model offers a profound understanding of the turbine's design philosophy. This understanding encompasses the optimal combination of C_p and C_t for the turbine, the choice of design TSR, the selection of the turbine's radius. These design philosophies can be used as a guideline for designing an optimal turbine design for this EHM.

3. The turbine in this study fundamentally operates as a force-to-velocity turbine. To adapt the actuator disc theory and its corresponding BEMT-based design method to this type of turbine, this study expanded the actuator disk theory. According to the expanded actuator disk theory, $a = 1/3$ no longer leads to highest P or E_y for the force-to-velocity turbine. Therefore, Betz's actuator disc theory, tailored for traditional turbine design, is not directly applicable to force-to-velocity turbines.

4. Theoretical upper bounds for the energy conversion efficiency and power have been identified for the force-to-velocity turbine, providing guidance for its design.

5. Following the expansion of the actuator disc theory, the power P is a function of B, ρ, R, r, C_d, and a, while E_y is a function of B, L, R, r, C_d, and a.

6. A new BEMT-based design method has been formulated for the preliminary design of force-to-velocity turbines. The method can design the turbine according to the design targets, including designing the turbine with the highest E_y or designing the turbine with the highest P.

7. A DFBI simulation using CFD software validated EHM's capabilities, achieving 20 W of power and 22.7 kJ energy yield per descent-ascent cycle. CFD simulation revealed that the mathematical model overestimates the energy yield by 16.2%, primarily due to idealizations and neglecting hydrodynamic interactions. Despite this, the energy yield significantly exceeds a typical Thermal UG's consumption. This suggesting that, in theory, a self-sustaining UG with endless operational capacity is achievable if component lifespan is not considered.

7.4 Recommendations for future research

The research presented in this thesis sets a foundation for deepening our understanding and optimization of EHM. While significant strides have been made within the constraints of time and resources, the following recommendations are proposed for future research in this domain:

- The new-type thermal buoyancy engines require the development of a prototype to determine the achievable ballast force, particularly the ballast force per kilogram of PCM. Based on this, the final sea trials should be conducted to verify most of the conclusions of this thesis.

- The potential of expanding this EHM to serve as an auxiliary propeller should be evaluated. As previously mentioned, by adjusting the pitch and rotation of the designed turbine, it could potentially offer propulsive capabilities, thus broadening the operational range of UGs. While this capability is not the primary focus of the current research, it emerges as a vital avenue for future exploration.

- An assessment of the entire system's economic cost is paramount. The overarching aim is to engineer a product that stands toe-to-toe with existing offerings in the market. A comprehensive evaluation entails both technical and economic considerations. While this research has delved into the technical aspects, an in-depth economic analysis remains to be conducted. This will be pivotal in gauging the mechanism's market viability.

- The impact of using various foils in EHM warrants investigation. While this study consistently utilized the NACA 0015 foil for the turbine, no comparative analysis has been done on the effects of different foils on power and energy harvesting. Future research should investigate the potential increase in power and energy yield by varying the foil type, as it might offer a straightforward approach to enhance the performance of EHM.

References

A. Amiri, H., Shafaghat, R., Alamian, R., Taheri, S. M. and Safdari Shadloo, M. (2020). Study of horizontal axis tidal turbine performance and investigation on the optimum fixed pitch angle using CFD: A case study of Iran. *International Journal of Numerical Methods for Heat and Fluid Flow*, 30(1), pp.206-227.

Abad, G., Lopez, J., Rodriguez, M., Marroyo, L. and Iwanski, G. (2011). *Doubly fed induction machine: modeling and control for wind energy generation.* New York: John Wiley and Sons.

Ahmed, U., Apsley, D. D., Afgan, I., Stallard, T. and Stansby, P. K. (2017). Fluctuating loads on a tidal turbine due to velocity shear and turbulence: Comparison of CFD with field data. *Renewable Energy*, 112, pp.235-246.

Aliexpress. (2022). *Oil Bladder* [online]. Available from: https://www.aliexpress.com/item/32934563620.html [Accessed 12 August 2023].

Amazon. (2023). *Dancing Wings Hobby Metal EVP Electric Variable Pitch System for RC EPO EPP Depron 3D Airplane w/Brushless Motor Combo for F3P F3C Fix-Wing Airplane for Adults (MEVP2212)* [Online]. Available from: https://www.amazon.com/Dancing-Wings-Hobby-Electric-Brushless/dp/B07DJ83C34 [Accessed 10 August 2023].

Andersen, C. (2017). *Why aren't primed mortars used as grenades?* [Online]. Quora. Available from: https://www.quora.com/Why-arent-primed-mortars-used-as-grenades/answer/Craig-Andersen-7 [Accessed 10 August 2023].

Argo. (2023). Available from: https://dataselection.euro-argo.eu/ [Accessed 10 August 2023].

Barthelmie, R. J., Hansen, K., Frandsen, S. T., Rathmann, O., Schepers, J. G., Schlez, W. ... and Chaviaropoulos, P. K. (2009). Modelling and measuring flow and wind turbine wakes in large wind farms offshore. *Wind Energy: An International Journal for Progress and Applications in Wind Power Conversion Technology*, 12(5), pp.431-444.

Batchelor, G. K. (1967). An introduction to fluid dynamics. Cambridge university press.

Betz, A. (1920). Das Maximum der theoretisch möglichen Ausnützung des Windes durch Windmotoren. *Zeitschrift für das gesamte Turbinenwesen*, 26, pp.42-43.

Boersma, S., Doekemeijer, B. M., Gebraad, P. M., Fleming, P. A., Annoni, J., Scholbrock, A. K. ... and van Wingerden, J. W. (2017). A tutorial on control-oriented modeling and control of wind farms. *2017 American control conference (ACC)* (pp. 1-18). New York: IEEE.

Branlard, E. (2008). *Introduction to wind turbines aerodynamics: the actuator disk theory* [Online]. http://emmanuel.branlard.free.fr/work/papers/html/2008ecn/node58 [Accessed 10 August 2023].

Buhl Jr, M. L. (2005). *New empirical relationship between thrust coefficient and induction factor for the turbulent windmill state* (No. NREL/TP-500-36834). National Renewable Energy Lab.(NREL), Golden, CO (United States).

Burton, T., Jenkins, N., Sharpe, D. and Bossanyi, E. (2011). *Wind energy handbook.* Hoboken: John Wiley and Sons.

Buuk. (2003). *Me 163 Komert at Canada Aviation Museum* [Online]. Available from: https://commons.wikimedia.org/wiki/File:Me-163_Komet_(Can).jpg [Accessed 10 August 2023].

Caffaz, A., Caiti, A., Casalino, G. and Turetta, A. (2010). The hybrid glider/AUV Folaga. *IEEE Robotics and Automation Magazine*, 17(1), pp.31-44.

Carneiro, J. F. and De Almeida, F. G. (2016). Model of a thermal driven volumetric pump for energy harvesting in an underwater glider. *Energy,* 112, pp.28-42.

Carneiro, J. F. and De Almeida, F. G. (2018). Model and simulation of the energy retrieved by thermoelectric generators in an underwater glider. *Energy Conversion and Management,* 163, pp.38-49.

CCTV. (2019). *Pufferfish Unmanned Helicopter* [Online]. Available from: https://space.bilibili.com/222103174 [Accessed 10 August 2023].

Celik, I. B., Ghia, U., Roache, P. J. and Freitas, C. J. (2008). Procedure for estimation and reporting of uncertainty due to discretization in CFD applications. *Journal of fluids Engineering-Transactions of the ASME,* 130(7), pp.15-17.

Chao, Y. (2016). Autonomous underwater vehicles and sensors powered by ocean thermal energy. *OCEANS 2016-Shanghai* (pp. 1-4). New York: IEEE.

Chaviaropoulos, P. K. and Hansen, M. O. (2000). Investigating three-dimensional and rotational effects on wind turbine blades by means of a quasi-3D Navier-Stokes solver. *Journal of Fluids Engineering*, 122(2), pp.330-336.

Chowdhury, B. H. and Chellapilla, S. (2006). Double-fed induction generator control for variable speed wind power generation. *Electric power systems research*, 76(9-10), pp.786-800.

Claus, B., Bachmayer, R., and Cooney, L. (2012). Analysis and development of a buoyancy-pitch based depth control algorithm for a hybrid underwater glider. *2012 IEEE/OES Autonomous Underwater Vehicles (AUV)* (pp. 1-6). New York: IEEE.

Corten, G. P., and Schaak, P. (2008). *U.S. Patent No. 7,357,622*. Washington, DC: U.S. Patent and Trademark Office.

Crimmins, D. M., Patty, C. T., Beliard, M. A., Baker, J., Jalbert, J. C., Komerska, R. J. ... and Blidberg, D. R. (2006). Long-endurance test results of the solar-powered AUV system. *OCEANS 2006* (pp. 1-5). New York: IEEE.

Cyprusubsea. (2022). *BIOGLIDER* [Online]. Available from: https://cyprus-subsea.com/projects/bioglider/[Accessed 10 August 2023].

Davis, R. E., Eriksen, C. C. and Jones, C. P. (2002). Autonomous buoyancy-driven underwater gliders. *The technology and applications of autonomous underwater vehicles*, pp.37-58.

De Lellis, M., Reginatto, R., Saraiva, R. and Trofino, A. (2018). The Betz limit applied to airborne wind energy. *Renewable Energy,* 127, pp.32-40.

Deters, R. W., Ananda Krishnan, G. K., and Selig, M. S. (2014). Reynolds number effects on the performance of small-scale propellers. *32nd AIAA applied aerodynamics conference* (p. 2151). Atlanta: American Institute of Aeronautics and Astronautics, Inc.

Dixon, S. L. and Hall, C. (2013). *Fluid mechanics and thermodynamics of turbomachinery.* Oxford: Butterworth-Heinemann.

Drzewiecki, S. (1920). *Théorie générale de l'hélice: hélices aériennes et hélices marines.* Paris: Gauthier-Villars et cie..

Encarnacion, J. I., Johnstone, C. and Ordonez-Sanchez, S. (2019). Design of a horizontal axis tidal turbine for less energetic current velocity profiles. *Journal of Marine Science and Engineering,* 7(7), p.197.

Eriksen, C. C., Osse, T. J., Light, R. D., Wen, T., Lehman, T. W., Sabin, P. L. ... and Chiodi, A. M. (2001). Seaglider: A long-range autonomous underwater vehicle for oceanographic research. *IEEE Journal of oceanic Engineering*, 26(4), pp.424-436.

Froude, W. (1978). On the Elementary Relation between Pitch, Slip and Propulsive Efficiency. *Transaction of the Institute of Naval Architects,* 19, pp.22-33.

GE. (2021). *GE designs massive floating turbine to take wind energy into deep water* [Online]. Available from: https://newatlas.com/energy/ge-massive-turbines-floating-ocean/ [Accessed 12 August 2023].

Glauert, H. (1935). *Airplane propellers.* New York: Aerodynamic theory.

Gudmundsson, S. (2013). *General aviation aircraft design: Applied Methods and Procedures*. Oxford: Butterworth-Heinemann.

Gunston, B. (2000). *The Osprey encyclopedia of Russian aircraft.* Oxford: Osprey Publishing.

Gupta, A., Singh, S. N. and Khatod, D. K. (2013). Modeling and simulation of doubly fed induction generator coupled with wind turbine-an overview. *Journal of Engineering, Computers and Applied Sciences (JECandAS),* 2**,** pp.45-54.

Globalspec. (2019). *Check valves — a tutorial* [Online]. Available from: https://insights.globalspec.com/article/10858/check-valves-a-tutorial [Accessed 12 August 2023].

GEO-matching. (2022). *Teledyne Marine Slocum Glider. Geo-matching* [Online]. Available from: https://geo-matching.com/products/slocum-glider [Accessed 12 August 2023].

Haldeman, C. D., Schofield, O., Webb, D. C., Valdez, T. I. and Jones, J. A. (2015). Implementation of energy harvesting system for powering thermal gliders for long duration ocean research. *OCEANS 2015-MTS/IEEE Washington* (pp. 1-5). New York: IEEE.

Harrison, M. E., Batten, W. M. J., Myers, L. E. and Bahaj, A. S. (2010). Comparison between CFD simulations and experiments for predicting the far wake of horizontal axis tidal turbines. *IET Renewable Power Generation*, 4(6), pp.613-627.

Hansen, A. C. and Butterfield, C. P. (1993). Aerodynamics of horizontal-axis wind turbines. *Annual Review of Fluid Mechanics,* 25(1), pp.115-149.

Houck, D. and Cowen, E. A. (2022). Power and Flow Analysis of Axial Induction Control in an Array of Model-Scale Wind Turbines. *Energies,* 15(15), p.5347.

IMOS. (2017). *Underwater glider sets world distance record* [Online]. Available from: https://imos.org.au/news/newsitem/underwater-glider-sets-world-distance-record [Accessed 12 August 2023].

ITTC Specialist Committee. (2011). Recommended procedures and guidelines-Practical Guidelines for Ship CFD Applications. *26th International Towing Tank Conference*, Rio de Janeiro, Brasil.

Javaid, M. Y., Ovinis, M., Nagarajan, T. and Hashim, F. B. (2014). Underwater gliders: a review. *MATEC Web of Conference*s (Vol. 13, p. 02020). London: EDP Sciences.

J Chapman, S. (2004). *Electric machinery fundamentals*. New York: McGraw-hill.

Jalalvand, A. R., Roushani, M., Goicoechea, H. C., Rutledge, D. N. and Gu, H. W. (2019). MATLAB in electrochemistry: A review. *Talanta,* 194, pp.205-225.

Jian, W. (2016). Research on several similarity criteria of ram air turbine operating under high-low altitude. *2016 IEEE International Conference on Aircraft Utility Systems (AUS)* (pp. 141-145). New York: IEEE.

Jones, C., Allsup, B. and DeCollibus, C. (2014). Slocum glider: Expanding our understanding of the oceans. *2014 Oceans-St. John's* (pp. 1-10). New York: IEEE.

Jones, J. A. and Chao, Y. (2008). *U.S. Patent No. 7,353,768*. Washington, DC: U.S. Patent and Trademark Office.

Jones, C. P. (2012). Slocum glider persistent oceanography. *2012 IEEE/OES autonomous underwater vehicles (AUV)* (pp. 1-6). New York: IEEE.

Jones, J. and Chao, Y. (2009). *Alternative OTEC Scheme for a Submarine Robot* (No. NPO-43500).

JPL. (2009. *SOLO-TREC， Sounding Oceanographic Lagrangrian Observer (SOLO) Thermal RECharging (TREC)* [Online]. Available from: https://web.archive.org/web/20100409092506/http://solo-trec.jpl.nasa.gov/SOLO-TREC/ [Accessed 12 August 2023].

Jung, H., Subban, C. V., McTigue, J. D., Martinez, J. J., Copping, A. E., Osorio, J. ... and Deng, Z. D. (2022). Extracting energy from ocean thermal and salinity gradients to power unmanned underwater vehicles: State of the art, current limitations, and future outlook. *Renewable and Sustainable Energy Reviews,* 160, p.112283.

Klintberg, L., Karlsson, M., Stenmark, L., Schweitz, J. Å., and Thornell, G. (2002). A large stroke, high force paraffin phase transition actuator. *Sensors and Actuators A: Physical*, 96(2-3), pp.189-195.

Kong, Q., Ma, J. and Xia, D. (2010). Numerical and experimental study of the phase change process for underwater glider propelled by ocean thermal energy. *Renewable Energy,* 35(4), pp.771-779.

Karmakar, S. D. and Chattopadhyay, H. (2022). A review of augmentation methods to enhance the performance of vertical axis wind turbine. *Sustainable Energy Technologies and Assessments*, 53, p.102469.

Lee, H., Sharp, J., Stokes, D., Pearson, M. and Priya, S. (2018). Modeling and analysis of the effect of thermal losses on thermoelectric generator performance using effective properties. *Applied Energy, 211*, pp.987-996.

Letcher, T. (2023). *Wind energy engineering: a handbook for onshore and offshore wind turbines*. Amsterdam: Elsevier.

Li, H., Wu, X., Zhang, Z., Tan, X., Pan, Y., Dai, C. ... and Xu, Y. (2022). An extended-range wave-powered autonomous underwater vehicle applied to underwater wireless sensor networks. *Iscience*, 25(8), p.104738.

Li, L. (2013). *Experimental testing of low reynolds number airfoils for unmanned aerial vehicles* [Doctoral dissertation, University of Toronto].

Lissaman, P. B. S. (1983). Low-Reynolds-number airfoils. *Annual review of fluid mechanics*, 15(1), pp.223-239.

Liu, L., Chen, M., Yu, J., Zhang, Z. and Wang, X. (2021). Full-scale simulation of self-propulsion for a free-running submarine. *Physics of Fluids*, 33(4), pp.1-16.

Liu, P., Bose, N., Chen, K. and Xu, Y. (2018). Development and optimization of dual-mode propellers for renewable energy. *Renewable energy*, 119, pp.566-576.

Liu, S. and Janajreh, I. (2012). Development and application of an improved blade element momentum method model on horizontal axis wind turbines. *International Journal of Energy and Environmental Engineering,* 3*,* pp.1-10.

Ma, Z., Wang, Y., Wang, S. and Yang, Y. (2016). Ocean thermal energy harvesting with phase change material for underwater glider. *Applied energy,* 178, pp.557-566.

Miguel, J., Báez-López, D. and Báez Villegas, D. A. (2019). *MATLAB Handbook with Applications to Mathematics, Science, Engineering, and Finance.* Leiden: CRC Press.

Marxen, O., Lang, M., Rist, U. and Wagner, S. (2003). A combined experimental/numerical study of unsteady phenomena in a laminar separation bubble. *Flow, Turbulence and Combustion,* 71, pp.133-146.

Menter, F. (1993). Zonal two equation kw turbulence models for aerodynamic flows. *23rd fluid dynamics, plasmadynamics, and lasers conference* (p. 2906). Orlando: AIAA.

Muller, S., Deicke, M. and De Doncker, R. W. (2002). Doubly fed induction generator systems for wind turbines. *IEEE Industry applications magazine*, 8(3), pp.26-33.

Munson, B. R., Young, D. F. and Okiishi, T. H. (1995). Fundamentals of fluid mechanics. *Oceanographic Literature Review*, 10(42), p.831.

Niewiadomska, K. (2004). Evolution, technology and application of Slocum gliders. *International Ocean Systems,* 8(1), pp.10-14.

Niu, W. D., Wang, S. X., Wang, Y. H., Song, Y. and Zhu, Y. Q. (2017). Stability analysis of hybrid-driven underwater glider. *China Ocean Engineering,* 31(5), pp.528-538.

NIWA. (2022). *RV Tangaroa* [Online]. Available from: https://niwa.co.nz/services/vessels/niwa-vessels/rv-tangaroa [Accessed 12 August 2023].

Nova. (2021). *The EnFAIT project: Enabling Future Arrays in Tidal* [Online]. Available from: https://novainnovation.com/news [Accessed 12 August 2023].

NASA Tech Brief. (2009). *Alternative OTEC Scheme for a Submarine Robot* [Online]. Available from: https://ntrs.nasa.gov/api/citations/20090008432/downloads/20090008432.pdf [Accessed 12 August 2023].

PLOCAN. (2016). *Graphical 3D representation of the regional bathymetry* [Online]. Available from: https://oom.arditi.pt/glider/ [Accessed 10 August 2023].

Parker. (2023). *Bladder Accumulator - High Pressure (EHV) - (Europe)* [Online]. Available from: https://ph.parker.com/ae/en/product/bladder-accumulator-high-pressure-ehv/10866301125 [Accessed 12 August 2023].

Rankine, W. J. M. (1865). On the mechanical principles of the action of propellers. *Transactions of the Institution of Naval Architects*, 6, pp.13-39.

Richardson, L. F. (1911). IX. The approximate arithmetical solution by finite differences of physical problems involving differential equations, with an application to the stresses in a masonry dam. Philosophical Transactions of the Royal Society of London. *Series A, Containing Papers of a Mathematical or Physical Character,* 210(459-470), pp.307-357.

Roache, P. J. (1998). Verification of codes and calculations. *AIAA journal,* 36(5), pp.696-702.

Roberts, L. S., Finnis, M. V. and Knowles, K. (2017). Forcing boundary-layer transition on a single-element wing in ground effect. *Journal of Fluids Engineering*, 139(10), p.101205.

RS. (2022). *SMC Solenoid Valve VX3114-01F-3DR1, 3 port(s)* [Online].Available from: https://uk.rs-online.com/web/p/solenoid-valves/0168187?cm_mmc=UK-PLA-DS3A-_-google-_-CSS_UK_EN_Plumbing_%26_Pipeline_Whoop-_-Solenoid+Valves_Whoop-_-168187&matchtype=&pla-495211978472&cq_src=google_ads&cq_cmp=9771206590&cq_term=&cq_plac=&cq_net=g&cq_plt=gp&gclid=Cj0KCQiA14WdBhD8ARIsANao07imiGxJiS1NrhdGWuFeLxtIrqOHkwm2ARo9yeyVSPenVbR88bQLZ2caAvrlEALw_wcB&gclsrc=aw.ds [Accessed 12 August 2023].

Saad, M. M. M., Mohd, S., Zulkafli, M. F., Samiran, N. A. and Didane, D. H. (2021). CFD Simulation Study on the Performance of a Modified Ram Air Turbine (RAT) for Power Generation in Aircrafts. *Fluids*, 6(11), p.391.

Saad, M. M., Mohd, S. B., and Zulkafli, M. F. (2017). A survey on the use of ram air turbine in aircraft. *AIP Conference Proceedings* (Vol. 1831, No. 1). New York: AIP Publishing.

Schlichting, H. and Kestin, J. (1961). *Boundary layer theory* (Vol. 121). New York: McGraw-Hill.

Schmidt, M. (2007). *Phase Change Materials-latent heat storage for interior climate control.* Ludwigshafen: BASF, Ludwigshafen, Germany.

Schofield, O., Kohut, J., Aragon, D., Creed, L., Graver, J., Haldeman, C. ... and Glenn, S. (2007). Slocum gliders: Robust and ready. *Journal of Field Robotics,* 24(6), pp.473-485.

Seatrec. (2022). *Deep Technology* [Online]. Available from: https://seatrec.com/technology/ [Accessed 12 August 2023].

Sen, P. C. (2021). *Principles of electric machines and power electronics*. Hoboken: John Wiley and Sons.

Sezen, S., Delen, C., Dogrul, A. and Atlar, M. (2021). An investigation of scale effects on the self-propulsion characteristics of a submarine. *Applied Ocean Research*, 113, p.102728.

Shen, W. Z., Mikkelsen, R., Sørensen, J. N. and Bak, C. (2005). Tip loss corrections for wind turbine computations. *Wind Energy: An International Journal for Progress and Applications in Wind Power Conversion Technology*, 8(4), pp.457-475.

Sherman, J., Davis, R. E., Owens, W. B. and Valdes, J. (2001). The autonomous underwater glider" Spray". *IEEE Journal of Oceanic Engineering*, 26(4), pp.437-446.

Shi, W. (2017). *Biomimetic improvement of hydrodynamic performance of horizontal axis tidal turbines* [Doctoral dissertation, Newcastle University].

Shi, W., Atlar, M., Norman, R., Day, S. and Aktas, B. (2019). Effect of waves on the leading-edge undulated tidal turbines. *Renewable energy,* 131, pp.435-447.

Shi, W., Hou, H., Xu, Y. and Mehmet, A. (2022). *A new thermal buoyancy engine and its control method* [Online]. Available from: https://patents.google.com/patent/GB2597095A/en?q=(A+new+thermal+buoyancy+engine+and+its+control+method)&oq=A+new+thermal+buoyancy+engine+and+its+control+method [Accessed 12 August 2023].

Stark, C., Shi, W. and Troll, M. (2021). Cavitation funnel effect: Bio-inspired leading-edge tubercle application on ducted marine propeller blades. *Applied Ocean Research,* 116, p.102864.

Sriti, M. (2017). Tip loss factor effects on aerodynamic performances of horizontal axis wind turbine. *Energy Procedia,* 118, pp.136-140.

Takahashi, K. and Sahoo, P. K. (2019, November). Numerical study on self-propulsive performance of the DARPA Suboff submarine including uncertainty analysis. *International Conference on Ships and Offshore Structures* (pp.4-8), Florida, USA.

Torkaman, H. and Keyhani, A. (2018). A review of design consideration for Doubly Fed Induction Generator based wind energy system. *Electric Power Systems Research,* 160, pp.128-141.

Van der Hoek, D., Kanev, S., Allin, J., Bieniek, D. and Mittelmeier, N. (2019). Effects of axial induction control on wind farm energy production-a field test. *Renewable Energy,* 140, pp.994-1003.

Vélez, C., de Zárate, J. M. O. and Khayet, M. (2015). Thermal properties of n-pentadecane, n-heptadecane and n-nonadecane in the solid/liquid phase change region. *International Journal of Thermal Sciences,* 94, pp.139-146.

Wang, G., Yang, Y. and Wang, S. (2020). Ocean thermal energy application technologies for unmanned underwater vehicles: A comprehensive review. *Applied Energy,* 278, p.115752.

Wang, G., Yang, Y., Wang, S., Zhang, H. and Wang, Y. (2019). Efficiency analysis and experimental validation of the ocean thermal energy conversion with phase change material for underwater vehicle. *Applied Energy,* 248, pp.475-488.

Webb, D. C., Simonetti, P. J. and Jones, C. P. (2001). SLOCUM: An underwater glider propelled by environmental energy. *IEEE Journal of oceanic engineering*, 26(4), pp.447-452.

WHOI. (2022). *Spray Glider* [Online]. Available from: https://www.whoi.edu/what-we-do/explore/underwater-vehicles/auvs/spray-glider/ [Accessed 12 August 2023].

Wikipedia. (2014). *File:THERMOCLINE.png* [Online]. Available from: https://en.m.wikipedia.org/wiki/File:THERMOCLINE.png [Accessed 12 August 2023].

Xue, D. Y., Wu, Z. L., Wang, Y. H. and Wang, S. X. (2018). Coordinate control, motion optimization and sea experiment of a fleet of Petrel-II gliders. *Chinese Journal of Mechanical Engineering*, 31, pp.1-15.

Yamamoto, I. (2015). Research on next autonomous underwater vehicle for longer distance cruising. *IFAC-PapersOnLine*, 48(2), pp.173-176.

Yang, M., Wang, Y., Zhang, X., Liang, Y. and Wang, C. (2022). Parameterized dynamic modeling and spiral motion pattern analysis for underwater gliders. *IEEE Journal of Oceanic Engineering,* 48(1), pp.112-126.

Yang, Y., Wang, Y., Ma, Z. and Wang, S. (2016). A thermal engine for underwater glider driven by ocean thermal energy. *Applied Thermal Engineering*, 99, pp.455-464.

Zhang, H. W., Wang, Y. H. and Lian, Z. G. (2009). Application and improvement of the interlayer thermal engine powered by ocean thermal energy in an underwater glider. *2009 Asia-Pacific Power and Energy Engineering Conference* (pp. 1-4). New York: IEEE.

Zhang, H., Ma, X., and Yang, Y. (2022). An external ocean thermal energy power generation modular device for powering smart float. *Energies,* 15(10), p.3747.

Zhang, H. W., Wang, Y. H. and Lian, Z. G. (2009). Application and improvement of the interlayer thermal engine powered by ocean thermal energy in an underwater glider. *2009 Asia-Pacific Power and Energy Engineering Conference* (pp. 1-4). New York: IEEE.

Zhao, D., Han, N., Goh, E., Cater, J. and Reinecke, A. (2019). *Wind turbines and aerodynamics energy harvesters.* New York: Academic Press.

9GAG. (2019). *Ram air turbine (RAT) emergency power supply in case power loss* [Online]. Available from: https://9gag.com/gag/an5Q6AB [Accessed 12 August 2023].

Appendix A Numerical setup and grid convergence analysis for CFD simulation in section 4.2.1.2

As mentioned in section 4.2.1.2, to balance the thesis structure, detailed information of CFD simulation setup in section 4.2.1.2 has been placed in Appendix A.

Computational method

For these simulations, the implicit unsteady incompressible Reynolds Averaged Navier Stokes (URANS) was implemented with the SST K-ω turbulence model. K-ω SST model merges the benefits of K-ω and K-ε turbulence formulations. Specifically, it adopts K-ω model in boundary layer regions and shifts to K-ε model in external flow areas. As a result, K-ω SST model is proficient in predicting adverse pressure gradient situations and flow separation events (Menter, 1993). Additionally, this model has seen extensive use in research related to submarine propulsion (Sezen et al., 2021, Liu et al., 2021). The time-step ensures that the hull moves 0.005 L_h per time-step, adhering to the recommendations of ITTC, which suggests a time-step between 0.005 L_h and 0.01 L_h (ITTC, 2011).

Computational domain and mesh generation

As depicted in Figure A-1, the study chose a rectangular computational domain to study the flow surrounding UG hull. The inlet boundary is established 4 L_h ahead of the hull as a velocity inlet, and the outlet boundary is set 10 L_h behind the hull as a pressure outlet. Adjacent boundaries are marked as symmetry planes, located 3 L_h from the hull. The hull is treated as no-slip walls. The chosen domain dimensions align with the recommendations from ITTC (ITTC, 2011).

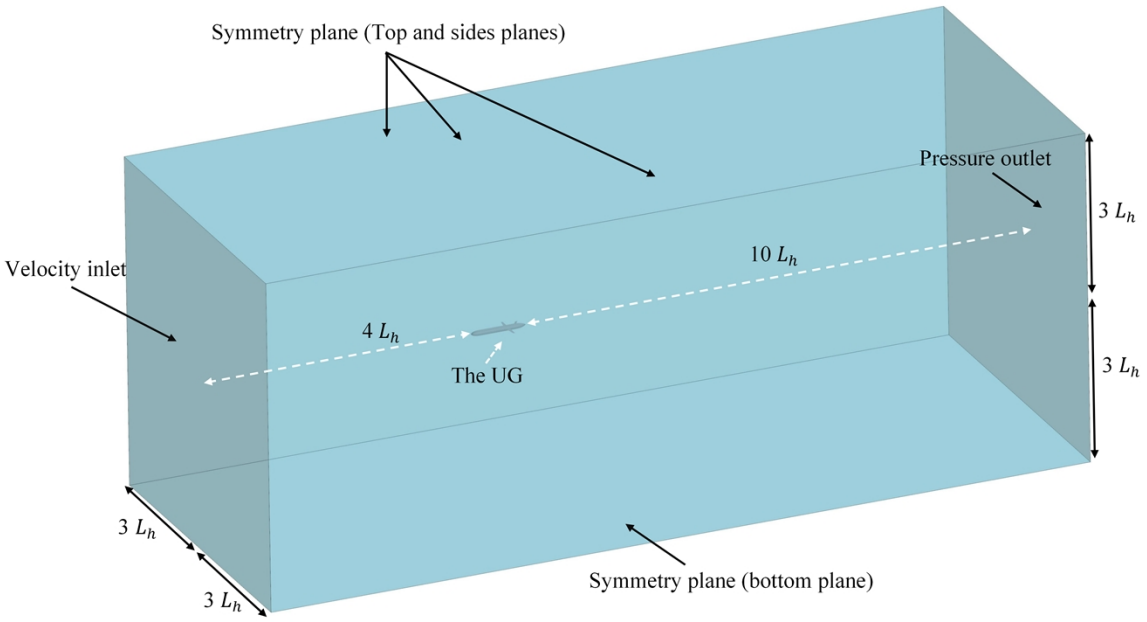

Figure A-1. Domain and boundary condition of the simulation

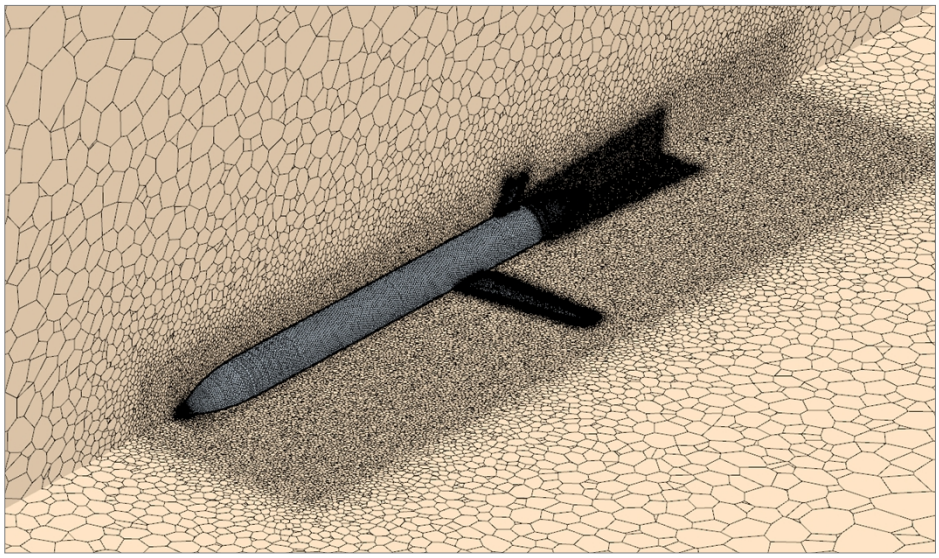

Figure A-2. Cell structure around the hull

The region-based automatic meshing tool, integrated with volumetric controls, was utilized to create a mesh encompassing roughly 3.98 million cells. For the simulation domain, the polyhedral mesh was chosen, having demonstrated its precision in reflecting experimental outcomes in self-propulsion CFD simulations of submarines (Takahashi et al., 2019). The boundary layer was addressed with prism layers. All y+ wall treatment was applied, ensuring the average y+

consistently stayed beneath 1. The space after the hull is refined to capture the wake distribution. The cell structure around UG hull is displayed in Figure A-2. Moreover, the surface meshes of the hull are shown in Figure A-3.

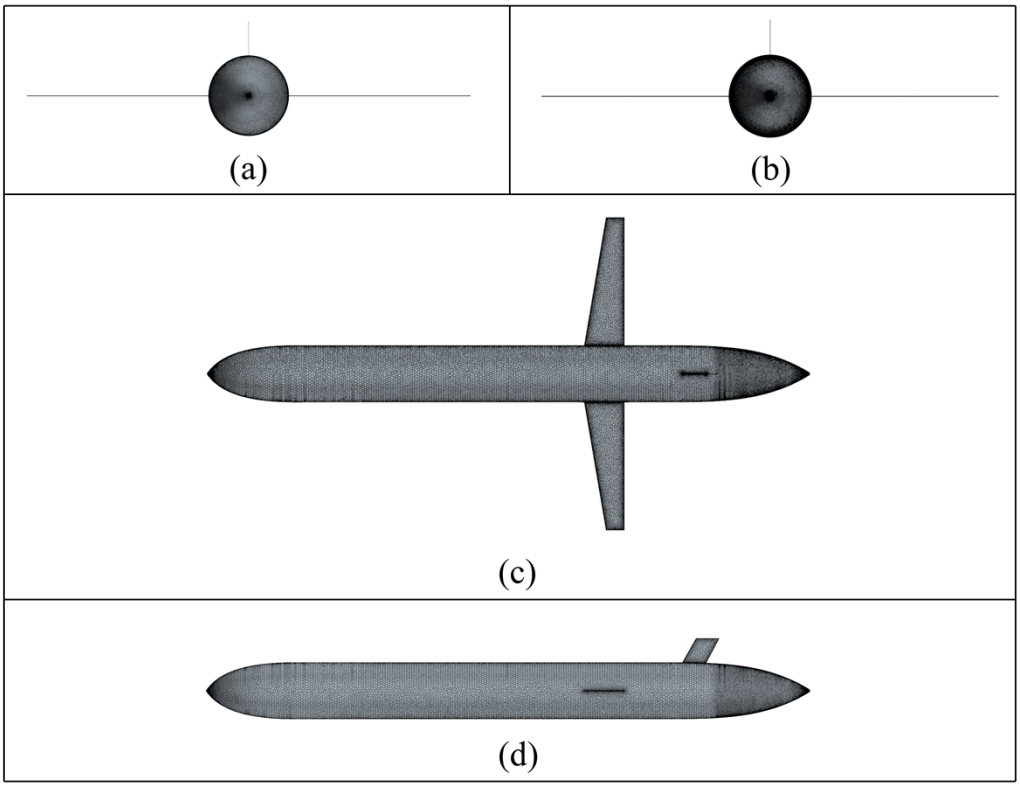

Figure A-3. Surface mesh of the hull: (a) Fore profile; (b) Rear profile; (c) Top profile; and (d) Side profile

Grid convergence analysis

A verification analysis was conducted to assess the uncertainty of CFD simulations using Grid Convergence Index (GCI) technique, originally proposed by Roache (Roache, 1998) and based on Richardson (Richardson, 1911). The comprehensive methodology implemented in this study was developed by Celik (Celik et al., 2008). ITTC also endorses this method to compute the numerical error of a solution. In this study, hull resistance (R_h) and wake factor (W_f) were chosen as the integral variables at V =1 m/s. There are two positions for the W_f . They are located 10 cm behind UG, with distances from the hull's own axis being 0 m and 0.015 m, named $W_{f\,0.1}^{0.015}$ and $W_{f\,0.1}^{0.03}$

respectively. The study uses three different mesh cell counts: coarse, medium, and fine, with the meshes comprising 0.98, 2.01, and 3.98 million cells, respectively.

Table A-1: Grid convergence analysis results

	φ_1	φ_2	φ_3	$N_1^{'}$	$N_2^{'}$	$N_3^{'}$	$R^{'}$	$\%GCI_{FINE}^{21}$
R_h (N)	2.763	2.769	2.834	3.98 M	2.01 M	0.98 M	0.087	0.027%
$W_{f0.1}^{0.015}$	0.493	0.472	0.552	3.98 M	2.01 M	0.98 M	-0.263	Oscillatory convergence
$W_{f0.1}^{0.03}$	0.642	0.629	0.701	3.98 M	2.01 M	0.98 M	-0.175	Oscillatory convergence

The tabulated uncertainty results for R_h, $W_{f0.1}^{0.015}$ and $W_{f0.1}^{0.03}$ are shown in Table A-1. φ_1, φ_2, and φ_3 represent the result of fine, medium, and coarse mesh grids, respectively. $N_1^{'}$, $N_2^{'}$ and $N_3^{'}$ represent the grid number of fine, medium, and coarse mesh grids, respectively. The difference between the solution scalars (ε), including ε_{21} and ε_{32} can be calculated through Equation 6-6 and Equation 6-7. With ε_{21} and ε_{32}, ratio of solution scalars, which is used to determine the convergent condition, can be obtained via Equation 6-8. By using the ratio of solution scalars, the solution type can be determined. There are four solution types: $0 < R^{'} < 1$ represents the monotonic convergence; $-1 < R^{'} < 0$ represents the oscillatory convergence; $R^{'} < -1$ represents the oscillatory divergence; and $R^{'} > 1$ represents the monotonic divergence. Subsequently, GCI index can be determined through Equation 6-9.

As depicted in Table A-1, the convergence conditions ($R^{'}$) for R_h is 0.027%, indicating that the simulation exhibits monotonic convergence. Additionally, the convergence conditions ($R^{'}$) for $W_{f0.1}^{0.015}$ and $W_{f0.1}^{0.03}$ are -0.263 and -0.175, respectively, indicating that the simulation exhibits oscillatory convergence. Consequently, based on the uncertainty assessment, the fine mesh consisting of approximately 3.98 million cells was chosen.

Appendix B Numerical setup and grid convergence analysis for CFD simulation in section 5.4.1.1

As mentioned in section 5.4.1.1, to balance the thesis structure, the detailed information of CFD simulation setup in section 5.4.1.1 has been placed in Appendix B.

Computational method

In these simulations, URANS was utilized alongside SST K-ω turbulence model. The K-ω SST model combines the advantages of both K-ω and K-ε turbulence approaches. It employs the K-ω model within boundary layer zones and transitions to K-ε model for outer flow regions. This makes the K-ω SST model especially adept at forecasting adverse pressure gradient conditions and occurrences of flow separation (Menter, 1993). Furthermore, numerous studies related to submarine propulsion have extensively employed this model (Sezen et al., 2021, Liu et al., 2021). According to ITTC guidelines, the selected time-step results in a hull movement of 0.005 L_h per time-step, staying within the advised range of 0.005 L_h to 0.01 L_h (ITTC, 2011).

Computational domain and mesh generation

Figure A-4 illustrates the selection of a rectangular computational domain for analyzing the flow around UG hull. A velocity inlet forms the inlet boundary, positioned 4 L_h ahead of the hull, while the outlet boundary is placed 10 L_h behind the hull and is designated as a pressure outlet. Symmetry planes demarcate the adjacent boundaries, situated 3 L_h from the hull. No-slip walls are used to model the hull. The dimensions of the chosen domain are consistent with the guidelines provided by ITTC (ITTC, 2011).

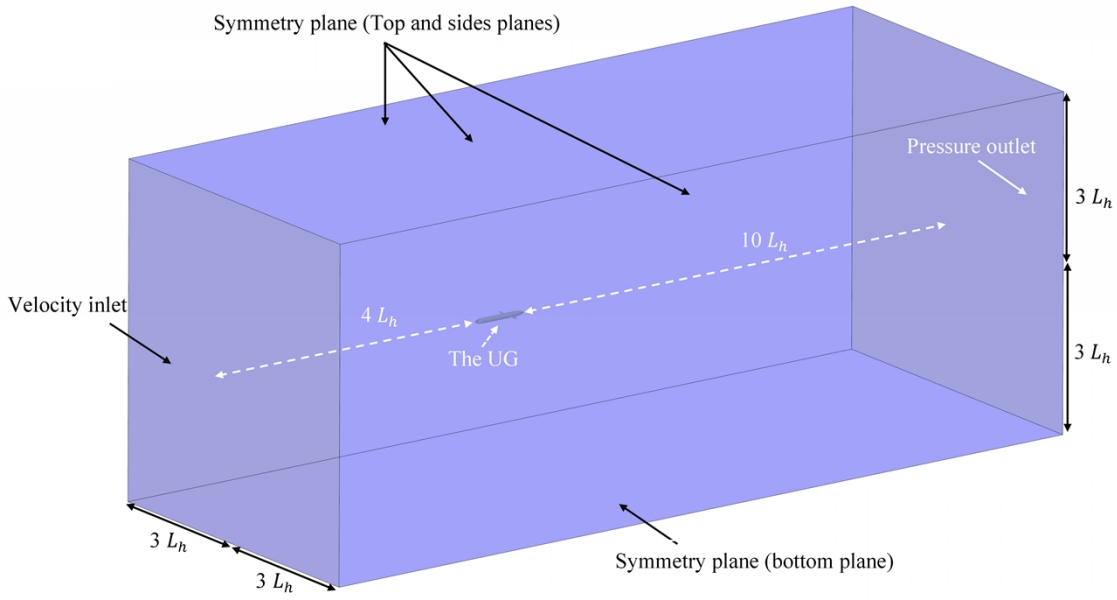

Figure A-4. Domain and boundary condition of the simulation

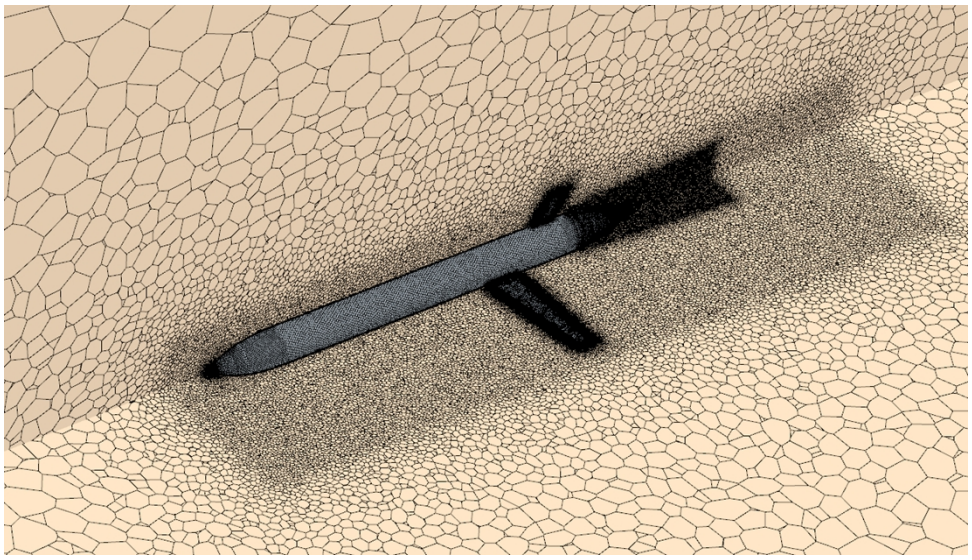

Figure A-5. Cell structure around the hull

The region-based automatic meshing tool, integrated with volumetric controls, was utilized to create a mesh encompassing roughly 3.4 million cells. For the simulation domain, the polyhedral mesh was chosen, having demonstrated its precision in reflecting experimental outcomes in self-propulsion CFD simulations of submarines (Takahashi et al., 2019). The boundary layer was addressed with prism layers. All y+ wall treatment was applied, ensuring the average y+

consistently stayed beneath 1. The space after the hull is refined to capture the wake distribution. The cell structure around UG hull is displayed in Figure A-5. And the surface meshes of the hull is shown in Figure A-6.

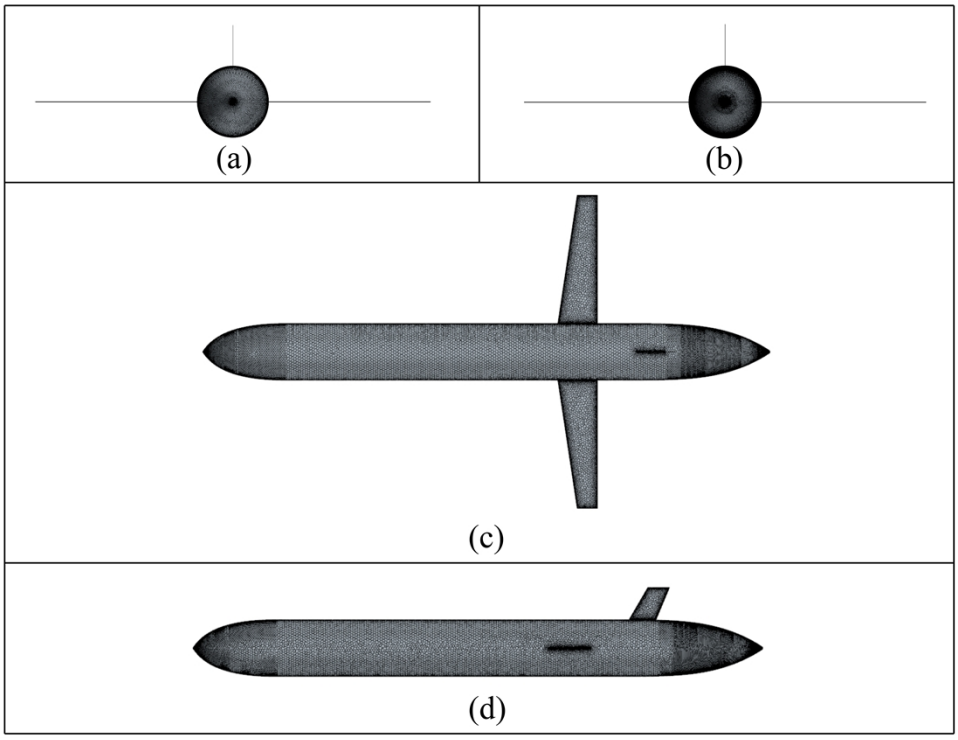

Figure A-6. Surface mesh of the hull: (a) Fore profile; (b) Rear profile; (c) Top profile; and (d) Side profile

Grid convergence analysis

A verification analysis was conducted to assess the uncertainty of CFD simulations using the Grid Convergence Index (GCI) technique, originally proposed by Roache (Roache, 1998) and based on Richardson (Richardson, 1911). The comprehensive methodology implemented in this study was developed by Celik (Celik et al., 2008). ITTC also endorses this method to compute the numerical error of a solution. In this study, C_d s are chosen as the integral variables at V =0.8 m/s and V =1

m/s, named $C_d^{0.8}$ and C_d^1, respectively. The study uses three different mesh cell counts: fine, medium, and coarse, with the meshes comprising 3.38, 1.61, and 0.73 million cells, respectively.

Table A-2: Grid convergence analysis results

	φ_1	φ_2	φ_3	$N_1^{'}$	$N_2^{'}$	$N_3^{'}$	$R^{'}$	$\%GCI_{FINE}^{21}$
$C_d^{0.8}$	0.1944	0.1967	0.2020	3.38 M	1.61M	0.73 M	0.44	1.4%
C_d^1	0.1876	0.1896	0.1946	3.38 M	1.61M	0.73 M	0.41	1.1%

The tabulated uncertainty results for $C_d^{0.8}$ and C_d^1 are shown in Table A-2. φ_1, φ_2, and φ_3 represent the result of fine, medium, and coarse mesh grids, respectively. $N_1^{'}$, $N_2^{'}$ and $N_3^{'}$ represent the grid number of fine, medium, and coarse mesh grids, respectively. The difference between the solution scalars (ε), including ε_{21} and ε_{32} can be calculated through Equations 6-6 and 6-7. With ε_{21} and ε_{32}, ratio of solution scalars, which is used to determine the convergent condition, can be obtained via Equation 6-8. By using the ratio of solution scalars, the solution type can be determined. There are four solution types: $0 < R^{'} < 1$ represents the monotonic convergence; $-1 < R^{'} < 0$ represents the oscillatory convergence; $R^{'} < -1$ represents the oscillatory divergence; and $R^{'} > 1$ represents the monotonic divergence. Subsequently, GCI index can be determined through Equation 6-9.

As depicted in Table A-2, the convergence conditions ($R^{'}$) for $C_d^{0.8}$ and C_d^1 are 0.44 and 0.41 respectively, indicating that the simulation exhibits monotonic convergence. The uncertainty errors for $C_d^{0.8}$ and C_d^1 are 1.4% and 1.1%, respectively. Consequently, based on the uncertainty assessment, the fine mesh of approximately 3.38 million cells was chosen.